Surface plasmon polaritons and light at interfaces: propagating and evanescent waves

Samenstelling van de promotiecommissie:

prof. dr. L. Kuipers (promotor)	Universiteit Twente
prof. dr. R. Quidant	Institut de Ciències Fotòniques, España
prof. dr. J. L. Herek	Universiteit Twente
prof. dr. S. G. Lemay	Universiteit Twente
prof. dr. G. Rijnders	Universiteit Twente
prof. dr. T. D. Visser	Vrije Universiteit Amsterdam

This research was supported by the European Commission under the
Marie Curie Scheme (Contract No. MEST-CT-2005-021000)
and is part of the research program of the
“Stichting Fundamenteel Onderzoek der Materie” (FOM), which is
financially supported by the
“Nederlandse Organisatie voor Wetenschappelijk Onderzoek” (NWO).

This work was carried out at:
NanoOptics Group,
FOM-Institute for Atomic and Molecular Physics (AMOLF)
Science Park 102, 1098 XG Amsterdam, The Netherlands,
where a limited number of copies of this thesis is available.

ISBN: 9789077209493
Printed by Ipskamp Drukkers, Amsterdam, The Netherlands.

SURFACE PLASMON POLARITONS AND LIGHT AT INTERFACES: PROPAGATING AND EVANESCENT WAVES

PROEFSCHRIFT

ter verkrijging van
de graad van doctor aan de Universiteit Twente,
op gezag van de rector magnificus,
prof. dr. H. Brinksma,
volgens besluit van het College voor Promoties
in het openbaar te verdedigen
op donderdag 30 juni 2011 om 14:45 uur

door

Marko Spasenović

geboren op 7 februari 1983
te Belgrado, Servië

Dit proefschrift is goedgekeurd door:
prof. dr. L. (Kobus) Kuipers

Za moje roditelje i moju sestru. Za Snežanu.

Contents

1 General introduction 5

1.1 The diffraction limit and surface plasmon polaritons 6
    1.1.1 Surface plasmon polaritons on a flat interface 7
    1.1.2 Field directions for surface plasmon polaritons . . . 7
    1.1.3 Coupling to surface plasmon polaritons 8
    1.1.4 Surface plasmon polariton waveguides 9
1.2 Photonic crystal waveguides 11
    1.2.1 Dispersion in photonic crystal waveguides 14
    1.2.2 Coupling to slow light in photonic crystal waveguides 16
    1.2.3 Multiple scattering and localization in photonic crystal waveguides 17
1.3 Phase- and polarization-sensitive near-field microscope . . . 18
1.4 Outline of this thesis 21

2 Modal symmetry in plasmonic slot waveguides 25

2.1 Introduction 26
2.2 Experiments 26
    2.2.1 Experimental details 26
    2.2.2 Measurement results 27
2.3 Discussion 31
2.4 Conclusion 33

3 Bending losses in plasmonic nanowire waveguides 35

3.1 Introduction 36
3.2 Sample fabrication and near-field measurement 37
3.3 Characterization of losses 39
    3.3.1 Transmission through nanowire bends 39
    3.3.2 Propagation losses 39
    3.3.3 Isolating the bending losses 41

3.3.4 Simulation 42
3.4 Discussion 43
3.5 Conclusion 46

4 The Talbot effect for surface plasmon polaritons 47
4.1 Introduction 48
4.2 Experiments 48
4.2.1 Experimental details 48
4.2.2 Measurement results 50
4.3 Discussion 50
4.4 Conclusion 57

5 Evanescent modes at the interface to slow light 59
5.1 Introduction 60
5.2 Sample and far-field measurements 60
5.3 Near-field measurements 63
5.4 Dispersion measurements and modal extraction 65
5.5 Conclusion 68

6 Measuring localization length with a near-field probe 71
6.1 Introduction 72
6.2 Transmission and near-field measurements 74
6.3 Near-field measurements of localized states 77
6.4 Influence of the probe on transmission 77
6.5 Measuring localization length 80
6.6 Discussion and conclusions 85

7 Applications and outlook 87
7.1 Classical and quantum optical circuits 88
7.1.1 Nanowires and slot waveguides for photonic circuits and quantum computing 89
7.1.2 Coupling light to the nanoscale 91
7.1.3 Polarization-controlled excitation of single photon sources 93
7.1.4 Nanoscale polarization demultiplexer 94
7.2 Trapping atoms with nanostructures 96
7.3 Slow light in photonic crystal waveguides 97

List of publications **115**

Summary **117**

Acknowledgements **121**

1

General introduction

Vision is a primary natural means of human perception. Light is crucial for vision. The basic process of vision involves three steps: the emission of light by a source, scattering by an object, and detection by interaction with matter in our eye. Modern technology has improved all three steps. The incandescent light bulb was followed by fluorescent tubes and light-emitting diodes, with an associated improvement in efficiency and directionality of emission. The advent of the laser brought on a revolution in light manipulation technology, with optical communications, optical storage media, and micromachining. Detectors range from miniature solid-state photodetectors to single-photon counters. Objects can be made to scatter, absorb or transmit light of practically any desired frequency. As a consequence of such sophisticated technological development, light is being used in the modern world for much more than human vision.

Today, most telecommunication signals are guided by light in optical fibers. Fibers offer a large bandwidth and have low power dissipation, compared to electrical connections [1]. At the nodes of optical networks sit amplifiers, interconnects, and computers based on electronics. These components would offer increased computational power and speed if they would also benefit from optics. The promise for efficient integration of optics and electronics has driven the field of nano-optics in recent years

[2, 3]. Nano-optics explores the science and applications of light fields confined to length scales of tens to hundreds of nanometers.

Optical emitters placed in confined optical fields can radiate more efficiently than emitters in free space, due to the large photonic mode density associated with confined waves [4, 5]. Thus the efficiency of sources such as light-emitting diodes and lasers can be improved by using confined optical fields. If the confined field is a mode of a nanoscale waveguide, the emission occurs preferentially into the waveguide mode, with an associated increase both in efficiency and directionality of emission. Efficient emission is also important for sources of non-classical light on a chip [6], for the prospect of integrated quantum information. The study of nanometer-scale waveguides with small mode volumes is hence an important step towards using nano-optics for optical computation and communication.

Reducing the speed of light is another important feat of on-chip light manipulation. Slow light leads to compact optical delays and buffers, optical switches, and the prospect of active optical components [7]. Efficient coupling to slow light is thus an important technological challenge.

1.1 The diffraction limit and surface plasmon polaritons

The diffraction limit is the traditional smallest size to which light can be concentrated, using standard optical elements. The limit was first derived by Ernst Abbe in 1873 [8]. According to Abbe, the smallest size Δx to which light can be focused in one dimension is on the order of

$$\Delta x \approx \frac{2\pi}{\Delta k_x} = \frac{\lambda_0}{2}, \tag{1.1}$$

where Δk_x is the maximum possible spread of the wavevector component k_x and λ_0 is the wavelength in free space.

Recently, scientists have learned that light can be confined to a smaller scale than in free space by utilizing surface plasmon polaritons (SPPs) [9]. Surface plasmon polaritons are propagating solutions of Maxwell's equations at an interface between a dielectric and a metal. They are electromagnetic waves coupled to oscillations of free electrons on the surface of the metal. The fact that SPPs are confined to the interface has caused much excitement [3, 10, 11], because of possible applications involving light control on the nanometer scale.

1.1.1 Surface plasmon polaritons on a flat interface

For a metal-dielectric interface normal to the spatial direction $\hat{z}$, the dispersion of an SPP propagating in the $\hat{x}$ direction is [9]

$$k_x = k_0 \sqrt{\frac{\epsilon_d \epsilon_m}{\epsilon_d + \epsilon_m}}. \tag{1.2}$$

Here $k_0 = \omega/c$ is the wavevector in free space, ϵ_m and ϵ_d are the dielectric constants of the metal and dielectric, respectively. When $\epsilon_m < -\epsilon_d$, $k_x > k_0$. The wavevector in free space is

$$\epsilon k_0^2 = k_x^2 + k_z^2, \tag{1.3}$$

where k_z is the wavevector in the direction normal to the surface. As a result, when $k_x > k_0$, the wavevector normal to the interface is imaginary and the electromagnetic field decays exponentially in that direction. A sketch of the z-dependence of the magnitude of the H_y component of the SPP field is depicted in figure 1.1. The field peaks on the surface and decays exponentially in both media. For the case of an interface between Au and air, and a free-space wavelength of 1.5 μm, the decay length is on the order of one micrometer into air and 10 nm into Au. The confinement is thus only slightly smaller than the wavelength in free space. Higher confinement can be achieved by using a dielectric with a higher permittivity.

The dominant factor for propagation losses of SPPs on an Au surface is heat transfer to the electron bath, or Ohmic losses. In the presence of losses, the wavevector k_x is a complex number, which leads to a characteristic propagation length L_{SPP}. The propagation length is the distance in which the SPP intensity decays to $1/e$ of the original value. In the case of an Au/air interface at $1.5\,\mu m$, this number is on the order of $100\,\mu m$. The imaginary component of k_x, k_x'', scales with $\epsilon_d^{3/2}$, so Ohmic damping is bigger for plasmons on an interface of a metal and a high-index dielectric.

1.1.2 Field directions for surface plasmon polaritons

Surface plasmon polaritons are transverse magnetic (TM) waves. This means that there is no magnetic field in the propagation direction. In the

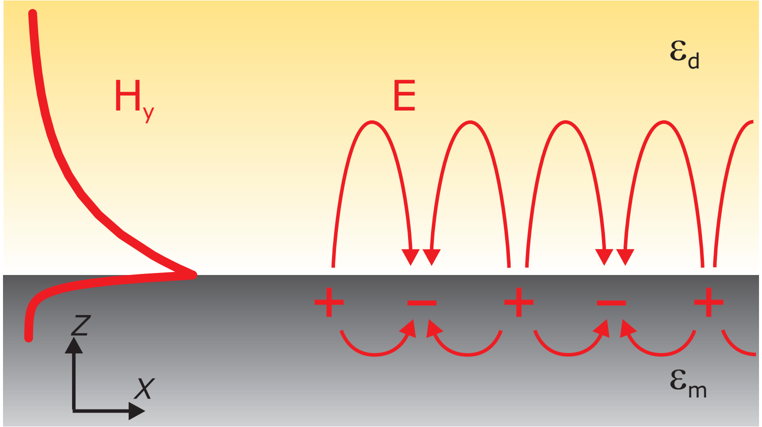

Figure 1.1: A sketch of a surface plasmon polariton at an interface between a metal and a dielectric. The grey area indicates the metal half-space. The orange area indicates the dielectric. The red line on the left is a representation of the amplitude of the magnetic field of the SPP. The magnetic field peaks on the interface and decays exponentially in both half-spaces. Electric field lines of the SPP are shown on the right.

picture of figure 1.1, the wave propagates to the right (in the x direction) and the magnetic field oscillates out of the paper plane (in the y direction). The electric field lines point as shown on the right side of the image. Hence, the electric field points primarily out of plane (in the z direction), but also has a longitudinal component (in the direction of propagation, x).

1.1.3 Coupling to surface plasmon polaritons

The fact that $k_x > k_0$ allows for focusing SPPs to dimensions smaller than the free-space wavelength, however it also introduces the challenge of coupling to SPPs from free space. The most common methods for exciting SPPs are attenuated total reflection (ATR), the use of a subwavelength scatterer, and grating coupling [9].

Attenuated total reflection relies on using a prism made of a dielectric with permittivity larger than ϵ_d. Light is totally internally reflected at one side of the prism. The metal surface is brought to close vicinity of the prism and SPPs can be excited through the tunneling of the evanescent field. Because the light in the prism has a higher wavevector than in air, it can be phase-matched to SPPs. This is called the Otto configuration. Similarly, in the Kretschmann-Raether configuration, plasmons are excited on a metal film deposited onto the prism [12]. With these methods, the coupling to SPPs depends strongly on the incident angle and is highly wavelength-selective.

A subwavelength scatterer may provide additional momentum for light to couple to SPPs. The momentum is provided by the scattering event. A consideration of electric fields for the case of a single hole is instructive. A sketch of the situation is depicted in figure 1.2. A circular hole is made in a gold film (yellow area). A linearly polarized laser beam is incident on the hole. The polarization of the beam is indicated by the arrow labelled E. The edges of the hole are polarized by the electric field of the beam, but boundary conditions impose that the electric field lines point normal to the metal surface. The result is that the electric field at the hole is strongest in the directions parallel to the incident polarization, and progressively weaker around the hole, as indicated by the length of the arrows in figure 1.2a. The edge of the hole reradiates into SPPs. Surface plasmon polaritons have a higher intensity in the directions given by the incident polarization than elsewhere, because the overlap between the incident linearly polarized electric field and the longitudinal component of the SPP is greatest in that direction [13, 14]. The intensity of the radiation is thus proportional to $\cos^2\theta$, where θ is the angle from the direction of polarization of the laser beam. The radiation pattern of a subwavelength hole is depicted in figure 1.2. This method of coupling to SPPs is usually the easiest to achieve and works over a wide range of frequencies, however it is not efficient [14].

A diffraction grating with a well-defined pitch can provide momentum, given by the grating constant, to phase-match light to SPPs. This is the most common method of SPP excitation, as it strikes a balance between bandwidth, efficiency and ease-of-use.

1.1.4 Surface plasmon polariton waveguides

The spatial extent of SPPs in a direction orthogonal to the direction of propagation can be reduced by coupling two SPPs. For example, if two metal surfaces are brought in the vicinity of each other, the two surface modes can couple to form a waveguide mode. This can occur in two configurations, which are sketched in figure 1.3. Figure 1.3a depicts an insulator-metal-insulator (IMI) configuration, in which a thin layer of metal is surrounded

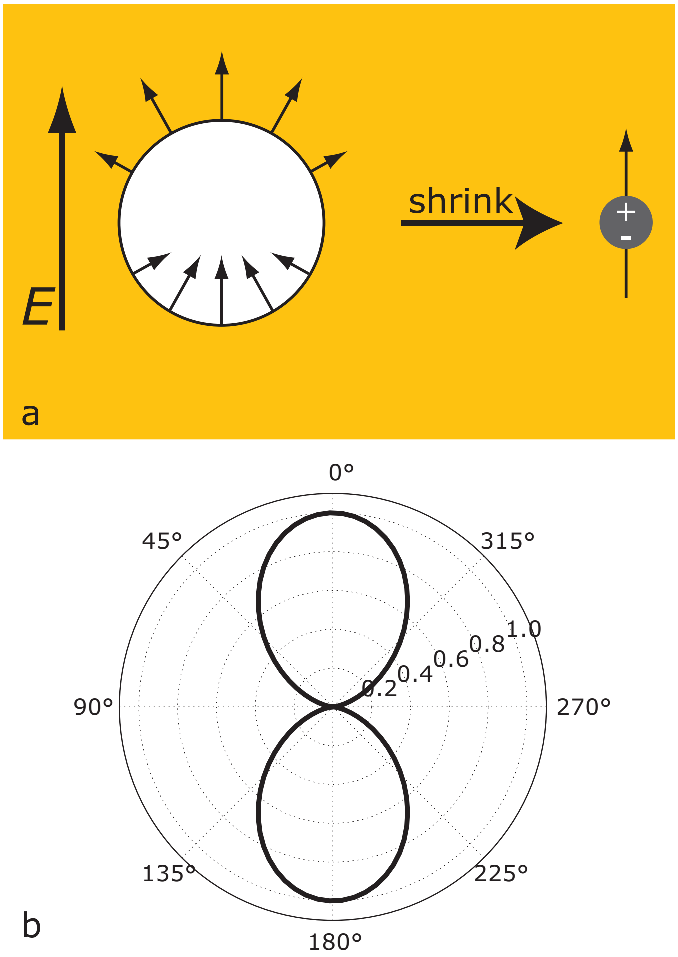

Figure 1.2: Launching SPPs from a single hole in a gold film. (a) The yellow region indicates gold. The white circle represents a hole in the film. A laser beam is incident with linear polarization in the direction of E. The arrows on the edges of the hole represent the induced electric field. The direction of the arrows is given by boundary conditions at the edges. The length of the arrows represents the magnitude, resulting from a projection of E onto the direction of the arrow. A hole which is significantly smaller than the wavelength can be represented by a dipole emitter. (b) The radiation pattern of a subwavelength hole in a gold film.

by two half-spaces of dielectric. The 2D half-spaces are infinite in the direction orthogonal to the paper plane. The two surface plasmon modes couple to form an IMI mode [15, 16, 17], which is confined to the metal slab. In reality, two modes are formed, however only the mode with a symmetric charge distribution is confined to the metal [18]. This mode stays confined for arbitrarily small non-zero metal thickness. If, instead of extending infinitely out of the paper plane, this geometry is placed on a substrate, a 1D waveguide is formed. This waveguide is a metallic nanowire.

The mode with the symmetric charge distribution will from now on be called the “symmetric” mode. Conversely, modes with an antisymmetric charge distribution will be called “antisymmetric”. The electric field lines of the symmetric mode are sketched on the right side of figure 1.3a. On the left side of the figure, we depict a sketch of the absolute magnetic field of the SPP. It is clear that the field is confined to the wire.

Conversely, one can create a metal-insulator-metal (MIM) configuration, depicted in figure 1.3b. In this structure, two metal half-spaces are brought close to each other, with a dielectric in between. Similarly to the previous case, plasmonic modes are formed in the gap between the metal interfaces [16, 19, 20]. The symmetric mode in this case exhibits cutoff when the waveguide is approximately $\pi c/(\sqrt{\epsilon_d}\omega)$ [20]. Below this thickness, only the antisymmetric mode remains. The magnitude of the magnetic field and the electric field lines for this mode are sketched in figure 1.3b. In this geometry, waveguides as narrow as 12 nm were reported [20]. The spatial extent of the plasmon field is similar to the width of the waveguide. A 1D equivalent of an MIM waveguide is called a slot waveguide. Since plasmonic waveguides support modes with such high spatial confinement, they are good candidates for enhancing the efficiency of optical emitters. The spatial distribution and symmetry of a mode will affect the efficiency with which an emitter couples to the mode.

1.2 Photonic crystal waveguides

Another method of controlling light propagation on small scales utilizes photonic crystal structures. Photonic crystals (PhCs) are periodic arrangements of dielectric materials [21]. The arrangements are carefully engineered to control the dispersion of light in the crystal.

PhCs can be fabricated in one, two or three dimensions. To understand

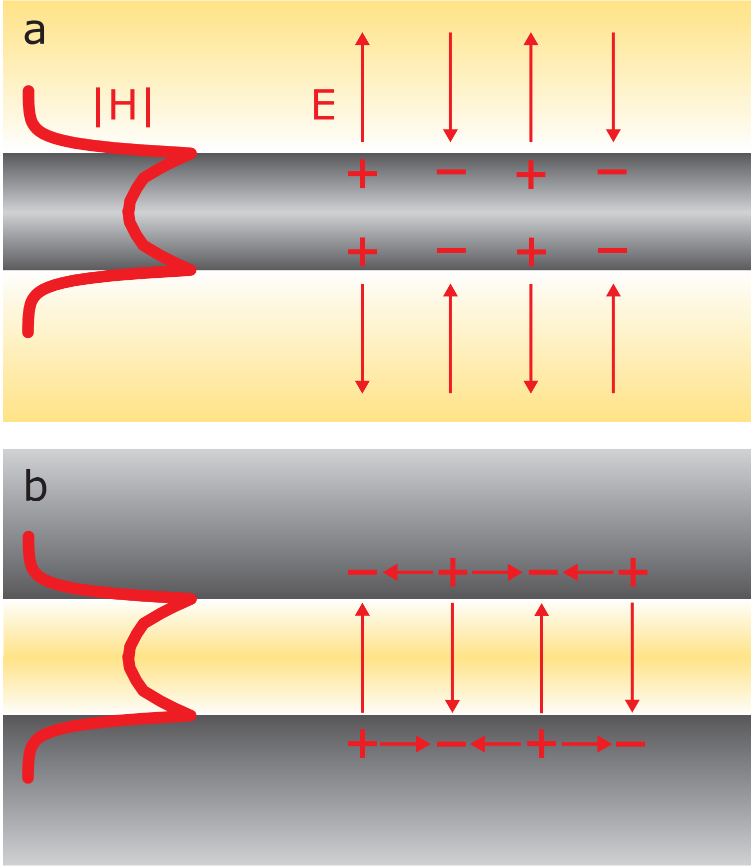

Figure 1.3: A sketch of magnetic field amplitudes and electric field lines for (a)an IMI waveguide and (b)an MIM waveguide. In both cases, the SPP field is confined to the waveguide.

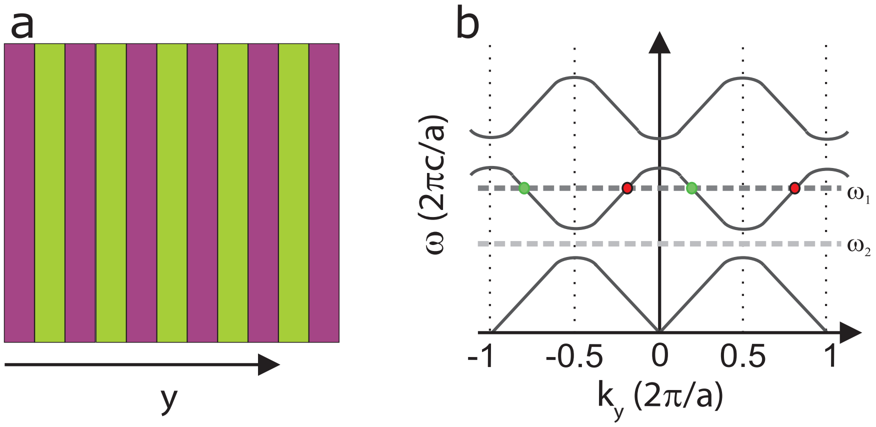

Figure 1.4: Bragg stack geometry and dispersion. a) Geometry of the Bragg stack. Different colors indicate layers with different refractive indices, n_1 *and* n_2*. Light is incident from the left, normal to the interfaces. b) A sketch of the dispersion of the Bragg stack. The horizontal axis is wavevector, the vertical axis is frequency. Light of a given frequency must obey the dispersion curve. The solid black lines are allowed modes. At a frequency* ω_1 *(dark grey dashed line), the wave consists of several Bloch components, indicated by the red dots. At a frequency* ω_2 *(light grey dashed line), there are no modes due to an avoided crossing between two Bloch modes. The region without modes is called the bandgap.*

the basic properties of PhCs, it is instructive to start with the 1D case. In this structure, alternating layers of two dielectrics with a high contrast of refractive index are stacked with period a, as sketched in figure 1.4a. This structure is called a Bragg stack. An optical wave which propagates orthogonal to the layer boundaries is partially reflected at each boundary. For specific wavelengths, the many partial reflections add up constructively to create total reflection. The range of frequencies for which this occurs is called the photonic stop gap [22, 23]. In the photonic stop gap, there are no allowed propagating modes in the structure.

Due to the periodic nature of the structure, light propagating in the crystal obeys Bloch's theorem, similar to electrons in a semiconductor crystal [24]. Bloch's theorem states that the eigenfunctions of the wave equation for a periodic potential are the product of a plane wave e^{iky} and a function

$u(y)$ with the periodicity of the crystal lattice. Here k is the wavevector of the plane wave. Consequently, the amplitude of the plane wave is modulated with the periodicity of the structure. As a result, the solution can be expressed as an expansion in m Bloch harmonics. The m-th harmonic has a wave vector $k + mG$, where $G = 2\pi/a$ is the reciprocal lattice vector.

1.2.1 Dispersion in photonic crystal waveguides

Optical properties of a material are conveniently expressed with a dispersion relation, which relates the optical frequency to the wavevector in the material. The dispersion relation for a Bragg stack is depicted in figure 1.4b. Modes which light is allowed to populate are visible as solid black lines. Light of a certain frequency ω_1, indicated by the dark grey dashed line, excites a forward-propagating mode composed of several Bloch wavevectors, shown as red dots. It also excites a backward-propagating Bloch mode, shown as green dots. For a certain frequency ω_2, indicated by the light grey dashed line, two Bloch modes would have the same wavevector. Due to reflections at the layer interfaces, these two modes are strongly coupled. The strong coupling causes an avoided crossing in the dispersion diagram, so that a stop gap is created. The stronger the contrast in the refractive indices of the two media, the larger the stop gap [21].

A stop gap can exist in 2-dimensional structures as well. A scanning-electron micrograph of a 2D PhC is depicted in figure 1.5a. Here, a Si membrane is perforated with a periodic arrangement of air holes to create a 2D photonic stop gap. A sketch of the associated band structure is shown in figure 1.5b. The dark grey regions indicate a continuum of allowed photonic states. The region of frequencies between the shaded dark grey regions is the photonic stop gap. When a row of holes is missing in such a structure, i.e. a line defect is introduced, another solution of the wave equation is created, in the stop gap. This solution is a new mode of the structure, located at the line defect: the missing row of holes acts as a waveguide for light. An image of the waveguide and the associated dispersion diagram are shown in figure 1.5c and d. The red line indicates the waveguide mode. Light is confined to the waveguide core, with an evanescent tail in the hole structure.

The mode in the waveguide exhibits very strong dispersion, i.e. the wavevector is highly dependent on the optical frequency. The group velocity of light, v_g, is given by the slope of the dispersion curve:

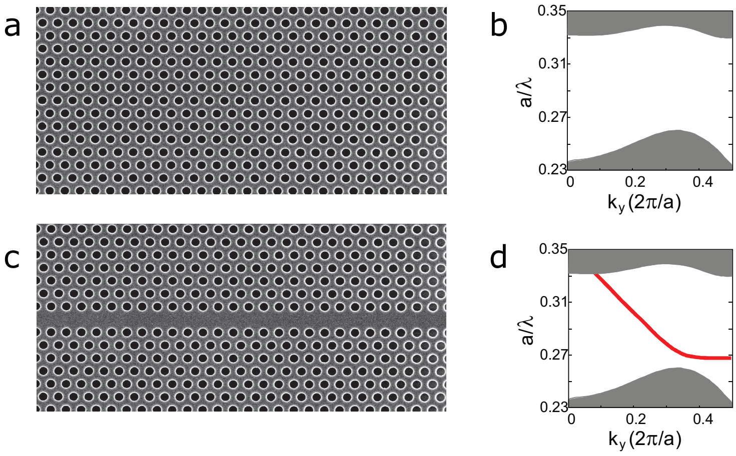

Figure 1.5: Photonic crystals and their associated dispersion diagrams. a) A scanning electron micrograph (SEM) of a photonic crystal. A periodic arrangement of holes is etched into a Si membrane. b) The dispersion diagram of the PhC. The grey areas indicate a continuum of allowed photonic eigenstates. The white region between the shaded regions is the photonic bandgap. c) An SEM of a PhC waveguide. A row of holes is left missing to create the waveguide. d) The dispersion diagram of the PhC waveguide. The red line indicates the waveguide mode.

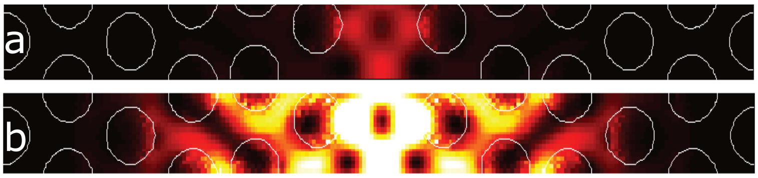

Figure 1.6: Mode profiles in a photonic crystal waveguide. Shown is one unit cell of the photonic crystal. The white circles represent air holes in the Si membrane. The waveguide is formed by the missing hole in the middle of the image. a) The electric field intensity for fast light ($v_g = c/15$). The mode is confined to the waveguide core. b) The electric field intensity for slow light ($v_g = c/150$). The mode extends laterally into the crystal lattice. The electric field intensity rises proportionate to the group index. The plots are results of 3-dimensional FDTD simulations, courtesy of T. P. White.

$$v_g \equiv \frac{\partial \omega}{\partial k}. \tag{1.4}$$

At $k = \pi/a$, the slope of the dispersion tends to zero, so that light is slowed down at the corresonding frequencies. The phenomenon of slow light has drawn a lot of attention [7, 25], due to wide-spread applications, ranging from optical delay lines [26], buffers [27], and switches [28, 29], to enhanced nonlinear optics [30]. The point at which the slope of the dispersion curve reaches zero is called the photonic band edge.

1.2.2 Coupling to slow light in photonic crystal waveguides

At frequencies near the band edge in a photonic crystal waveguide, where the propagating mode exhibits strong dispersion, the group velocity of light is reduced. Slow light behaves differently from fast light in several respects.

In 2D PhC waveguides, the mode profile of fast light is different than the mode profile of slow light. To illustrate the difference, we refer to figure 1.6. The figure depicts the intensity of the electric field, resultant from a 3D FDTD numerical simulation. The image portrays one unit cell of the photonic crystal waveguide. The white circles represent air holes etched in a Si slab. The waveguide is formed by the missing hole in the middle, i.e. the mode propagates in the vertical direction. Figure 1.6a depicts the intensity in the fast light regime, where the group velocity of light is $v_g = c/15$.

In this regime, the mode is confined to the waveguide core, with a full width half maximum on the order of a lattice constant. In the slow light regime, where $v_g = c/150$ (figure 1.6b), the electric field intensity profile differs dramatically. The mode extends laterally far into the crystal, with the full width half maximum on the order of 5 times the lattice constant. Additionally, the intensity is higher in the slow light regime. In fact, it is predicted that, disregarding losses, the intensity increases linearly with group index [31, 32]. In a PhC waveguide with two sections, one of which supports a fast mode and the other a slow mode, the difference between mode profiles and the difference in intensities in the two sections results in an effective impedance mismatch [33]. To avoid reflections and increase the efficiency of energy transfer to slow light, the impedance needs to be matched on the boundary.

1.2.3 Multiple scattering and localization in photonic crystal waveguides

In an ideal PhC waveguide, light can be slowed down to group velocity zero. Recently, however, it has become apparent that multiple scattering introduces limitations to the usefulness of practical PhC waveguides at speeds smaller than $v_g \sim c/35$ [32, 34, 35], where c is the speed of light in free space. When the group velocity is reduced in a PhC waveguide, light starts to interact more strongly with the structure it propagates in [36, 37, 38]. Photons scatter off any imperfection in the crystal lattice. For sufficiently strong interactions, light can become localized in space, due to Anderson localization [39]. In this case, multiple scattering events result in interference which localizes light in a small spatial region in the waveguide [40]. Anderson localization is a universal wave phenomenon, with manifestations in electron transport [39, 41], sound [42], matter waves [43, 44] and light [45].

Localization length, L_{loc} is an important parameter in localization studies. In a randomly scattering 1D sample, localization occurs when L_{loc} is smaller than the length of the sample [39]. In the localization regime, the transmission of a sample is strongly impeded. When L_{loc} is larger than the sample length, light propagation is unperturbed by scattering. Finally, when L_{loc} is on the order of the sample length, light propagation is on the verge of the localization regime [35]. In this regime, random cavities are still formed in the waveguide, however their bandwidths are broader (corresponding to lower Q's) than in the localization regime. Transmission is intermittent, because in some spectral regions the cavities overlap, and in others they don't. Hence, to determine the usefulness of a waveguide, it is very important to measure the localization length.

1.3 Phase- and polarization-sensitive near-field microscope

One of the key properties of nano-optics is the presence of evanescent waves. In section 1.1.1, we showed that confinement of optical fields beyond the diffraction limit in a given spatial direction can be achieved when the wavevector in that direction exceeds the total wavevector in free space. In that case, for equation 1.3 to still be valid, the wavevector in an orthogonal direction becomes purely imaginary, meaning that the electric field in the orthogonal direction decays exponentially. The ability to confine optical fields beyond the diffraction limit is the basic principle of nano-optics [46].

In this thesis, we consider situations in which there is a wave propagating in one or two spatial directions and exponentially decaying in another. Examples are a plasmonic waveguide (Chapters 2 and 3), surface plasmons on a gold film (Chapter 4), or light in a photonic crystal waveguide (Chapters 5 and 6). In each case, we probe the evanescent wave to get a measure of the electric field of the propagating wave. We probe the electric field with a near-field microscope [47].

A near-field microscope works by introducing a subwavelength-sized probe into the evanescent field of the wave. If the probe scatters the field into free space, to be collected by a detector, the microscope is called scattering-type [48]. On the other hand, if the probe contains a small aperture at the end of a fiber through which the field is picked up, the microscope is called collection-type [49]. In this thesis, we use a collection-type near-field microscope.

A scanning-electron micrograph (SEM) of a near-field aperture probe is depicted in figure 1.7a. The probe is made from an optical fiber, which is first heated in the middle with a CO_2 laser while being pulled on both ends. The heating/pulling procedure is continued until the fiber breaks. What remains on each side of the breaking point is a glass tip, with a radius of curvature of $\approx 20\,\text{nm}$. Next, the tip is coated with a layer of aluminum with a thickness of ≈ 150 nm. The final step in probe fabrication is to cut

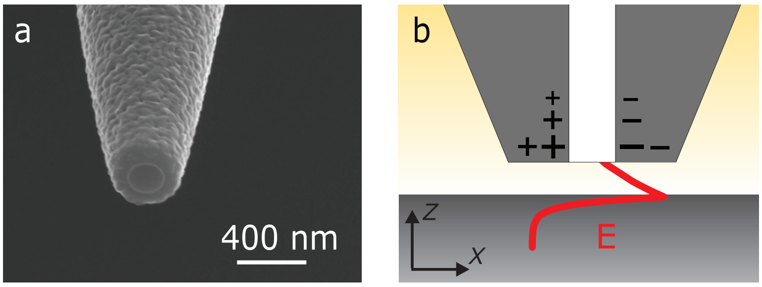

Figure 1.7: Geometry of the near-field probe and its principle of operation. a) A scanning-electron micrograph of the probe. The circular glass aperture has a diameter on the order of 150 nm. The aluminum coating has a thickness of 150 nm. The coating prevents light entering the probe at any other position except through the glass aperture. b) The principle of operation of the probe. The grey and yellow areas are materials of different dielectric constants. An optical wave propagates in the x direction and is evanescent in the z direction. The evanescent tail of the wave's electric field (marked in red) polarizes the aperture, as indicated by positive and negative charges in the coating. The aperture re-radiates into propagating modes of the fiber (not shown in the image).

the end of the probe with a focused-ion beam, so that what remains is a circular glass aperture with a diameter on the order of 150 nm, surrounded by the aluminum coating.

The principle of operation of the aperture probe is sketched in figure 1.7b. The grey area indicates a semi-space with dielectric constant different from that of the yellow semi-space. An optical mode propagates at the interface, in the x direction, and is evanescent in the z direction. The x-component of the electric field of a sample is portrayed by the red line. In this illustration, the field peaks at the interface. The probe is brought into the evanescent field of the sample. The probe-sample distance is controlled with a shear-force feedback loop (not shown in the image), and is kept at about 20 nm [50]. The probe needs to be kept as close as possible to the surface, without touching it, for maximum signal and to prevent damage to the probe, respectively. The electric field polarizes the probe aperture, as indicated by positive and negative charges in the figure. The glass core at the apex of the probe is too small to support propagating

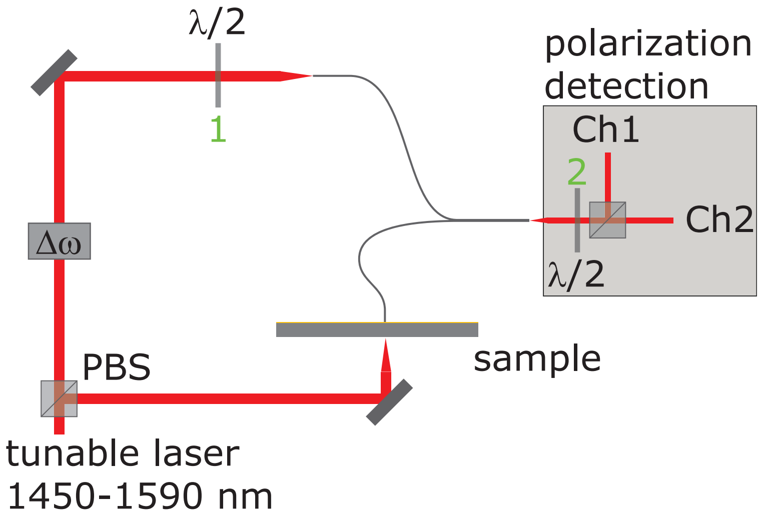

Figure 1.8: A schematic of the phase- and polarization-sensitive near-field microscope. A laser beam is incident from the bottom. It is split by a polarizing beam splitter (PBS) into the sample branch and the reference branch. The sample branch excites a wave in the structure. The evanescent tail of the wave is collected by the aperture probe and guided down the probe fiber. The probe fiber is mixed with the reference branch. Before mixing with the signal branch, the reference branch is frequency-shifted by $\Delta\omega$*, using acousto-optic modulators. This allows for heterodyne detection, which increases sensitivity. The polarization detection scheme consists of wave plates, a second PBS and two photodetectors.*

fiber modes, however the core expands away from the apex. The near field of the polarized core extends in the z direction to the cutoff point, where propagating modes exist in the fiber. At this point, the near field excites these propagating modes, which carry the signal through the fiber towards a photodetector. For more details, see [51].

A schematic of the phase- and polarization-sensitive near-field microscope is depicted in figure 1.8. A laser beam, shown as a red line, is incident from the bottom. In this thesis we use a continuous-wave laser source (HP/Agilent 8168F), tunable between 1450 nm and 1590 nm. The beam is split by a polarizing beam splitter (PBS) into two branches. One branch goes to the sample and excites the wave which we want to investigate. The near field of the wave is collected with a probe, as described above, and guided by the probe fiber. The other branch of the beam, which we will call the reference branch, does not go to the sample. Instead, it is sent through a pair of acousto-optic modulators (AOMs) and a half-wave plate ($\lambda/2$), labelled with a green “1”, before being mixed in a fiber with the sample branch. The AOMs are modulated at frequencies which differ by $\Delta\omega = 40\, kHz$, such that the sample and reference branch beat with that frequency. The beat frequency is fed into a lock-in amplifier to which the photodetectors are connected. In this way, sensitivity of detection is greatly enhanced, in what is termed heterodyne detection [52, 53]. After they have been mixed, the sample and reference branch together go through another half-wave plate, labelled with a green “2”, are split by a second PBS and sent to two different detectors, noted as Ch1 and Ch2. The polarization detection scheme, together with half-wave plate 1, allows for the detection of the orientation of the in-plane electric field vector [54, 51]. For example, if we are studying a plasmonic slot waveguide, we would like to measure in Ch1 the electric field component orthogonal to the waveguide, and in Ch2 the electric field component parallel to the waveguide. These two electric field directions are indicated by the red coordinate system in figure 1.9. The reference beam is linearly polarized, but the direction of polarization makes an arbitrary angle with the red axes. The direction of polarization of the reference beam is indicated by the blue arrow. To detect the electric field parallel to the waveguide and that orthogonal to the waveguide with equal sensitivity, we rotate the polarization direction of the reference branch such that it makes an angle of 45° to the red axes. This is performed by setting the half-waveplate “1”. The black dashed axes in the figure indicate the coordinate frame set by the second PBS and the two detectors. To ensure that the detection channels align with the electric field components which we want to measure, we rotate the red coordinate frame by setting half-waveplate “2”, as shown in the image.

1.4 Outline of this thesis

In Chapter 2 we use the near-field microscope to measure symmetry properties of plasmonic slot waveguides. For a waveguide only 40 nm wide, we find only one propagating mode. This mode is found to be anti-symmetric, with opposite charges facing each other across the gap. The anti-symmetric

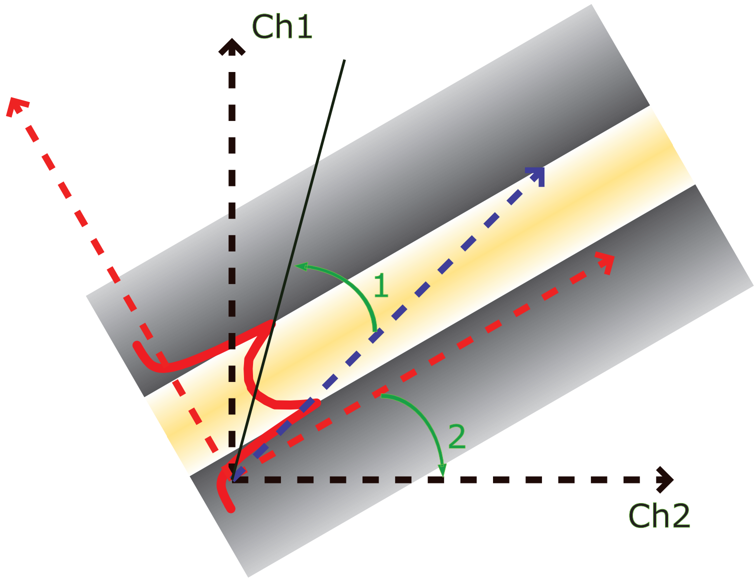

Figure 1.9: A schematic of the polarization detection scheme. We use an MIM waveguide sample for illustration purposes. The desired electric field directions to be measured are indicated by the red arrows. The thin black line indicates the 45° angle between these two arrows. The polarization in the reference branch, indicated with the blue arrow, is rotated by using waveplate "1", such that it overlaps the thin black line. The polarization of the reference branch and the red coordinate frame together are rotated using waveplate "2", to ensure that the desired field components are mapped onto detection channels 1 and 2, indicated by the black coordinate system.

nature is supported by numerical calculations. We anticipate the symmetry of modes in narrow plasmonic waveguides to become important in the fields of nonlinear optics and integrated quantum optics.

In Chapter 3, we investigate losses of a plasmonic nanowire waveguide due to bends. We separate bending losses from propagation losses and find exponential dependence of losses on radius of curvature. We find that for curves with bending radii down to 4 μm, the bending losses are negligible compared to the propagation losses of a straight waveguide. The bending losses become the dominant loss component for radii smaller than 2 μm. Such basic studies are necessary for future integrated optical and plasmonic circuits.

Chapter 4 describes the launching of surface plasmon polaritons by a chain of subwavelength holes in a gold film. We study the intricate pattern formed by interference of SPPs launched by each individual hole and resolve the plasmonic Talbot effect. We find that the Talbot effect occurs at distances different than expected from the paraxial approximation and suggest a correction to the approximate Talbot equation. We study the evolution of the Talbot effect as we increase the number of holes. We also find that the ratio of excitation of different diffraction orders can be controlled by the polarization of the incident beam. Localized hotspots are generated, with relevance to sensing and integrated quantum optics.

In Chapter 5, we study the interface between fast and slow light photonic crystal waveguides. We find an evanescent mode at the interface, which is predicted to be responsible for efficient coupling to slow light. Efficient coupling to slow light is of paramount importance to its use in optical circuitry.

In Chapter 6, we study localized states in a photonic crystal waveguide. We show that we can measure the localization length via a magnetic interaction with a near-field probe. The localization length reveals whether light is strongly localized, which is important for determining the usefulness of waveguides.

In Chapter 7, we propose a number of applications and research directions based on results given in this thesis. We discuss designs for efficient coupling to guided plasmons in a slot waveguide, a plasmonic polarization demultiplexer, addressing single emitters for quantum optics, trapping atoms near nanostructures, and applications of efficient coupling to slow light to optical switching and delay lines.

2

Modal symmetry in plasmonic slot waveguides

ABSTRACT: Plasmonic slot waveguides are versatile submicrometer sized plasmonic devices. They are readily fabricated on glass substrates and can assist in various interactions between the light field and matter. The symmetry of the electric field in a waveguide plays a crucial role in the interactions. With a phase- and polarization- sensitive near-field microscope, we measure the electric field in the waveguide for a range of slot widths, from 40 nm to 120 nm. The field is experimentally found to be antisymmetric across the slot gap. Numerical calculations confirm this symmetry. Calculations also show a confinement of the field to a lateral size ∼10 times smaller than the free-space wavelength. Our results will be significant for the field of quantum plasmonics, for which the symmetry of the electric field is crucial.

2.1 Introduction

Strong electric fields can be achieved by coupling the SPP modes of two parallel metal surfaces in an MIM waveguide. In contrast to purely dielectric optical waveguides, in which some evanescent field inevitably extends into the surrounding material [55], most of the electric field in an MIM waveguide is confined to the core, even for arbitrarily narrow spacings between the two metal surfaces. Similar confinement exists also in triangular channel guides [56] and a slot in a metal film, in which SPPs on the sides of the slot couple to form a guided mode that is confined to the core in two dimensions[57, 58, 59, 60, 61]. The ability to access the waveguide from the air side and introduce materials or particles into the gap opens up many potential applications. The strong field enhancement between two metal surfaces can be used to sense the presence of molecules [62], or to produce nonlinear effects [63, 64, 65, 66]. The associated small mode volume could be useful for coupling the emission of individual quantum emitters introduced into the gap to guided modes, which may lead to a nanoscopic source of light on a chip [67].

When considering any near-field interaction between matter and waveguide modes, the distribution and symmetry of the field must be carefully studied. In this Chapter we report near-field measurements of the spatial symmetry of the electric field in a plasmonic slot waveguide. We show that there is only one mode in waveguides of height and width considered in this work. The field of this mode is such that it sets up opposite charges across the gap, i.e. the mode is antisymmetric [68]. Numerical calculations confirm this symmetry and indicate subwavelength confinement of the mode. Although there have been several far-field input/output studies of plasmonic slot waveguides at optical frequencies [59, 69, 70, 71, 72], none of those provide direct information about the symmetry of the mode.

2.2 Experiments

2.2.1 Experimental details

Slots are fabricated by focused ion beam (FEI Helios) milling in a layer of gold, which was evaporated by physical vapour deposition on a BK7 glass substrate. The thickness of the gold film is 80 ± 5 nm. Slot widths w range from 40 nm to 120 nm, with a fixed length of 17 μm. The slot width and

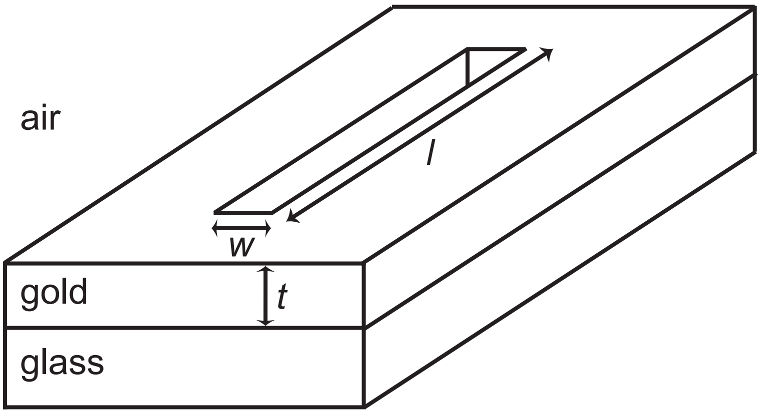

Figure 2.1: A diagram of the structure. The thickness t of the gold film is 80 ± 5 nm. The length l of the slots is 17 μm. The width w of the slots ranged from 40 nm to 120 nm.

length were measured with a scanning electron miscroscope. A diagram of the sample is shown in figure 2.1 Continuous wave laser light from a commercial telecom laser is focused to a spot with a diameter of ~10 μm (1/e in amplitude). The light impinges through the glass substrate, perpendicular to the gold layer. The free-space wavelength used in the experiment is 1.55 μm. At this wavelength, the dielectric constant of gold was experimentally determined by ellipsometry to have a value of -115.67+11.34i, and the dielectric constant of the substrate is 2.25. The light is linearly polarized orthogonal to the long axis of the slot. A phase- and polarization-sensitive near-field microscope [52, 54] is used to image the electric field from the air side of the gold film.

2.2.2 Measurement results

Figure 2.2 shows the measured amplitude and phase of the electric field component orthogonal to the long axis of the slot. The slot extends from the top left to the bottom right corner of the image, making an angle of ~15 degrees with the x-axis. The amplitude, figure 2.2(a), above the slot peaks in the middle of the slot, corresponding to the excitation beam. A modulation is superimposed on the amplitude, with a measured period of 1.0 ± 0.1 μm. The phase image, figure 2.2(b), shows a similar distribution

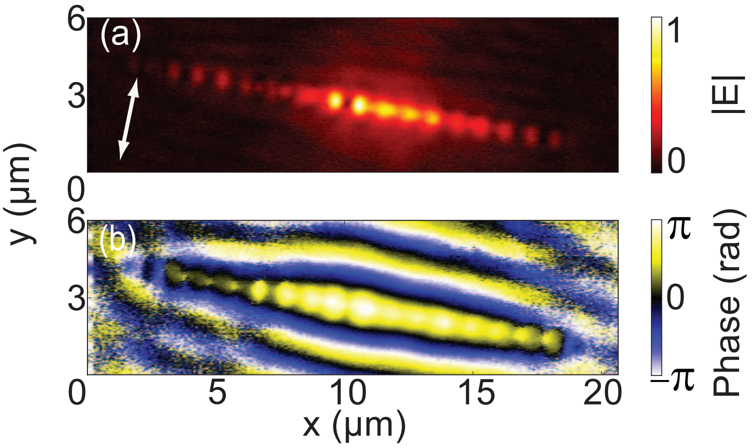

Figure 2.2: The measured near-field amplitude (a) and phase (b) of the electric field component orthogonal to the long axis of the slot, as indicated by the white arrow. The slot makes an angle of ∼15 degrees with the x-axis. The amplitude follows the excitation beam profile, with a superimposed modulation. The modulation period is 1.0 ± 0.1 μm.

as the amplitude image in the slot area. The wavefronts parallel to the slot are waves with a wavelength of ∼1.5 μm, propagating to the top and bottom of the image. These are surface plasmon polaritons excited at the slot, propagating on the smooth gold/air interface.

When the component of the electric field parallel to the slot waveguide is measured (figure 2.3), only a modulation is observed. The field exhibits a node along the center of the slot. The modulation period of 0.5 ± 0.1 μm, best observed close to the slot ends, is twice as fast as the one observed for the perpendicular field direction (figure 2.2(a)). The phase in figure 2.3(b) and (c) varies with a period of 1.0 ± 0.1 μm. The two opposite metal edges of the slot are found to be in anti-phase. This indicates that the wave which gives rise to the observed pattern along the slot sets up opposite charges across the slot gap.

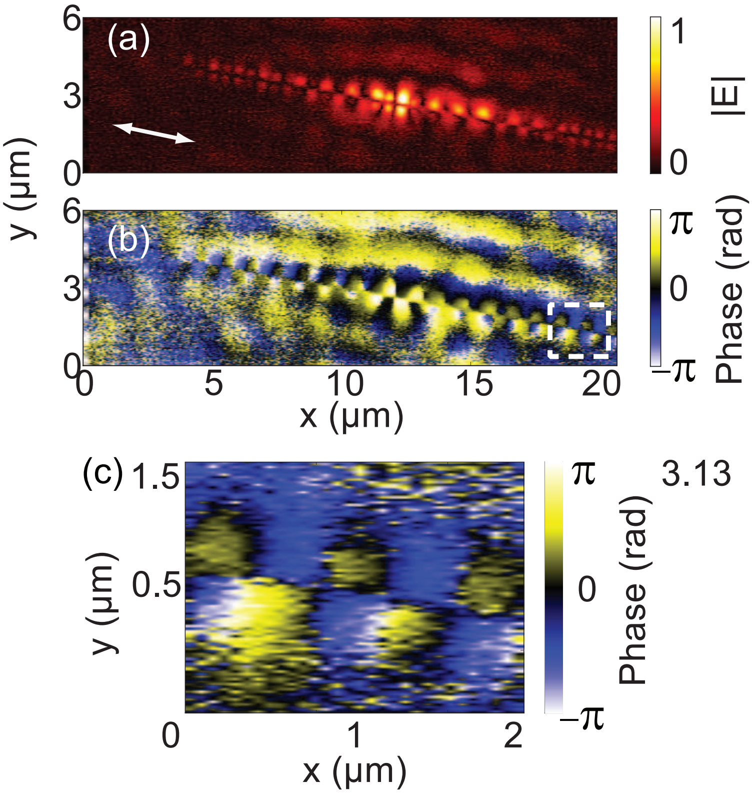

Figure 2.3: The measured near-field amplitude (a) and phase (b) of the electric field component parallel to the long axis of the slot, as indicated by the white arrow. A closeup of the part of the phase image which is surrounded by a dashed white rectangle is shown in (c). The field is antisymmetric, with opposite phases facing each other across the slot. The amplitude is modulated with a period of 0.5 ± 0.1 μm.

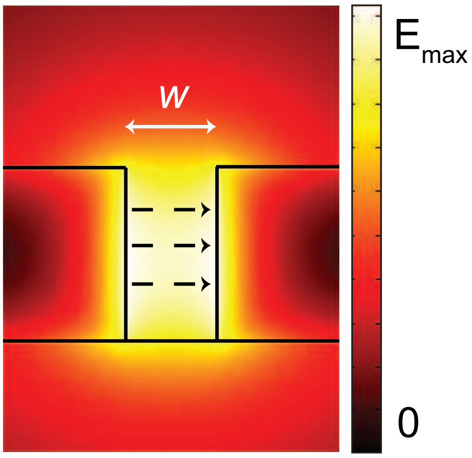

Figure 2.4: Amplitude of the electric field obtained from the finite element method solver. Shown is a crosscut through the waveguide. The width w of the waveguide is 40 nm. The field is localized to the air gap. The electric field lines point across the gap, as indicated by dashed black arrows.

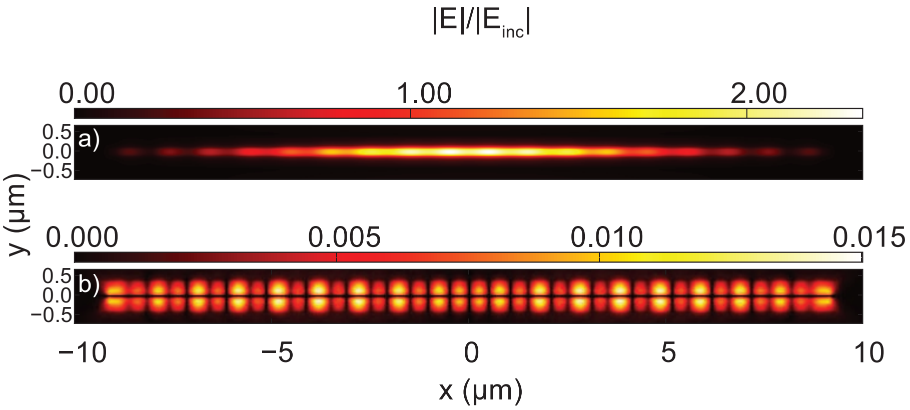

Figure 2.5: Results of the finite-difference time-domain simulation for a slot 17 μm long. Amplitude of the perpendicular (a) and parallel (b) component of the electric field, 10 nm above a slot with a width of 40 nm. The excitation spot has a Gaussian profile, with a waist of 10 μm. The simulated fields show agreement with the measurements of figure 2.3(a) and 2.5(a).

2.3 Discussion

To clarify the results further, a finite element method (FEM) solver (COMSOL) is employed to find the allowed modes of the structure. At widths smaller than ∼200 nm only one physical solution is found, which has most of the electric field confined to the slot. This is different from the critical slot width of ∼1 μm found by Pile and co-workers [68], because the gold film in our case is much thinner than the 400 nm used in that work. With the calculation, we also verify the measured symmetry. The electric field resulting from the FEM simulation for a 40 nm wide waveguide is shown in figure 2.4. The measured lateral extent of the mode (∼600 nm full width at half maximum, FWHM) is larger than the calculated one (150 nm FWHM), which we attribute to the finite size of our near-field probe. The electric field is confined to a lateral size ∼10 times smaller than the free-space wavelength. The symmetry of the mode is such that electric field lines point in the direction shown by the dashed black arrows in figure 2.4.

The match in the calculated and measured modal symmetry indicates that we are indeed observing the plasmonic slot mode in the waveguide.

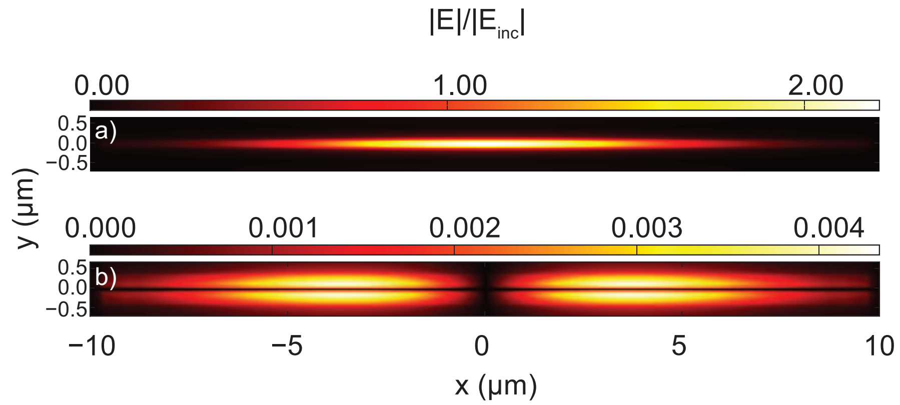

Figure 2.6: Results of the finite-difference time-domain simulation for a slot much longer than the size of the laser spot. Amplitude of the perpendicular (a) and parallel (b) component of the electric field, 10 nm above a slot with a width of 40 nm. The modulation seen for shorter slots is absent, which points to scattering off the short edges of the slot as the excitation mechanism.

However, the FEM calculation only shows allowed solutions to Maxwell's equations for a given geometry, hence it does not provide insight into the excitation mechanism and the origin of the modulation in the amplitude images of figure 2.3(a) and 2.3(b). To understand the situation further, we perform finite-element time-domain (FDTD) simulations with the Lumerical Solutions FDTD software. In the simulation, we fix the width of the slot to 40 nm, and vary the slot length and the width of the laser spot. It is observed that for our experimental situation, a 17 μm long slot and a 10 μm wide (1/e in field) incident beam, the simulation qualitatively reproduces the measured field patterns (figure 2.5). The top part of the figure, which shows the amplitude of the electric field component perpendicular to the slot, shows a weak modulation with a period of $\sim$1.02 μm, which is approximately λ_{SPP}, the calculated wavelength for this slot width. This is the same period which we experimentally observe for the corresponding field component (figure 2.2(a)). The simulated amplitude of the field component parallel to the slot (figure 2.5(b)) displays two superimposed periods. Besides the periodicity corresponding to λ_{SPP} also observed for the perpendicular field direction in figure 2.5(b), now an additional periodicity corresponding to $\lambda_{\mathrm{SPP}}/2$ is present, which can be seen most clearly in the middle of the slot. The contrast of the modulation is found to increase for shorter slots and wider laser spots. For longer slots, the contrast of the beating decreases, until finally, in an infinitely long slot, the beating vanishes, as shown in figure 2.6. We therefore conclude that scattering at the slot ends into the plasmonic mode is the excitation mechanism, even though the amplitude of the incident laser at the slot ends is small. The periodicity corresponding to $\lambda_{\mathrm{SPP}}/2$ in the amplitude pattern is then the result of two counterpropagating modes, each launched by one of the slot ends. Due to the high amplitude of the directly transmitted beam, and the relatively weak amplitude of the plasmonic field, the directly transmitted light influences the pattern observed for both field components. The interference between the directly transmitted beam, which has a nearly constant phase along the length of the slot, with the plasmonic slot mode, results in the modulation of the amplitude with a periodicity corresponding to λ_{SPP}. It is now obvious that figure 2.2(a) shows primarily a λ_{SPP} modulation of the amplitude because the transmitted light dominates for the electric field component orthogonal to the long slot axis. On the other hand, for the electric field component parallel to the long slot axis, simulations show that the exact area where the periodicity corresponding to λ_{SPP} dominates the amplitude over the periodicity corresponding to $\lambda_{\mathrm{SPP}}/2$, as well as the shape of the interference pattern, strongly depend on the position of the center of the beam with respect to the slot ends. This can be understood when we consider that moving the excitation spot closer to or further away from one of the slot ends will change the amplitude and phase relation between the different contributing modes and the transmitted beam. Thus a slight offset of the incident beam with respect to the center of the waveguide can explain the discrepancies between figure 2.3(a) and figure 2.5(b).

2.4 Conclusion

In conclusion, we have excited a plasmonic mode in a subwavelength slot in a gold film. We observed the electric fields of the mode with phase and polarization sensitivity, showing that the mode is antisymmetric, i.e. opposite charges face each other across the air gap. Due to its high confinement, we expect that this mode can be of great use for 2-dimensional plasmonic interconnects, sensing, and quantum plasmonics. The existence of only one mode in the waveguide results in well-known positions of field maxima and minima, which will have to be considered when using such a slot for sensing or interaction with single emitters. The node of the electric field in the middle of the gap, which directly results from the antisymmetric nature of the mode, will affect any particles inserted into the slot. For further improvement of the device, we foresee the need for controlled coupling to this mode, perhaps similarly to the adiabatic coupling to nanowire waveguides [73]. An alternative would be to couple to this mode from a dielectric slot waveguide with the same symmetry, as was shown recently [74].

3

Bending losses in plasmonic nanowire waveguides

ABSTRACT: Metallic nanowires are a good candidate for submicrometer sized plasmonic waveguides. They are readily fabricated on glass substrates and can be efficiently coupled to. The subwavelength extent of plasmonic nanowire modes makes the notion of creating complex plasmonic circuits attainable. Losses of waveguides in tight bends will be an important issue for any future plasmonic circuit. We study bending losses of curved plasmonic gold nanowire waveguides for radii of curvature ranging from 1 to 12 μm. We use near-field measurements to separate bending losses from propagation losses. The bending losses scale exponentially with radius of curvature. We find attenuation due to bending losses to be 0.1 μm^{-1} for a curved waveguide with a width of 70 nm and a radius of curvature of 2 μm. Experimental results are supported by Finite Difference Time Domain simulations. An analytical model developed for dielectric waveguides is used to predict the trend of rising bending losses with decreasing radius of curvature in plasmonic nanowires.

3.1 Introduction

In the field of optical data processing, the integration of discrete photonic components on a chip has been a long-standing goal. Micrometer-scale waveguides, switches [75, 28], delay lines [76], and routers [77] have been realized in various silicon-based materials. As more such components are fabricated on small areas, bending losses start to play an important role. Bending losses have been studied experimentally in photonic crystal [78, 79, 80], silicon [81], and silicon-on-insulator (SOI) [82] waveguides.

Recently, subwavelength confinement has been realized with SPP optics [83], which could offer an alternative way to guide light on the submicron scale. By using a strip of metal, plasmons can be confined to two-dimensional metal waveguides [84]. Further modifications of the number and shape of metal-dielectric interfaces resulted in high-confinement SPP waveguides, such as triangular wedges [85], dielectric stripes on metal [86], slot waveguides [69, 20, 87, 60], and metallo-dielectric fiber waveguides [88]. Basic integrated plasmonic components such as interferometers and ring resonators have been successfully demonstrated in channel plasmon waveguides [56]. Transmission through S-shaped bends [89], splitters [90], and directional couplers [91] has been shown in dielectric stripes on metal. In addition metal nanowires can support guided plasmonic modes for arbitrarily small non-zero radii [88, 92]. Verhagen et al. showed that such nanowires, with a width as small as 60 nm, can be fabricated on a chip and efficiently coupled to from the far field [73].

In this Chapter we present a study of bending losses in plasmonic nanowire waveguides. We use the adiabatic coupling scheme demonstrated in [73] to excite nanowire plasmon polaritons (NPPs) on wires with widths of 70 nm and 40 nm. The NPPs propagate through bends with radii of curvature (R_C) ranging from 1 to 12 μm. With a phase- and polarization-sensitive near-field microscope we measure the electric field in the wire in both straight and curved segments. We determine the transmission through the bends as a function of R_C. We use the straight wire segments to measure propagation losses due to Ohmic damping and surface roughness, and then subtract that from the overall transmission losses in bends to reveal pure bending loss. Our data is supported by Finite Difference Time Domain (FDTD) modeling. A simple analytical model is used to describe the trend of the bending losses as a function of R_C.

3.2 Sample fabrication and near-field measurement

The gold nanowires are fabricated on a glass (BK-7) substrate using electron beam lithography. A 150 nm thick positive-resist layer (Zep520) is spin coated onto the substrate, after which a conductive polymer layer (necessary for electron beam exposure) is spin coated on top of the resist layer. After exposure the sample is developed in N-amyl acetate, removing all the exposed resist. A 50 nm thick gold layer is evaporated onto the substrate. The remaining resist and gold are chemically removed in a lift-off process, with N-Methylpyrrolidone. The designed structures consist of a grating of subwavelength holes, and a taper which is connected to a curved nanowire waveguide. The grating has a pitch of 1 μm. This pitch is chosen for the excitation of surface plasmon polaritons at the gold/glass interface, with a free-space wavelength $\lambda_0 = 1.55$ μm. A beam of SPPs propagates into the tapered waveguide, and is adiabatically funneled to a nanowire [73]. The nanowire waveguides had a width of either 40 or 70 nm; as measured with a scanning electron microscope (SEM). Figures 3.1 (a and b) depict scanning electron micrographs of typical fabricated nanowire structures. Figure 3.1(b) depicts a straight nanowire section, with a width of 70 nm and figure 3.1(a) depicts a curved section with a radius of curvature of 6 μm. In all the investigated structures, the nanowire waveguides were designed to make a 90^o bend with RC ranging from 1 to 12 μm.

The phase- and polarization-sensitive near-field scanning optical microscope described in Chapter 1 was used to locally probe the electric field. The experiments were performed using an aluminum-coated near-field aperture probe, with aperture diameter of approximately 300nm. Figures 3.1 (c and d) depict a measured near-field electric field amplitude for two different nanowire waveguide configurations: a straight waveguide section (d), and a curved waveguide with $R_C = 6$ μm (c). Figure 3.1(c) depicts SPPs approaching the nanowire from the right, propagating in the direction of the white arrow. We observe that the NPPs propagate along the curved nanowire waveguide without significant leakage of light around the bend.

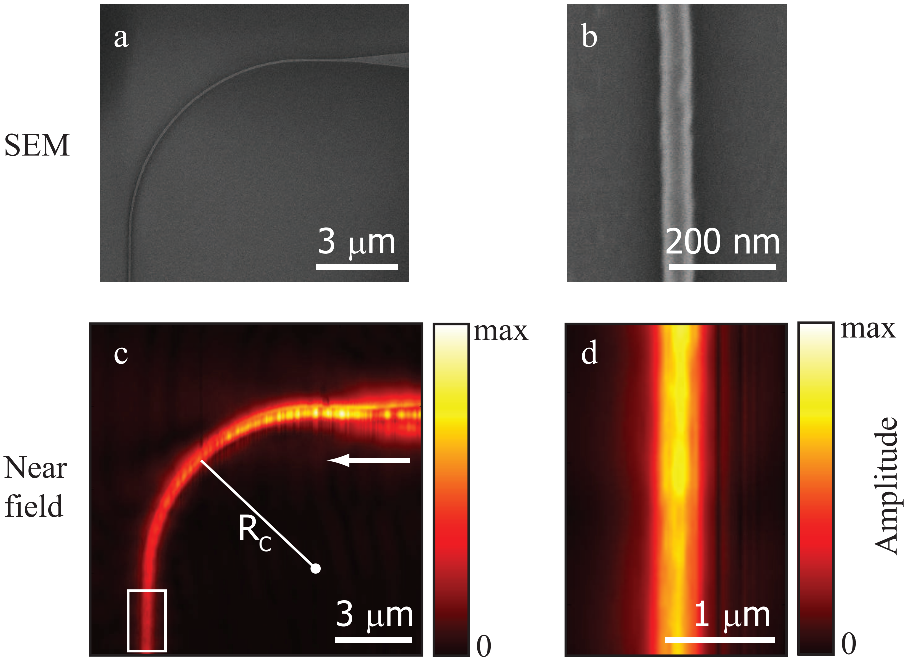

Figure 3.1: Scanning electron micrographs (a and b) and measured near-field amplitudes (c and d) of straight (b and d) and curved (a and c) sections of a 70 nm wide nanowire waveguide. D is an enlargement of a straight section indicated with a white box in c. The radius of curvature of nanowires shown in a and c is 6 µm. The white arrow in c indicates the propagation direction of SPPs on the start of the nanowire bend. The colorbars show the time-averaged electric field amplitude, normalized to the largest measured signal.

3.3 Characterization of losses

3.3.1 Transmission through nanowire bends

Figure 3.2 shows the amplitude transmittance through curved nanowires with a width of 40 or 70 nm as a function of radius of curvature. The amplitude transmittance across the bend is determined by comparing the amplitude before and after a curve. The highest transmittance of 0.53 was observed in the case of a waveguide with a width of 70 nm and a radius of curvature of 2 μm. A general trend of decreasing transmission with increasing radius of curvature can be observed in all studied waveguides. For the general case of lossy waveguides, the intensity drops exponentially with the traversed path. A single exponentially decaying function is fitted to the last three data points in figure 3.2, shown as a dashed line. It is easily noticed that the data point for the smallest R_C lies significantly beneath the fitted line in both cases, which indicates that for small R_C an additional loss component plays a role.

The simplest assumption is that the loss in the bends consists of two components, one for the propagation loss and one for the bending loss. Separating the two components while still keeping the exponential form yields:

$$A_{out}/A_{in} = exp(-k^{''}_{propagation}x)exp(-k^{''}_{bending}x) \tag{3.1}$$

In equation 3.1, $k^{''}_{propagation}$ represents the attenuation of the electric field per unit length due to propagation losses, $k^{''}_{bending}$ represents the attenuation due to bending losses, and x is the length along the waveguide. A_{out}/A_{in} is the amplitude transmittance around the bend, which can also be expressed as $exp(-k^{''}_{total}x)$, where $k^{''}_{total}$ is the total attenuation of the electric field per unit length through the bend.

3.3.2 Propagation losses

In the case of plasmonic structures, propagation losses generally consist of both Ohmic and scattering components. Ohmic losses are due to power dissipated by scattering of electrons inside the metal. Scattering losses are the conversion of power from the propagating mode to free radiation by scattering from surface or bulk imperfections. Both components are present in straight, as well as curved nanowire sections.

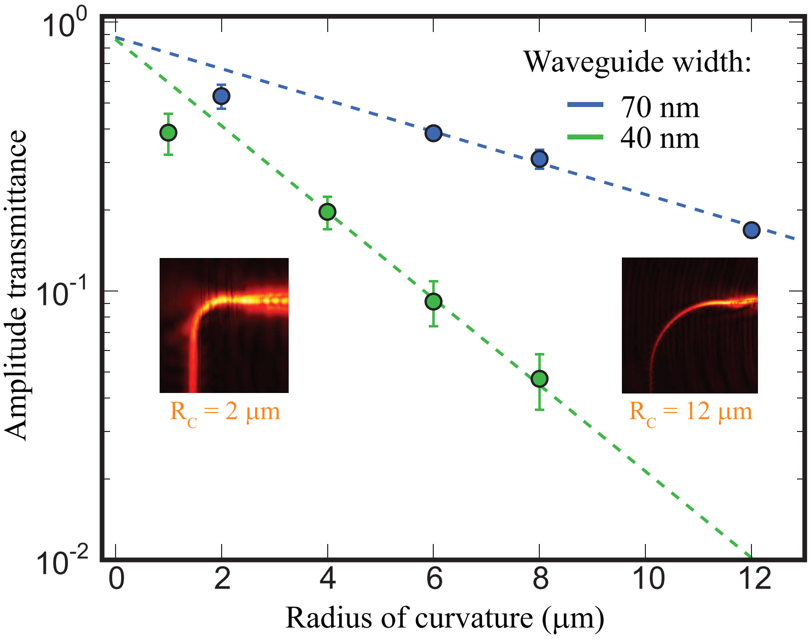

Figure 3.2: Amplitude transmittance through a 90° bend as a function of radius of curvature. Blue and green points correspond to waveguides with widths of 70 nm and 40 nm, respectively. Dashed lines are exponential fits with a single exponent to the last three data points of the near-field amplitude transmittance measurements. The errorbars represent the experimental uncertainty. The insets show near-field amplitude images of two investigated structures.

Comparing the slopes of the fits for the two different waveguide widths in figure 3.2, we observe that the transmission in a 40 nm wide nanowire decreases faster with increasing R_C. In contrast to the case of a dielectric waveguide, where the mode is gradually expelled as the guide is narrowed, in the case of nanowire plasmons the mode retracts into the wire as it gets narrower [88, 92, 73]. Consequently, in narrower waveguides a larger fraction of the mode resides in the metal and hence Ohmic losses are higher than in wider wires. By fitting a decaying exponential function to the amplitude in straight nanowire sections, we obtain average values of $k^{''}_{propagation} = 0.2 \pm 0.05\ \mu m^{-1}$ in 40 nm wide waveguides, and $k^{''}_{propagation} = 0.085 \pm 0.006\ \mu m^{-1}$ in 70 nm wide waveguides. As expected, the propagation attenuation is smaller in the wider waveguide.

3.3.3 Isolating the bending losses

From equation 3.1 and the presented data, we can extract a value for $k^{''}_{bending}$ by substituting x by $R_C/2$ (the path traversed in a 90^o bend). This yields

$$k^{''}_{bending} = -log\frac{A_{out}}{A_{in}}\frac{2}{\pi R_C} - k^{''}_{propagation}. \tag{3.2}$$

In the above equation, we have made the assumption that propagation losses are the same in straight sections of the waveguide as in the curved sections. The assumption is verified with FDTD simulations, which show that the mode profile does not change significantly even in bends with small R_C. A similar mode profile lets us assume that the surface scattering losses are the same for straight and curved waveguide sections. Ohmic losses and bulk scattering losses stay the same, irrespective of bending radius. Figure 3.3(a) depicts the measured attenuation in 70 nm wide waveguides. The total attenuation $k^{''}_{total}$ is measured as described in section 3.3.1, the propagation attenuation $k^{''}_{propagation}$ as described in section 3.3.2, after which $k^{''}_{bending}$ is extracted according to equation 3.2. The rise in attenuation (green circles) for small R_C in figure 3.3(a) corresponds to the drop in amplitude transmittance seen in figure 3.2. Propagation losses (blue circles) remain constant for all waveguides with the same width, apart from small fluctuations, which we attribute to small variations in the width of wires for different realizations. As a result, the attenuation due to bending (orange circles) increases as R_C decreases. At radii of curvature larger than

6 μm, bending losses are negligible compared to propagation losses, however at radii smaller than 4 μm the two loss mechanisms become comparable in magnitude. At curvatures with radii smaller than $\sim 2\ \mu m$, bending losses appear to become dominant.

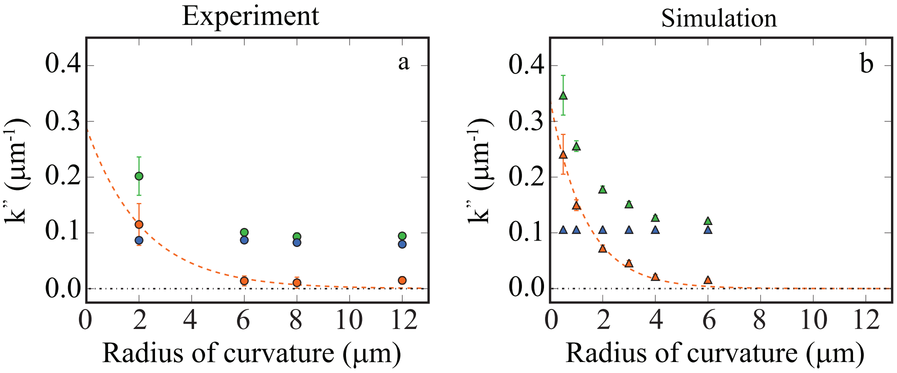

Figure 3.3: Attenuation due to bending losses obtained for waveguides with a width of 70 nm. (a) experimentally obtained values for k''_{total} *(green),* $k''_{propagation}$ *(blue) and* $k''_{bending}$ *(orange). (b) Attenuation values obtained from FDTD simulations. The dashed orange lines indicate the fit to an exponential function. The error bars in the left image represent experimental uncertainty. In the right image, the error bars represent the uncertainty in placing power monitors exactly at the beginning and end of a bend.*

3.3.4 Simulation

We compare the experimental results to FDTD simulations with a commercial simulation software (Lumerical FDTD Solutions v6.5.11). The substrate was modeled as a uniform slab of BK7, with refractive index 1.50066. The permittivity of gold was fitted to a Drude model, around a wavelength of 1.55 μm using optical constants obtained from ellipsometry measurements performed on a similar sample. Perfectly matched layers (PML) were employed around the simulation box to absorb radiated power. The wire cross-section was modeled as a rectangle with a width of 70 nm and a height of 50 nm. A finite difference frequency domain solver, described in reference [93], was used to obtain the mode profile that is used as the excitation source at the intersection of the nanowire with the simulation boundary. The mode has the highest intensity at the surface of the gold wire, which results in strong electric field gradients, especially at the nanowire corners. To ensure that we capture the gradient with sufficient resolution, the mesh size was varied from 10 nm down to 1 nm, while monitoring amplitude transmittance of a straight section of the waveguide. No noticeable change in transmittance occurred while reducing the mesh size from 2 nm to 1 nm. In the final simulation, we used a size of 2 nm for the smallest elements of the simulation mesh. To check whether the absorption of the evanescent tail by the PML affects the results, we varied the size of the simulation box. A distance of 1.2 μm between the structure and the PML was found to be sufficient to obtain reliable results.

The results of the FDTD simulation are shown in figure 3.3(b). Similar to experimental results, the total attenuation (green triangles) rises with decreasing radius of curvature. The attenuation due to bending losses (orange triangles) rises with decreasing R_C, becoming the dominant loss component at a radius of curvature below 2 μm.

3.4 Discussion

A simple model to describe radiation loss in bends leads to bending losses that depend exponentially on the radius of curvature R_C [94]:

$$k''_{bending} = C_1 exp(-C_2 R_C), \text{ where } C_2 = \beta(2\Delta n_{eff}/n_{eff})^{3/2} \tag{3.3}$$

C_1 depends on the dimensions of the waveguide, β is the propagation constant of the mode, and Δn_{eff} is the difference between the modal effective index n_{eff} and the index of the surroundings. Equation 3.3 was derived for dielectric slab waveguides [95], for which electric field intensity decays exponentially outside of the waveguide. In a waveguide curve, at a certain distance X_0 away from the center of the waveguide, the wavevector of the guided light matches that of light freely propagating in the surroundings. The bending losses of the waveguide scale with the fraction of the total modal energy beyond this distance X_0. This leads to exponentially decreasing losses with increasing R_C, as in equation 3.3. In the curved plasmonic nanowires considered in this work, the mode has an effective index slightly higher than that of the glass substrate, hence in a bend the energy primarily leaks into the glass, and not the air. To verify that equation 3.3 is valid in plasmonic nanowire waveguides, we perform simulations to show that the electric field intensity in the substrate decays exponentially outside of the waveguide. In figure 3.4 we show the fraction of the total energy which lies in the glass substrate, outside a distance X away from the center of the waveguide, for straight nanowires with widths of 40 nm and 70 nm. The blue and green data points were obtained from a numerical mode solver (COMSOL). The overlaid red lines are exponential fits. In both cases, the exponential fit matches well to the numerical data, especially at distances close to the waveguide, where most of the energy resides. This observation shows that the assumption underlying equation 3.3 is fulfilled for NPPs just like for dielectric waveguides. We therefore fit equation 3.3 to the experimental and simulated data, shown as dashed orange lines in figure 3.3. Table 3.4 displays the resultant fit coefficients.

At a free-space wavelength of 1.55 μm and for a nanowire width smaller than $\sim 200nm$, the effective mode index rises with decreasing width [73]. As a result, plasmons are better confined to narrower wires (see figure 3.4) and the simulated C_2 is higher at a width of 40 nm than at 70 nm, which results in smaller bending losses. The simulated C_1 is equal for the two widths, which is not surprising since the difference in waveguide widths in the two cases is small. The values extracted from experiments are close to simulation results, although the absolute numbers do not match. As the bending losses become the dominant loss mechanism for only the smallest of the measured R_C, more measurements at radii below 1 micrometer would be required to find the combination of C_1 and C_2 that describes the bending losses best.

The effective index in plasmonic nanowires with a width of 40 nm is only slightly higher than the index in the underlying glass substrate, whereas the index contrast in dielectric waveguides can be significantly higher [82].

Table 3.1: Coefficients obtained by fitting to equation 3.3

	$C_1[\mu m^{-1}]$	$C_2[\mu m^{-1}]$
Experiment (70 nm)	0.289 ± 0.081	0.461 ± 0.140
FDTD simulation (70 nm)	0.348 ± 0.015	0.752 ± 0.048
Experiment (40 nm)	0.638 ± 0.077	0.457 ± 0.096
FDTD simulation (40 nm)	0.361 ± 0.041	1.040 ± 0.012

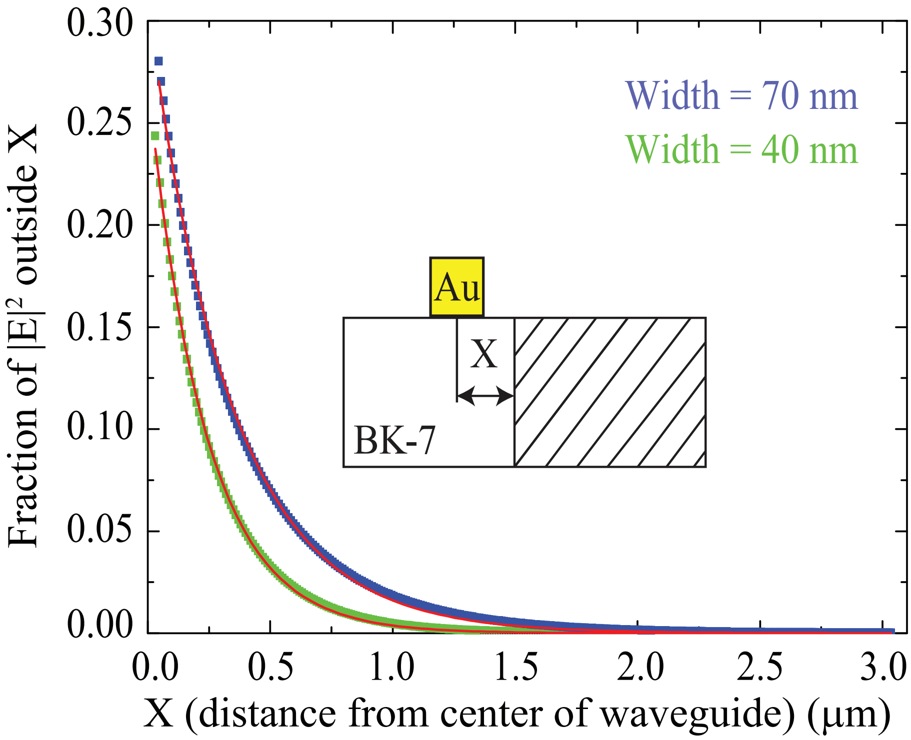

Figure 3.4: The fraction of energy in the substrate. BK-7 is the glass substrate, Au is the gold nanowire. X is the distance from the center of the nanowire waveguide. The green and blue dots are results of numerical simulations for wires of width 40 nm and 70 nm, respectively. The shaded area of the substrate marks the area from which the fraction is calculated. An exponentially decaying dependence on X is observed, which is confirmed with overlaid exponential fits (red lines).

Higher index contrast in dielectrics allows for smaller bending losses at similar radii of curvature [80, 82]. Nevertheless, plasmonic nanowires have smaller footprints and allow for more densely stacked waveguides. Additionally, the effective index in nanowires is predicted to be larger for smaller waveguide widths, and also when the dielectric surrounding is symmetric. This may therefore allow reduction of bending losses at comparable mode confinement.

3.5 Conclusion

In conclusion, propagation losses and bending losses were measured in plasmonic nanowire waveguides with widths of 40 nm and 70 nm. Using a near-field microscope, amplitude transmittances of up to 0.5 were measured in 70 nm wide nanowires with a radius of curvature of 2 μm. Bending losses were isolated from propagation losses. The amplitude attenuation due to bending was found to be as small as 0.1 μm^{-1} in the same wire. Measurements were supported by FDTD simulations. An analytical model developed for dielectric waveguides is employed to describe the losses, which exponentially decay as a function of the radius of curvature. Further improvements in the fabrication procedure could decrease bending losses by generating narrower wires. For applications requiring tight packing of optical waveguides without crosstalk, plasmonic nanowires will be the ideal candidate due to the associated small mode volume. The small volume will additionally be useful for strong coupling to single emitters in the vicinity of nanowires. We thus anticipate the emergence of plasmonic circuits based on this type of nanowire connecting quantum emitters.

4

The Talbot effect for surface plasmon polaritons

ABSTRACT: Subwavelength sized holes in metal films are often used to launch SPPs. The holes are readily fabricated and can also be used to generate a variety of near- and far-field intensity patterns. We use a chain of subwavelength sized holes to launch SPPs onto a gold-air interface. With the phase-sensitive near-field microscope, we visualize the electric field of the excited SPPs. We observe self-images of the chain that we attribute to the Talbot effect. Far from the chain we observe the SPP diffraction orders. We find that when the spacing of the holes is on the order of the wavelength, the revivals do not occur on the well-known Talbot distance. We present an alternative expression for the Talbot distance that does hold for these small spacings. We study the behavior of the revivals and the diffraction orders. We find that the Talbot revivals become more pronounced as the number of holes is increased, which is in accordance with numerical calculations. We anticipate that our findings are interesting for multiplexing sensor applications, where control over the local intensity of SPPs is crucial.

4.1 Introduction

Already in the 1830s, Talbot observed that when a grating is illuminated with a monochromatic plane wave, images of the grating can be observed at certain distances away from the grating [96]. This self-imaging effect, now commonly known as the Talbot effect, was explained much later by Lord Rayleigh [97]. Using the Fresnel diffraction integral he derived the distance z_{T} at which these revivals occur. In the 1950s it became clear that besides the self images observed at integer multiples of the Talbot distance z_{T}, images that are closely related to images of the grating can also appear at rational fractions of the Talbot distance [98, 99]. In the literature this has become known as the fractional Talbot effect. As shown by Berry and Klein, the intensity of the light behind a grating can even, under the appropriate conditions, show fractal behavior [100]. More recently, the Talbot effect attracted the attention of the atomic physics community. It was shown that when a collimated beam of sodium atoms passes through a grating, the distribution of atoms in the beam exhibits self-images of the grating downstream [101]. This effect has been used with great success to create a matter wave interferometer that works with very large molecules [102]. In fact, the Talbot effect appears in any wave diffracted from a periodic structure, which is why Dennis et al. [103] suggested it would also be important when studying the diffraction of surface plasmon polaritons. The Talbot effect has been observed recently for surface plasmons diffracted by a chain of cylindrical nanostructures [104].

In this Chapter, we study the Talbot effect in a surface plasmon polariton field propagating on a gold-air interface. We observe Talbot revivals in the SPP field launched by short chains of up to 11 equidistant subwavelength sized holes. Furthermore, we visualize how the diffraction orders from these chains develop as the number of holes is increased. We show how the number of holes and the polarization of the impinging light can be used to control the distribution of the electric field of the SPPs.

4.2 Experiments

4.2.1 Experimental details

Our sample consists of a BK7 glass slide on which a 88 nm thick gold film has been evaporated. In this film, chains of holes are milled using a focused ion beam (FEI Helios). A scanning electron micrograph of such a chain is shown in figure 4.1(b). The near-field microscope described in section 1.3 is modified to create an elliptical laser spot. Our experimental setup is illustrated in figure 4.1(a). Surface plasmon polaritons are launched onto the gold-air interface by illuminating a chain of holes with light from a diode laser source with a wavelength of 1.5 μm. With a cylindrical telescope and a microscope objective, the laser beam is focused to an elliptical spot with beam waists in the direction perpendicular and parallel to the chain of holes of 4 μm and 40 μm, respectively.

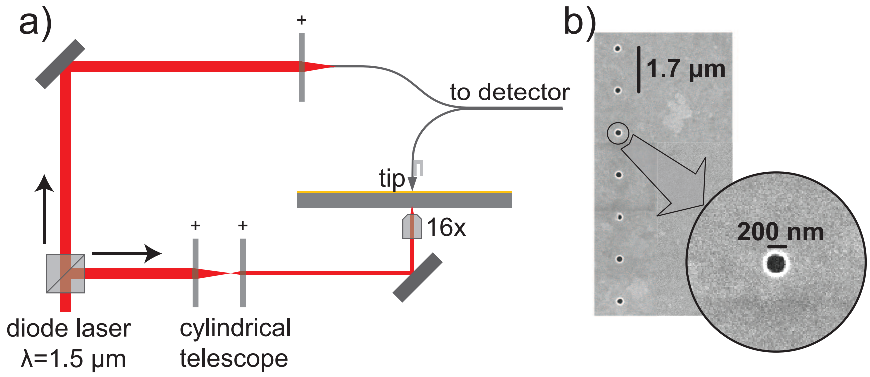

Figure 4.1: (a) Schematic of the experimental setup. Light from a tunable diode laser illuminates the sample from behind. A cylindrical telescope and a 16× *microscope objective are used to create an elliptical focal spot with a 10:1 aspect ratio. A near-field aperture probe is raster scanned over the sample, to map the electric field of the surface plasmon polaritons on the gold-air interface. (b) Scanning electron micrograph showing a part of the sample. The diameter of the holes is* 200 *nm and the period of the chain of holes is* 1.7 *μm*

4.2.2 Measurement results

Typical results of such a measurement are shown in figure 4.2. In this measurement, a vacuum wavelength of $\lambda_0 = 1.5\ \mu$m is used. From the optical constants of gold [105], we can calculate that this corresponds to an SPP wavelength of $\lambda_{\mathrm{SPP}} \approx 1.493\ \mu$m. Note that at this wavelength, the propagation length of the SPP is more than 100 μm, so we expect to see very little damping on the scale of these images. We show images, describing an area of $76 \times 32\ \mu$m, of the electric field of the SPPs launched by a row of 11 holes with a spacing of $d = 1.7\ \mu$m. The amplitude in the images is normalized to the maximum amplitude, which is obtained directly above the holes in figure 4.2(a). In this image the polarization of the impinging light is chosen perpendicular to the chain of holes. We see the 0^{th} and the $\pm 1^{\mathrm{st}}$ SPP diffraction orders (indicated by the green arrows) propagate away from the structure. The diffraction angle of the $\pm 1^{\mathrm{st}}$ orders is found to be $\theta_{\mathrm{out}} \approx 60°$, in good correspondence with the Bragg condition $\sin\theta_{\mathrm{out}} = m\lambda_{\mathrm{SPP}}/d$, where d is the hole spacing and m is the diffraction order. Note that the color scale is chosen such that it saturates at a value of $E/E_{\mathrm{max}} = 0.5$ to show the diffracted orders more clearly. When the polarization is chosen parallel to the chain (figure 4.2(b)), we clearly observe that the 0^{th} diffraction order is strongly suppressed. This suppression is caused by the fact that a circular hole does not launch SPPs in a circular pattern: due to the boundary conditions of the electric field at the edge of a hole, the SPPs are launched mainly in the direction of the impinging polarization [106, 107]. Thus, we can select the order the preferred beam direction of the SPPs by choosing the appropriate polarization and thus externally control the two dimensional intensity pattern formed by the SPPs.

4.3 Discussion

To understand how these diffraction orders develop as a function of the number of holes in the chain, we show the phase of the SPP field launched by a chain of 3, 7, and 11 holes in figure 4.3(a), (b) and (c), respectively. The images each describe an area of $42 \times 16\ \mu$m. The period of the chain is again $d = 1.7\ \mu$m. We note that for 3 holes (figure 4.3(a)), the wavefronts are strongly curved in an almost circular pattern centered around the chain. In contrast, for 11 holes (figure 4.3(c)), almost plane wavefronts are observed in three directions corresponding to the 0^{th} and the $\pm 1^{\mathrm{st}}$ SPP diffraction

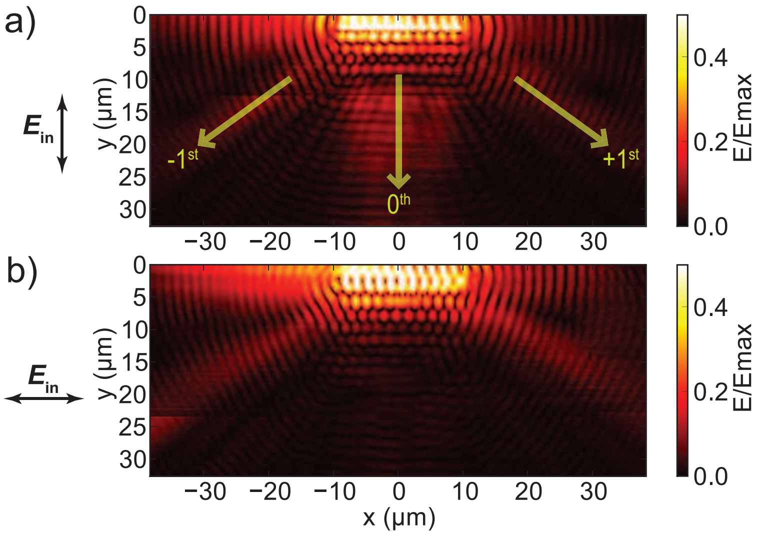

Figure 4.2: Measured amplitude of the electric field of the surface plasmon polaritons (SPPs) launched by a row of 11 holes, for an incident linear polarization that is vertical (a) and horizontal (b). These data were measured with a vacuum wavelength of 1.5 *µm. In both images we see a strong signal directly above the holes (at the top of the images) and the weakly transmitted excitation spot (with a waist of* $w_x \approx 40$ *µm in the horizontal direction and of* $w_y \approx 4$ *µm in the vertical direction) around it. In the case of vertical linear polarization (a), we see a broad beam of SPPs propagating away from the chain in the positive y-direction (indicated as the* 0^{th} *order) and two more narrow beams of SPPs propagating away from the chain under angles of* $\approx \pm 60°$*. In the case of horizontal linear polarization (b), the* 0^{th} *order is suppressed while the* $\pm 1^{\text{st}}$ *orders are enhanced, as expected from the SPP radiation pattern of the individual holes. In both cases, we see a complex pattern of localized hotspots close to the chain.*

orders. In figure 4.3(a) we also see that the phase is blurred in the top middle to left of the image. This is because some of the light from the excitation spot is directly transmitted through the film and detected on the other side, due to the limited thickness of the gold film. The excitation spot can also weakly be seen in the amplitude data shown in figure 4.3(d), where is appears as a weak elliptical spot to the left of the structure.

In figure 4.3(d-f) the amplitude of the SPP field is shown. The amplitude in these images is normalized to the maximum amplitude measured in Fig. 3(f). At the top of these images, we see chains of bright spots. These spots are as bright as they are, because light from the holes is directly picked up by the tip. At a distance of a few micrometers away from the chain, we clearly observe a chain of hotspots in the amplitude parallel to the chain, that has the same period as the chain of holes. These images therefore show the first observation of the Talbot effect for SPPs. In fact, the images show both integer and fractional Talbot revivals. The row of hotspots closest to the chain is horizontally offset, such that the maxima are lined up between the holes. In the row of hotspots below that, the maxima are aligned with the holes. This second row is the first Talbot revival. The first row is laterally shifted with respect to the holes, but has the same period. Importantly, it occurs at roughly half the distance between the chain and the first Talbot revival, which shows that this row is a fractional Talbot revival [98, 99]. It is important to realize that since the distance d in our measurement is on the order of the wavelength, the revivals do not occur exactly at the Talbot distance derived in the paraxial limit by Lord Rayleigh, as suggested in by Dennis *et al.*[103]. When $d < 2\lambda$, it is more appropriate to calculate the Talbot distance by coherently adding up three plane waves corresponding to the SPP diffraction orders of the chain. The electric fields of the three orders are:

$$\begin{aligned} 0^{\text{th}} &: E_0 \propto e^{ik_0 y} \\ +1^{\text{st}} &: E_+ \propto e^{ik_\perp y} e^{ik_\parallel x} \\ -1^{\text{st}} &: E_- \propto e^{ik_\perp y} e^{-ik_\parallel x}, \end{aligned} \tag{4.1}$$

where $k_0 = 2\pi/\lambda$, $k_\parallel = 2\pi/d$, and $k_\perp = \sqrt{k_0^2 - k_\parallel^2}$. The Talbot effect arizes at distances at which $e^{ik_0 y}$ comes back in phase with $e^{ik_\perp y}$. This happens when $(k_0 - k_\perp)y = 2\pi n$, so that the Talbot distance is:

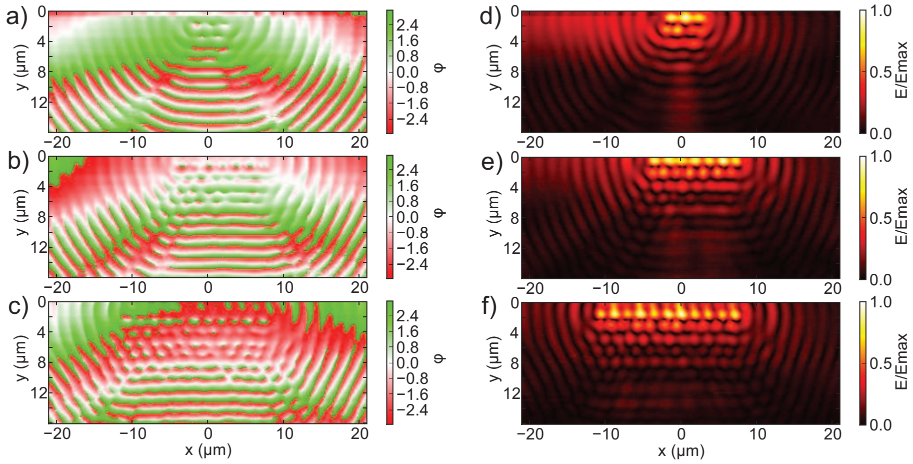

Figure 4.3: Measured phase (a-c) and amplitude (d-f) of the electric field of the surface plasmon polaritons launched by rows of respectively 3 (a, d), 7 (b, e) and 11 (c, f) holes, each with a diameter of 200 nm and a spacing of $1.7\ \mu m$. *All measurements were taken with a vacuum wavelength of* $1.5\ \mu m$ *and with the electric field of the incident light in the y-direction. Each image describes an area of* $42 \times 16\ \mu m$. *In the amplitude data for 3 holes (d), we see the directly transmitted excitation light as a weak, elliptical beam to the left of the structure. The phase images (a-c) clearly show that for 3 holes the SPP field propagates almost circularly outwards from the structure, whereas for 11 holes, the SPP field develops 3 diffraction orders. The amplitude images (d-f) show that parallel to the chain of holes (the row of bright spots at the top of the images), at certain distances away from the chain, the SPP field shows a chain of hotspots with the same period as the chain. These are the so-called Talbot revivals. Note that as the number of holes increases, the Talbot revivals persist at larger distances away from the chain.*

$$z_{\mathrm{T}} = \frac{2\pi}{k_0 - k_\perp} = \frac{2\pi}{k_0 - \sqrt{k_0^2 - k_d^2}}. \tag{4.2}$$

We insert the values for k_0 and k_d and we find

$$z_{\mathrm{T}} = \frac{1}{\frac{1}{\lambda} - \sqrt{\frac{1}{\lambda^2} - \frac{1}{d^2}}}, \tag{4.3}$$

which simplifies to

$$z_{\mathrm{T}} = \frac{\lambda}{1 - \sqrt{1 - (\frac{\lambda}{d})^2}}. \tag{4.4}$$

In the limit of $d \to \infty$, z_{T} goes to $2d^2/\lambda$, which is exactly the Rayleigh result. In the absence of an expression for the relative amplitudes of these diffraction orders, we cannot analytically predict the modulation strength of the Talbot revivals. We have confirmed the behavior of the Talbot revivals for $d < 2\lambda$ by comparing our analytical expression with results from a numerical calculation in which the holes are replaced by non-interacting in-plane dipole sources. The result of such a calculation for the case of 7 holes is shown in figure 4.4.

We see the good correspondence between theory and experiment especially when comparing the numerically calculated (figure 4.4(b)) and experimentally measured (figure 4.3(b)) images of the phase. We see how in both theory and experiments, the wavefronts of the $\pm 1^{\mathrm{st}}$ and the 0^{th} diffraction orders develop at the sides and bottom of the images, respectively. We also note the correspondence in where the dislocations occur between these orders. Lastly, we see that close to the chain of holes at the top of figure 4.3(b) and figure 4.4(b) a complex phase pattern arizes in both theory and experiment. This pattern is due to the Talbot effect. We see a discrepancy when comparing the experimentally acquired phase distribution to the numerically calculated one: the experimental data close to the chain of holes shows a much flatter phase distribution than that obtained from the calculation. This is caused by the fact that a small fraction of the excitation spot is directly transmitted through the thin gold film. As this spot has an almost flat phase front, it flattens out the phase we expect for the SPP pattern.

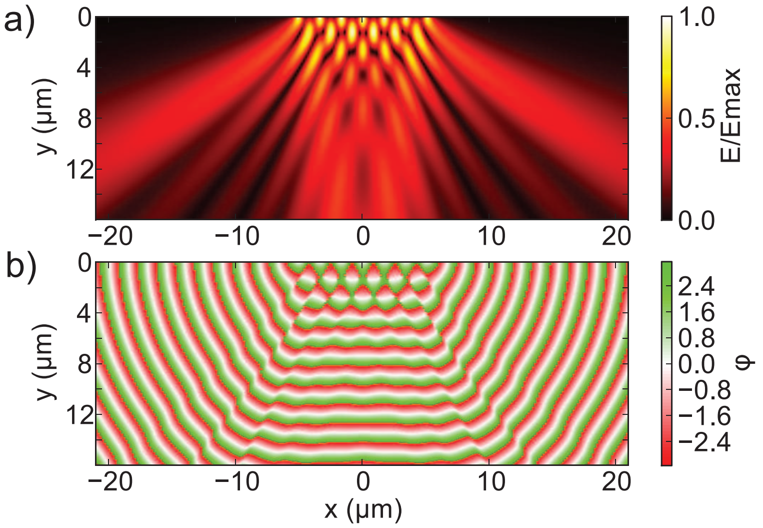

Figure 4.4: Numerically calculated amplitude (a) and phase (b) of the electric field of the surface plasmon polaritons launched by 7 holes, each with a diameter of 200 *nm and a spacing of* 1.7 *µm. This was calculated by adding up the field of 7 non-interacting in-plane dipole sources.*

When comparing the amplitude images for different numbers of holes (figure 4.3(d-f)), we see that as the number of holes increases, the Talbot revivals become more pronounced and persist to distances further away from the structure. To quantify this behavior, we determine the visibility of the Talbot revivals at different distances from the chain for various chain lengths. We define the visibility associated with the amplitude map $|E(x_i, y_j)|$ as $V(y_i) = \sum_i f(x_i, y_j) f(x_i, 0)$, where $f(x_i, y_j) = |E(x_i, y_j)| - \sum_i |E(x_i, y_i)|$. In other words, $V(y_j)$ compares the modulation in row j of the images with the modulation in the row above the holes. We normalize the visibility to the visibility measured above the holes. In the regime where the hole spacing is only slightly larger than the wavelength, the fractional Talbot revivals will be shifted by half a period with respect to the full revivals, which means they will show up as having a negative visibility.

The results of the visibility analysis on both experimental data and numerically calculated SPP fields is presented in figure 4.5. The SPP fields were numerically calculated by replacing the holes by non-interacting in-plane dipole sources. We verified our analytical result, shown as vertical grey lines in figure 4.5, by first performing the analysis on a simulated SPP field corresponding to 51 holes. We have confirmed that within an area of 80 × 20 μm, the calculated pattern does not change significantly when adding more holes to the calculation, which means we can consider this simulated row of 51 holes to correspond to an infinitely large chain. The maxima of the visibility then indeed coincide with multiples of the Talbot length z_{T} (equation 4.4, as indicated by the solid vertical gray lines. For reference, the dashed vertical gray lines correspond to the classical expression of the Talbot length as derived in the paraxial limit by Lord Rayleigh. The black solid lines in figure 4.5(a), (b) and (c) correspond to numerical results for 3, 7, and 11 holes. The points in the graphs are the experimental results. As can be seen in both theory and experiment, the visibility of the revivals decays more rapidly for small numbers of holes. This can be intuitively understood, because the distance within which the diffracted orders still mutually overlap is of the order of the length of the chain. The correspondence between theory and experiment is evident, but it is somewhat spoiled by the fact that besides the Talbot effect there is also interference between the SPP field and light directly transmitted through the gold. Additionally, for the case of 3 holes, all the interesting interferences occur very close to the structure. In this regime, the SPP might not be the only contribution to the signal, but also quasi-cylindrical and/or Zenneck waves might become important [108, 109]. However, for the case of 7 and 11 holes, the revivals extend to a much larger distance away from the structure, so that in this case the SPP is the dominant contribution. Lastly we note that the experimental visibility for three holes stays roughly constant from 7 μm onwards, at a value between 0.1 and 0.2, whereas the visibility for both 7 and 11 holes decays quickly to 0. This is caused by that fact that experimentally, strong beaming of the SPP field occurs (see figure 4.3(d)), which means that there is still a strong transverse modulation of the SPP field even at 20 μm distance away from the structure.

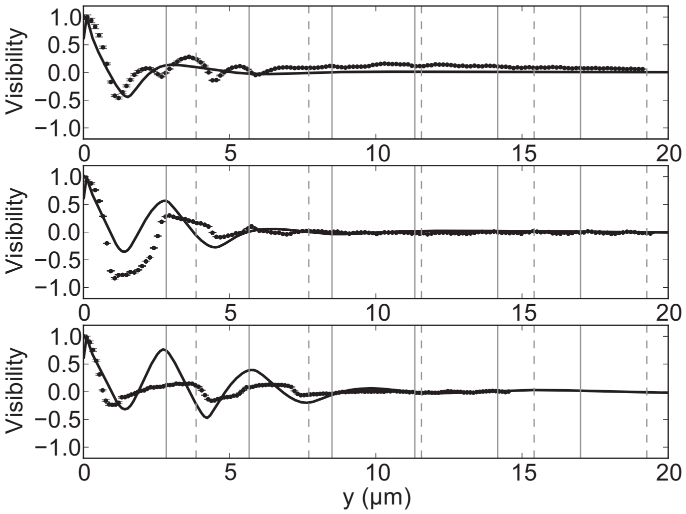

Figure 4.5: The visibility of the Talbot revivals as a function of the distance away from the structure for 3 (a), 7 (b) and 11 (c) holes. As a measure for visibility, we used the inner product of a line trace taken across the holes and all other lines in the SPP field. The experimentally obtained data is represented by the dots. The solid lines are calculated from numerically simulated SPP fields. The solid vertical gray lines indicate where the Talbot revivals would occur for an infinitely long chain of holes. The dashed vertical gray lines are where the Talbot revivals would be according to the Rayleigh result.

4.4 Conclusion

In conclusion, we have used a short chain of holes to launch surface plasmon polaritons on a gold-air interface. We have observed both the integer and the fractional Talbot effect for surface plasmon polaritons on a gold-air interface and investigated how the visibility of the Talbot revivals depends on the number of holes in the chain. We show that when the wavelength of the surface plasmon polaritons is only slightly smaller than the periodicity d of the chain of holes ($\lambda_{\text{SPP}} < d < 2\lambda_{\text{SPP}}$) the revivals do not occur at the Talbot distance as derived by Lord Rayleigh. As we are far outside the paraxial limit, we use an alternative analytical expression for the Talbot distance that correctly predicts the position of the revivals for small spacings, as observed in the experiment and as found in numerical calculations. We have also studied the diffraction of the surface plasmon polaritons and have shown that by changing the input polarization, we can steer the direction of propagation of the surface plasmon polaritons away from the structure. These observations show that the seemingly simple structure of a chain of holes can generate complex SPP patterns of hotspots, that can be manipulated by changing the polarization of the impinging light. We anticipate that this control over two dimensional intensity patterns can have many exciting applications in the field of sensing and integrated optics.

5

Evanescent modes at the interface to slow light

ABSTRACT: Photonic crystal waveguides (PhCWs) support slow light modes which are useful for integrated photonics. The mismatch in group velocities of light in PhCWs and in an access waveguide normally makes efficient coupling to slow light impossible. We experimentally study fields close to an interface between two PhCWs. After the transition from a PhCW in which the group velocity of light is $v_g \sim c/10$ to a PhCW in which $v_g \sim c/100$ we observe a gradual increase in the field intensity and the lateral spreading of the mode. We attribute this evolution to a weakly evanescent mode which exponentially decays away from the interface. We compare this to the situation where the transition between the PhCWs only leads to a minor change in group velocity and show that in that case the evolution is absent. Furthermore, we apply novel numerical mode extraction techniques to confirm experimental results. Evanescent modes at the interface assist in efficient coupling to slow light. The ability to efficiently couple to slow light crosses one of the biggest hurdles for slow-light devices and applications.

5.1 Introduction

Photonic crystal (PhC) waveguides that support slow light modes present new opportunities for enhancing linear and nonlinear optical effects, and realization of compact optical delay lines [7, 25]. Waveguide dispersion and group velocity can be controlled precisely by modifying the PhC geometry to achieve broadband slow light propagation [110], or other dispersive properties tailored for applications such as tunable delays [111] or switching [29]. In order to utilize the benefits of slow light in PhC waveguides, light must be efficiently coupled to them.

Coupling to slow light PhC modes was thought to be difficult [112], one reason being the mismatch in mode profiles between fast light and slow light in PhCs. Recent theoretical work has demonstrated that evanescent modes can play a role in allowing efficient excitation of slow light [113, 114]. Evanescent modes can be excited at interfaces with other waveguides, where they assist in matching the transverse mode profiles on either side of the interface [115]. For example, it was predicted that the presence of a weakly evanescent mode near the inflection point of a PhC waveguide's dispersion curve allows better than 99% coupling efficiency from an incident mode with group velocity $v_g \sim c/5$ to one with $v_g \sim c/1000$ [115]. More generally, evanescent modes play a crucial role in the phenomenon of "frozen light" in which light can be perfectly coupled to zero group velocity modes [116].

In this Chapter, we report experimental evidence for the existence of weakly evanescent modes at an interface to specially engineered slow-light photonic crystal waveguides. We show that at low group velocities in these waveguides, the field intensity grows and the lateral extent of the electric field increases gradually into the slow light waveguide, while at higher group velocities this behavior is absent. Both the gradual rise in intensity and the evolution of the field profile are signatures of a weakly evanescent mode. A novel numerical mode extraction technique [117] confirms these conclusions and reveals an evanescent mode which decays over a length of ~ 10 PhC periods.

5.2 Sample and far-field measurements

The geometry under study is similar to that considered in [115]. The PhC consisted of three waveguide sections: an 80 μm long central waveguide supporting a mode with a dispersion inflection point, at which $v_g < c/100$, connected at both ends to 10 periods of modified waveguide. For the frequencies used in this investigation, the end waveguides supported a relatively fast mode, with group velocity $v_g \approx c/5$. The outer PhC sections were connected to tapered ridge access waveguides. The samples were fabricated on a silicon-on-insulator wafer consisting of a 220 nm Si layer on a 2 μm layer of silica using electron-beam lithography and reactive ion etching. The PhCs were under-etched using hydrofluoric acid to form symmetric Si membranes in air. Further details of the fabrication process can be found in [110]. The geometry is illustrated in Figure 5.1a. Only one end of the structure is shown, the other being the mirror image. The PhC waveguides were formed in a triangular lattice of holes with period $d = 420$nm, and hole radius $r = 128$nm $= 0.305d$. To create an inflection point in the dispersion curve of the central section, we locally modified the geometry by shifting the first two rows of holes on either side of the waveguide in the direction parallel to the waveguide. The first row of holes was displaced by $p_1 = 0.3d$, and the second row by $p_2 = 0.4d$ in the same direction, as illustrated in Figure 5.1a. The PhC sections at either end were similar to the central section but the lattice was “stretched” by 30 nm per unit cell along the waveguide so that the wavelength of the inflection point in the central section coincided with a fast mode in the end sections. A similar approach was used in [113] to demonstrate efficient coupling between fast and slow PhC modes.

The waveguide was first characterised by obtaining transmission and group velocity spectra, using a broadband TE-polarized light source and optical spectrum analyzer. The group velocity was measured using Fourier transform interferometry by combining the transmitted light with light from a reference arm and analysing the resulting interference spectrum [118]. The measured transmission and group index are shown in Figures 5.1e and d, respectively. Note that although there is a sharp drop in transmission corresponding to the slow light region, we attribute this largely to increased propagation loss, rather than to inefficient coupling into the slow light mode. The dispersion curves for the two waveguide sections, obtained by fitting 3D band structure calculations to the measurement results, are

---

The sample was fabricated in St.Andrews. The author acknowledges Thomas White and Thomas F. Krauss.

Measurement thanks to Thomas White.

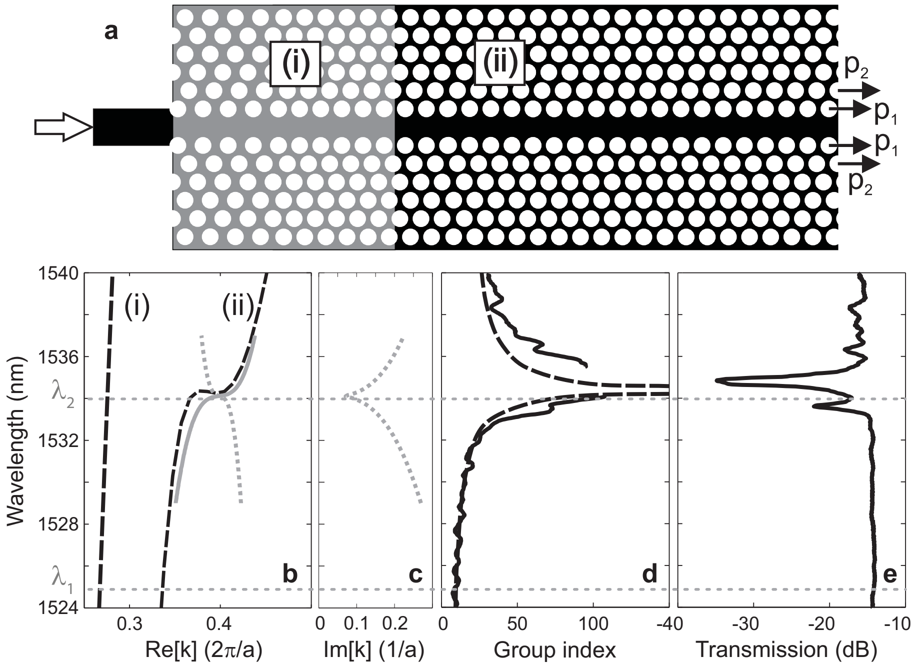

Figure 5.1: (a) Geometry of the waveguide. The W1 waveguide is formed by leaving out a row of holes. The first and second rows of holes were shifted by $p_1 = 0.3d$ and $p_2 = 0.4d$, respectively, in the direction parallel to the waveguide, to create an inflection point in the dispersion curve. In region (i) the lattice was stretched by 30 nm. (b) Calculated dispersion for the two waveguide sections (dashed black lines) and dispersion retrieved from the numerical fit (gray lines). (c) Imaginary component of the wavevector of the evanescent mode, from the numerical fit. (d) Calculated (dashed line) and measured (solid line) group index spectrum. (e) Measured transmission spectrum. The dotted horizontal gray lines indicate the two wavelengths studied with near-field measurements. At λ_1, light is fast in both PhCW sections. At λ_2, light is slow in section (ii). The imaginary component of the wavevector of the evanescent mode decreases sharply close to λ_2, which results in gradual coupling to slow light.

shown as black dashed lines in Figure 5.1b. The dashed black line in Figure 5.1d is the group index obtained by the same calculation. At a free-space wavelength of λ=1533.95 nm, indicated by a horizontal dashed gray line, the dispersion of section (ii) of the waveguide displays an inflection point, with a correspondingly high group index $n_g \sim 100$. At the same wavelength, the dispersion curve in section (i) is steep, resulting in a relatively low group index $n_g \sim 5$. On the other hand, at λ=1525 nm, indicated by the other horizontal gray line in Figure 5.1, $n_g \sim 5$ in the outer sections and $n_g \sim 10$ in the central section. We study the interface between section (i) and section (ii) at these two wavelengths.

5.3 Near-field measurements

We perform phase- and polarization-sensitive near-field optical measurements [54] on the waveguide. Figure 5.2 depicts $|E_x|$, the modulus of the transverse component of the electric field, i.e. the component which oscillates perpendicular to the waveguide, as a function of position (in units of d), for the two wavelengths. Light propagates from left to right. The dotted line at $y = 0$ indicates the interface between sections (i) and (ii). The measurement of figure 5.2a was taken at λ_1=1525 nm. At this wavelength, the group velocity in the central waveguide is $v_g \sim c/10$. The measurement of figure 5.2b was taken at λ_2=1533.95 nm. At this wavelength, the group velocity in the central waveguide is $v_g \sim c/100$. The amplitude was normalized in both images such that the maximum amplitude in the first waveguide is equal to 1.

We clearly observe different behavior of the electric field in the two cases. It can be seen that close to the inflection point, the electric field amplitude grows into the slow light section by a factor of ~ 5, as expected [115]. Far from the inflection point, the amplitude grows by less than 10%. Another difference is that far from the inflection point, the electric field does not expand laterally after entering the central waveguide. To the contrary and most strikingly, close to the dispersion inflection point, the field laterally expands further into the PhC lattice, but the expansion is gradual.

The integrated intensity $\int |E_x^2| dx$ is plotted in Figure 5.3a as a function of position along the waveguide, y. This value is proportional to the energy density in the waveguide. The solid vertical line indicates the interface between the two PhC sections. In the first 15 periods beyond the interface,

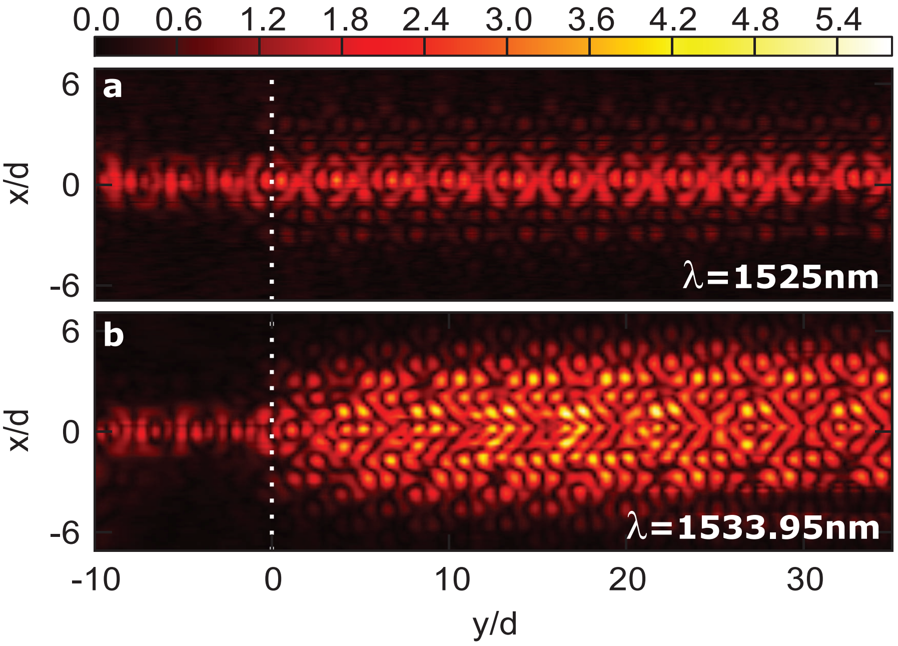

Figure 5.2: Near-field measurements of the electric field above the waveguide. The waveguide is centered at x=0. Light propagates from left to right. The dashed white line indicates the interface between the two waveguide sections. (a) The light is "fast" in both waveguide sections, at a wavelength of λ_1=1525 nm. (b) The light is slow in the second section, at λ_2=1533.95 nm. Upon transition from a fast to a slow section, the intensity rises and the mode gradually spreads in the lateral dimension.

energy density at λ_2 grows to a value ~ 10 times higher than the energy density at λ_1. This is consistent with the measured slowdown factor of 10. The rise in intensity was pointed out in [115], based on numerics. The modes interfere destructively at the interface, and since one is evanescent, further into the waveguide only the propagating mode is left, which results in a field strength which is higher further down the waveguide than at the interface. As the light propagates even further, the measured intensity starts to decay, due to propagation losses [35, 119].

To quantitatively study the broadening of the mode profile in the case of coupling to slow light, we determine the variance of the intensity along the length of our structure. The variance is defined as:

$$\sigma^2 = \frac{\int (x-\mu)^2 I(x)dx}{\int I(x)dx}. \tag{5.1}$$

Here $I(x)$ is the measured intensity, and μ is the center of mass on the x axis. The variance shows directly how much the intensity spreads into the surrounding PhC lattice. The results of the calculation are depicted in Figure 5.3b for the two wavelengths of Figure 5.2. To avoid effects due to the Bloch nature of light in photonic crystals, the variance is averaged over each unit cell.

At λ_1=1525 nm, the variance does not change noticeably over the length of the waveguide. At λ_2=1533.95 nm, however, the mode expands progressively as it propagates further into the second waveguide, with the variance growing by a factor of ~ 2. Both the gradual expansion of the mode and the rise in intensity are signatures of a weakly evanescent mode which is excited at the interface between the fast and slow sections of the waveguide.

5.4 Dispersion measurements and modal extraction

To retrieve the dispersion of the evanescent mode, we perform a series of near-field measurements at different input wavelengths. At each wavelength, we take a fast Fourier transform (FFT) to visualize the spatial frequency spectrum. Propagating modes of the structure appear as peaks in the Fourier spectrum. Figure 5.4 depicts a section of the dispersion diagram obtained in this way. Dashed gray lines indicate the two wavelengths studied in previous sections. Two modes are obvious in the image. The

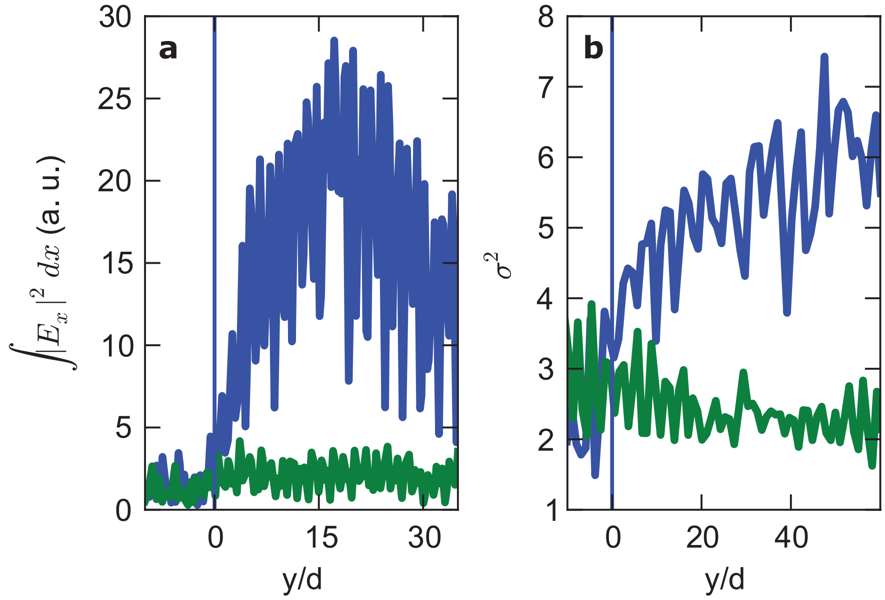

Figure 5.3: Intensity and field spread. (a) $\int |E_x|^2 dx$ *along the length of the waveguide. The green curve is measured at* λ_1*=1525 nm; the blue curve is measured at* λ_2*=1533.95 nm. (b) Variance of the intensity along the waveguide. The solid vertical lines indicate the position of the interface between the two waveguide sections.*

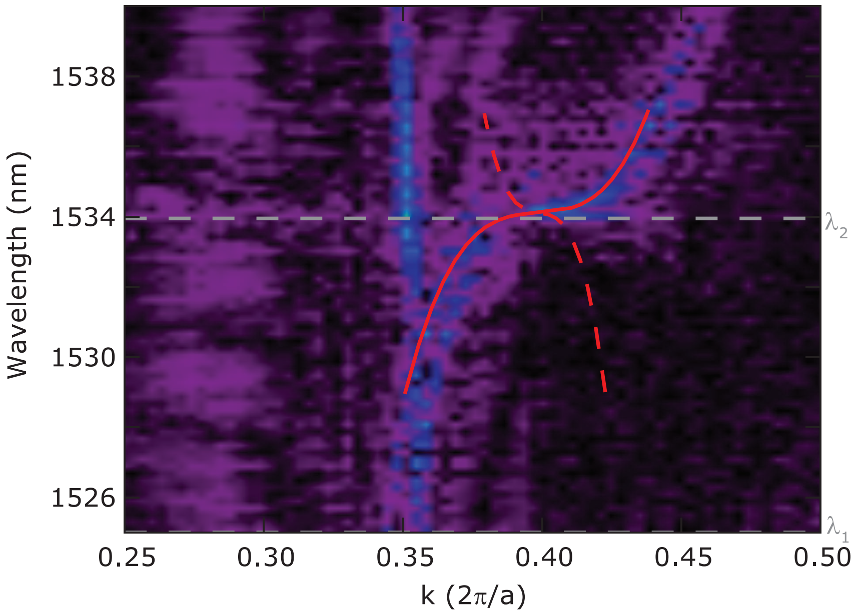

Figure 5.4: Dispersion measurement. The dispersion is obtained by measuring the near field along the entire waveguide length. The field is Fourier-transformed. Waveguide modes appear as peaks in the Fourier spectrum. The procedure is repeated for each wavelength, with a wavelength step $\Delta\lambda = 0.2$ *nm. The mode which displays little dispersion is the light line in the silicon slab. The other mode contains an inflection point. Dashed gray lines indicate the two wavelengths considered in previous sections. The thin red lines are results of the numerical dispersion extraction. The continuous line indicates the result for the propagating mode. The dashed line indicates the result for the evanescent mode.*

straight line, which seemingly exhibits little dispersion, corresponds to the light line in the silicon slab. The other mode displays an inflection point close to λ_2. The section displayed was chosen in order to make a comparison with the calculation of figure 5.1b. In addition to the mode of the central waveguide, which contains an inflection point, figure 5.1b includes a mode of the fast section, with $0.25 < k < 0.3$. Only a vague trace of this mode can be seen in the measurement, because the amplitude of the peaks of the FFT is directly proportional to the spatial extent of the mode. Additionally, the width of an FFT peak is inversely proportional to the spatial extent. With the fast section only 10 periods long, the mode of that section manifests as a small, wide peak in the Fourier spectrum. Similarly, the evanescent mode, which is expected to appear close to the inflection point, does not show up in the dispersion measurement.

To extract the weak evanescent mode from the data, we apply a numerical dispersion extraction technique [117]. The technique involves performing fits to find the optimal combination of propagating and evanescent Bloch modes that best matches the experimental data. The obtained dispersion of the propagating mode in section (ii) is shown as the solid gray line in Figure 5.1b. The dispersion of the evanescent mode is shown as the gray dotted line. As pointed out in [115], at the inflection point the evanescent and propagating modes are phase-matched. The imaginary component of the wavevector, shown in Figure 5.1c, contains a dip centered at the inflection point. At this wavelength, the evanescent mode decays only weakly, with a decay length of ~ 10 periods, and assists in the coupling to slow light [115]. This is consistent with the measured gradual spread of the mode and rise in intensity. The results of the numerical dispersion extraction are also depicted as red lines in figure 5.4. The continuous line is the result obtained for the propagating Bloch mode, showing good agreement with the measurements. The dashed line is the extracted dispersion of the evanescent mode.

5.5 Conclusion

In conclusion, we have used a combination of direct near-field measurements and dispersion extraction techniques to observe experimentally the excitation of a weakly evanescent mode at the interface between two pho-

---

The author thanks Sangwoo Ha and Andrey Sukhorukov for the numerical extraction.

tonic crystal waveguides supporting propagating modes with very different group velocities. Such evanescent modes have been shown theoretically to enable very efficient coupling between fast and slow light, and also play a crucial role in the phenomenon of frozen light. We show that the electric field spreads laterally and grows in intensity gradually as it propagates in the slow section of the crystal. Both the lateral spread and the growth in intensity are signs of an evanescent mode. Efficient coupling to slow light in photonic crystals is important for applications in optical buffers, switches, filters and sensors.

6

Measuring localization length with a near-field probe

ABSTRACT: Waves in disordered media can undergo multiple scattering. For sufficiently high disorder, multiple scattering results in Anderson localized states. The spatial extent of localized states, or localization length (L_{loc}), is one of the primary parameters in studies of localization. In the optical regime, measurements of L_{loc} to date have relied on statistical averaging over many realizations of disorder. In this chapter we show a method for measuring L_{loc} of individual localized photonic states. By introducing a metallodielectric probe into the near field of a photonic crystal waveguide, L_{loc} can be deduced from the spectral shift of localized states, which occurs due to the interaction of the magnetic field of light with the probe. Our method opens a new pathway to explore localization in photonics, with implications spanning all wave physics.

6.1 Introduction

In this chapter, we use the diamagnetic interaction of a metalized near-field probe with the magnetic field of light [120] to investigate localized states in a photonic crystal waveguide. Our PhCW is formed by a single row of missing holes from a hexagonal lattice of air holes in a Si membrane, as depicted in figure 6.1a. The calculated band diagram of the waveguide is depicted in figure 6.1b. The calculation was performed using the MIT Photonic-Bands package (MPB). The diagram describes the relation between frequency and wavevector of light in the waveguide. To correlate the diagram with real-world parameters used in the lab, the frequency is given in terms of the free-space wavelength. Lines in the diagram correspond to dispersion curves of waveguide modes. The group velocity of light is given by the slope of the curves, $v_g = \partial\omega/\partial k$. At wavelengths close to 1567.5 nm, the slope of the dispersion curve of the only waveguide mode becomes shallow, resulting in a decrease of group velocity. In theory, at $ka/2\pi = 0.5$, the group velocity goes to zero.

In practice, it has been shown that disorder affects the group velocity achievable in real devices [32, 34, 36, 35]. The idea that disorder in photonic crystals [121] can be used as a model system for the study of localization is as old as the research field of photonic crystals [22]. Even with state-of-the-art fabrication, some residual disorder will always remain in the crystal, and localization will occur in a 1D photonic crystal waveguide [35]. The average localization length, L_{loc}, scales inversely with the density of states [122, 37], and hence inversely with the square of the nominal group refractive index, n_g [36, 123, 38]. Close to the band edge, the group index rises, and when the average L_{loc} becomes shorter than the waveguide length Anderson localization sets in. For device lengths typically used in practice (on the order of 100 μm), the transition to Anderson localization occurs at group indices $n_g \approx 35 - 65$ [35]. The localized states of light closely resemble PhC microcavities in their behaviour. PhC microcavities are deliberately engineered defects which confine light to small volumes, with high quality factors and precisely defined resonance frequencies [124]. In the Anderson localization regime, similar "cavities" are formed at random positions in the waveguide, with random quality factors and resonance frequencies. The volume which such a localized state occupies is proportional to L_{loc}. Thus

---

The author thanks Daryl Beggs for the calculation.

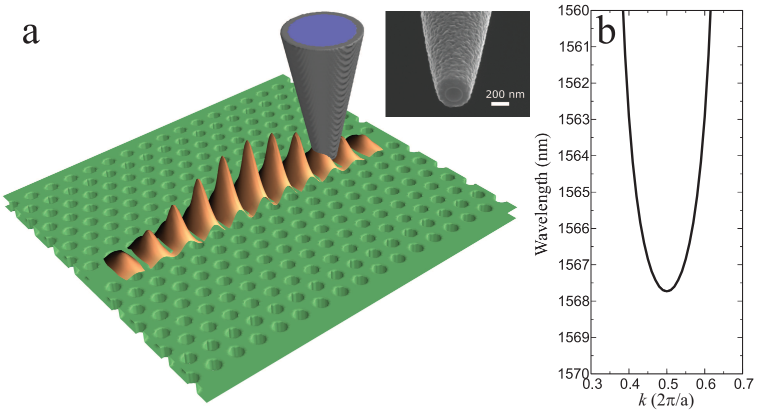

Figure 6.1: **Schematic representation of the sample and near-field probe.** **a** *An aluminum-coated near-field probe (inset) is scanned over the surface and collects a fraction of the light. The magnetic field of light interacts with the aluminum coating to shift the resonance of localized states.* **b** *Calculated dispersion of the waveguide.*

far, Anderson localization in PhC waveguides has been observed as narrow transmission resonances due to the randomly embedded "cavities" [40, 125, 126, 35, 127] and an increase in out-of-plane scattering [37, 35]. Since the spectral position of the resonances and the strength of scattering are random, these methods rely on statistical averaging over many instances of disorder to extract the average L_{loc}. A method to measure L_{loc} for each individual localization instance could provide more insight into the behaviour of the individual localized states.

The magnetic field of light usually plays a negligible role in light-matter interactions [128]. Recently, however, it has been shown that the magnetic field above a PhC microcavity can interact with a metalized near-field probe [120, 129]. Our near-field probe is a tapered glass fibre of diameter $\sim 200\,\text{nm}$, coated with aluminum of thickness $\sim 150\,\text{nm}$ (figure 6.1a, inset). Above a PhC cavity the magnetic field of light drives a current through the metal coating, and, in a nanoscopic manifestation of Lenz's law, the magnetic field caused by the current opposes that of the cavity. The result is that the resonance frequency of the cavity is shifted to the blue. Thus inserting the near-field probe into the evanescent near field of an Anderson localized state should shift its frequency, and the frequency shift can be measured as a function of position of the probe. From the location-dependent magnitude of the spectral shift, we will determine the localization volume and length. Hence we determine L_{loc} directly on each instance of localization, without a need for statistical averaging. This opens up the possibility for case-to-case studies of localization in individual waveguides, with anticipated implications for other kinds of wave phenomena. L_{loc} has been measured directly in the microwave regime [130], however measurements in the optical regime were absent, due to a lack of a reliable method.

6.2 Transmission and near-field measurements

To find the spectral position of localized states, we measure a transmission spectrum of the waveguide (Fig. 6.2a). Linearly polarized light from a continuous-wave laser is coupled into the access ridge waveguide, using a 40x (NA = 0.55) objective. The polarization axis is parallel to the plane of the PhC slab, to excite the TE-like modes in the photonic crystal waveguide. Transmission is monitored with a lensed fiber at the output facet. The fiber is connected to a Thorlabs photodetector. The wavelength is scanned in steps of 0.01 nm, in the range 1560 nm to 1565 nm. A distinct drop in transmission can be observed at $\sim$ 1561.5 nm, indicated with a dashed black line in the transmission spectrum. At longer wavelengths, narrow and sparse resonances appear, a sign of localization [40, 130]. Next, we bring the near-field probe close to the sample and measure the electric field above the waveguide. The amplitude of the electric field, as a function of laser wavelength and probe position, is depicted in figure 6.2b. At shorter wavelengths (top of the image), we operate far above the band edge. In this spectral region light propagates in the Bloch modes owing to the structure's periodicity, and the measured electric field reflects this. The beating between different Bloch modes results in periodic modulations of the amplitude with two different beating frequencies. Beating between different harmonics of the same Bloch mode causes amplitude modulation with a period equal to the lattice constant of the crystal. Beating between backward- and forward- propagating Bloch modes causes amplitude modulation with a period of several lattice constants. The period of this second beating depends on the wavelength, because the difference in wavevectors of the forward and backward components becomes smaller towards longer wavelengths. Observing the exit of the PhCW (at the position $x = 82\ \mu$m), for short wavelengths we find that transmission is high, i.e. the measured electric field at $x = 82\,\mu$m is comparable to that at $x = 0$. At $\lambda \approx 1562$ nm), we start to observe the first localization peaks, visible as an increase in intensity of the electric field. These first features seemingly extend over the length of the waveguide. Observing the optical signal at the exit of the PhCW, we note that the onset of localization causes the electric field at this point to exhibit sporadic amplitude dips, which is consistent with the amplitude dips observed in transmission measurements of figure 6.2a. Similar behavior of the electric field is observed at longer wavelengths, up to $\lambda \approx 1563.5$ nm. Another example of an extended localization instance is visible at $\lambda = 1563.35$ nm. For even longer wavelengths, the amplitude of the electric field at the end of the waveguide becomes negligible, apart from sparse peaks. In general, at wavelengths longer than $\lambda = 1563.5$ nm, the electric field extends a shorter distance into the waveguide. It is noteworthy that the structure of the electric field, owing to beating between different Bloch modes, persists throughout the localization regime. This structure is an indication that even in the localization regime, the light populates modes of the nominal, perfect structure.

To relate the free-space wavelength to the group index, we use the band structure of our sample. The band structure is obtained by a fast-Fourier-transform of our data [131], depicted in figure 6.2c. The dispersion curve of the PhC waveguide follows the behavior expected from calculation (figure 6.1b). Away from the band edge (top of the image), the dispersion curve can be approximated by a parabola. A parabolic fit to this part of the curve results in the dashed yellow line. We obtain the group index of the nominal structure, without any disorder, by taking the first-order derivative of the fit. The nominal group index is shown on the right-hand axis. Theory and measurements involving statistical averaging [35] have shown that for our waveguide the average length of localization instances becomes of the order of the waveguide length at $n_g \approx 65$. This group index corresponds very well with our first spatially resolved observation of localization, at $\lambda = 1562$ nm. In the band structure, localized states appear as horizontal lines. The broad distribution of wavevectors results from the high spatial confinement.

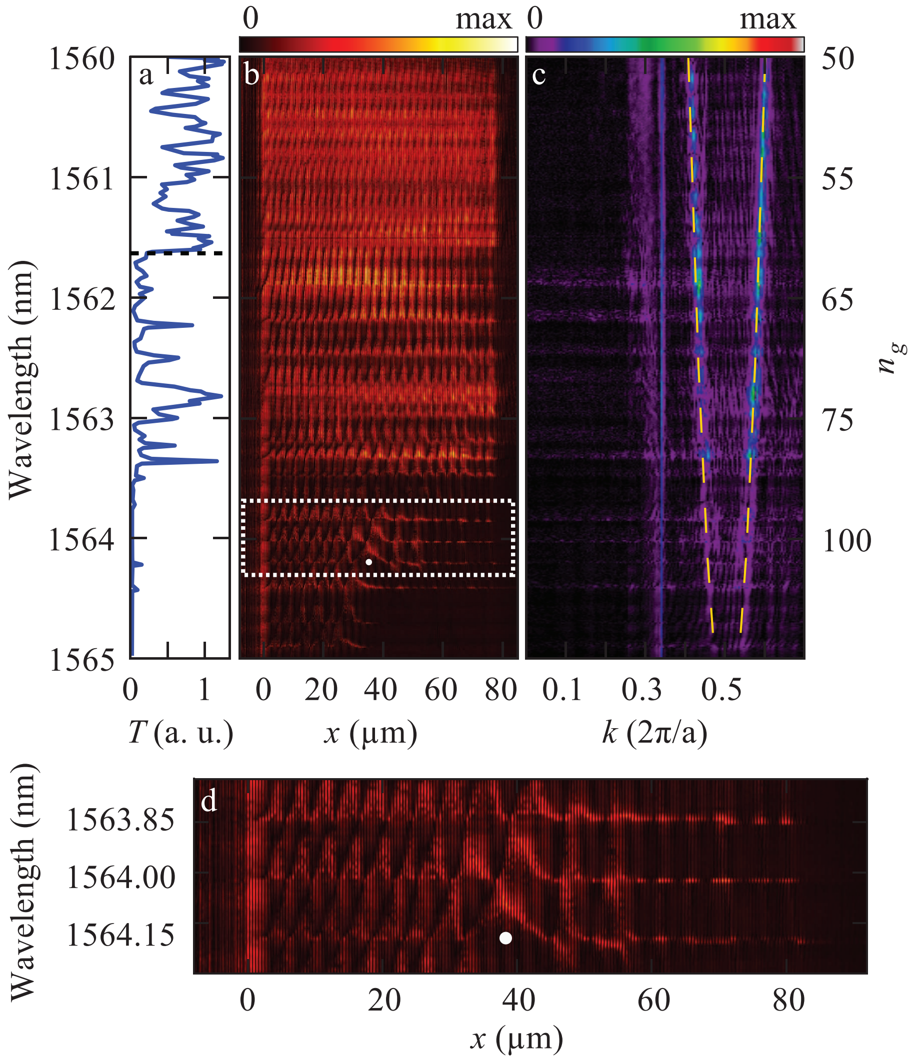

Figure 6.2: **Waveguide transmission, near-field amplitude, and dispersion.** **a**, *Transmission spectrum, T, of the PhCW.* **b**, *Near-field amplitude collected through the probe, as a function of wavelength and probe position along the center of the waveguide. Light enters the PhCW from the left, at position $x = 0$.* **c**, *Band structure of the waveguide. A parabolic fit is depicted by the dashed yellow line. The nominal group index, n_g, is obtained by taking the derivative of this line.* **d**, *Closeup of the near-field of the region indicated with a dashed white box in part b).*

6.3 Near-field measurements of localized states

The near-field probe collects the electric field with high resolution, but at the same time its interaction with the magnetic field shifts the spectral position of the localized resonances to the blue. This magnetic-induced shifting is most evident for long wavelengths, at the bottom part of figure 6.2b. For certain spatial positions of the probe, the maximum of the electric field is shifted from its original spectral position towards shorter wavelengths. One such position is indicated by a white dot in the image. The shift occurs periodically with spatial position, as a result of interference between forward- and backward-propagating Bloch modes. We primarily observe the shift in the left half of the waveguide, which leads us to believe that the amplitude of the localized states is small in the right half of the waveguide.

6.4 Influence of the probe on transmission

In the previous section, we described the observation of spectral shifts of localized states in the near-field signal. In this section, we show that we also observe spectral shifts if we monitor waveguide transmission as the probe is scanned along the sample. Figure 6.3 displays the transmission as a function of probe position and laser wavelength, normalized to the maximum transmission. Light is incident from the left and propagates to the right.

At positions of the probe between $0\,\mu$m and $\sim 82\,\mu$m, the probe is above the PhCW. At positions $x < 0$, the probe is above the access waveguide. At positions $x > 82\,\mu$m, the probe is above the exit waveguide. The transmission for probe positions on the exit waveguide gives the transmission spectrum without any probe influence. A transmission peak can be observed at 1563.35 nm. Interestingly, when the probe is above certain positions on the waveguide, this peak is shifted to shorter wavelengths. The shift can be seen when we follow the high-intensity peak at 1563.35 nm as the probe is scanned along the waveguide. As the probe moves in a line, we observe maxima and minima in transmission. At positions between two maxima, the transmission is shifted towards shorter wavelengths. A similar shift is observed for a smaller peak at 1563.50 nm. To illustrate, we consider the wavelength of 1563.32 nm, which lies just to the blue of the peak at 1563.35 nm. Figure 6.4 displays the measured transmission at that

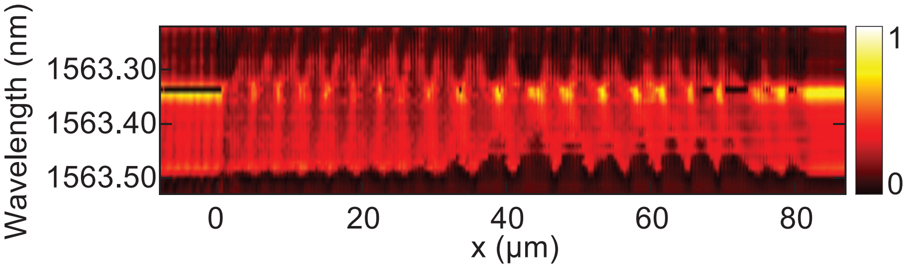

Figure 6.3: Transmission, given by the color scale, as function of probe position (horizontal axis) and wavelength (vertical axis). The transmission is normalized to its maximum value in this image. Light propagates from left to right. The access waveguide ends and PhCW begins at 0 µm. The exit waveguide begins at $\sim 80\,\mu m$*. Transmission is clearly influenced by probe position. A noticeable transmission peak lies at 1563.35 nm. This peak is shifted to shorter wavelengths for certain probe positions.*

wavelength as the probe is scanned along the waveguide. The grey shaded areas indicate the entrance and exit access waveguides. The grey region on the left side of the image, when the probe is above the access waveguide, is obscured by Fabry-Perot fringes. To explain the exact origin of these fringes, further investigation is needed. A preliminary study shows that the contrast of the fringes decreases at lower n_g, with especially large values of the contrast at spectral positions where a localized state is observed. A possible cause of the fringes is interference between the incident light and light scattered back from the localized states[35]. Another possible explanation is that, because at this wavelength the localized state is longer than the waveguide, the probe disturbs transmission even when it is positioned above the access waveguide. The grey region on the right side of the image indicates positions at which the probe is above the exit waveguide. Comparing the transmission in the presence of the probe above the PhC waveguide to the transmission when the probe is above the exit waveguide, it is obvious that at this wavelength the probe enhances transmission up to a factor of 2.5.

From the above discussion, it is clear that the presence of the probe changes the transmission spectrum. When the probe is above the entrance or exit waveguide, the transmission spectrum is unperturbed. When the probe is above the PhC waveguide, the spectrum may be influenced by the

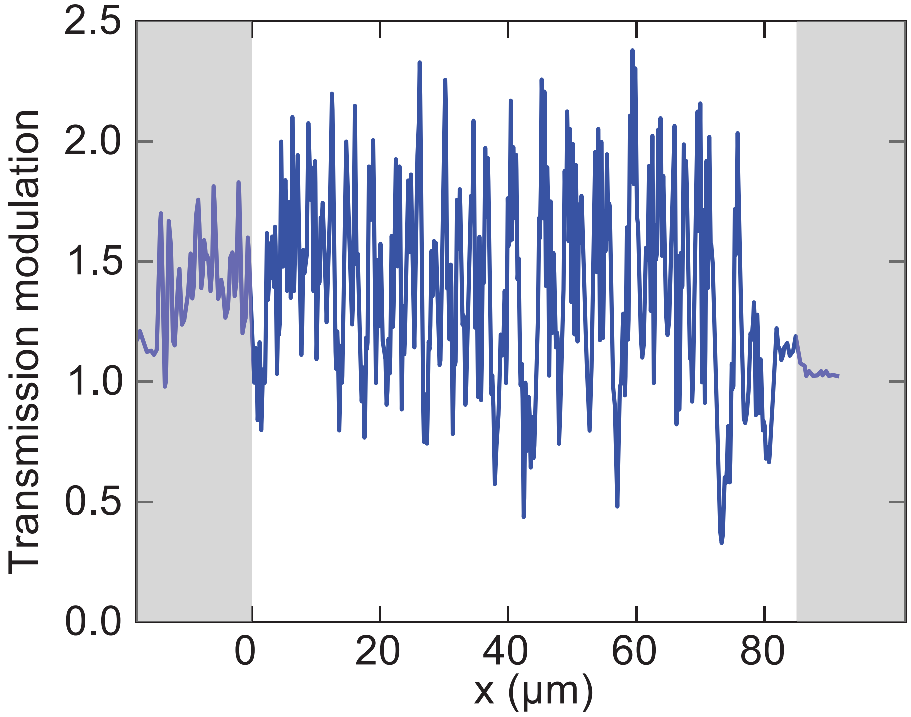

Figure 6.4: Transmission modulation at $\lambda = 1563.32\,\mathrm{nm}$ *due to the presence of the probe, as a function of its position. For certain positions of the probe above the PhCW, the transmission is enhanced by a factor of 2.5 compared to transmission when the probe is above the exit waveguide (shaded region to the right). When the probe is above the entrance waveguide (shaded region to the left), Fabry-Perot fringes due to reflection at the input facet of the PhCW influence the measurement.*

probe. We can directly study the effect of the probe by comparing the unperturbed to the perturbed transmission spectra. Figure 6.5 illustrates the two cases. The green curve is T_U, the unperturbed transmission spectrum. This curve is obtained by taking the transmission spectrum from figure 6.3 for $x = 84\,\mu$m. At this position the tip is above the exit waveguide and does not perturb the PhCW mode. The red vertical dashed line indicates the central position of the unperturbed transmission peak. The blue curve is T_P/T_U, where T_P is the perturbed transmission spectrum. T_P is obtained by taking the transmission spectrum from figure 6.3 at a position $x \approx 42$ μm, where the probe-induced shift is most evident. In agreement with results of figure 6.4, the transmission is enhanced by a factor 2.5 on the blue side of the original transmission peak. At the same spectral positions, transmission at the wavelength of the original peak drops by 50%. Towards longer wavelengths, at $\lambda = 1563.45\,$nm, the unperturbed and perturbed transmission are equal, which results in the blue curve levelling off at 1. These observations are a clear sign of a probe-induced blue shift of the localized state.

6.5 Measuring localization length

To study the shift as a function of wavelength in a quantitative manner, we first sample the shift of each resonance at different probe positions. To do this, we analyze the near-field data (figure 6.2b) for the spectral position of the maximum electric field at a narrow wavelength range around a particular resonance. We record the spectral position of this maximum for all positions along the waveguide and collect them in a histogram. One such histogram is displayed in figure 6.6. Two broad peaks can be identified in this image. The peak centered at $\lambda = 1564.89\,$nm is the original unperturbed peak, which we identify from near-field amplitude measurements. The peak at $\lambda = 1564.74\,$nm is the blue-shifted peak. This particular resonance shifts by $\Delta\lambda = -0.15\,$nm.

The spectral shift, $\Delta\lambda$, was shown to be inversely proportional to the volume of a designed PhC microcavity, in work performed with a dielectric uncoated probe [132]. In the case of an uncoated probe, the resonance shifts to the red, with a relative shift:

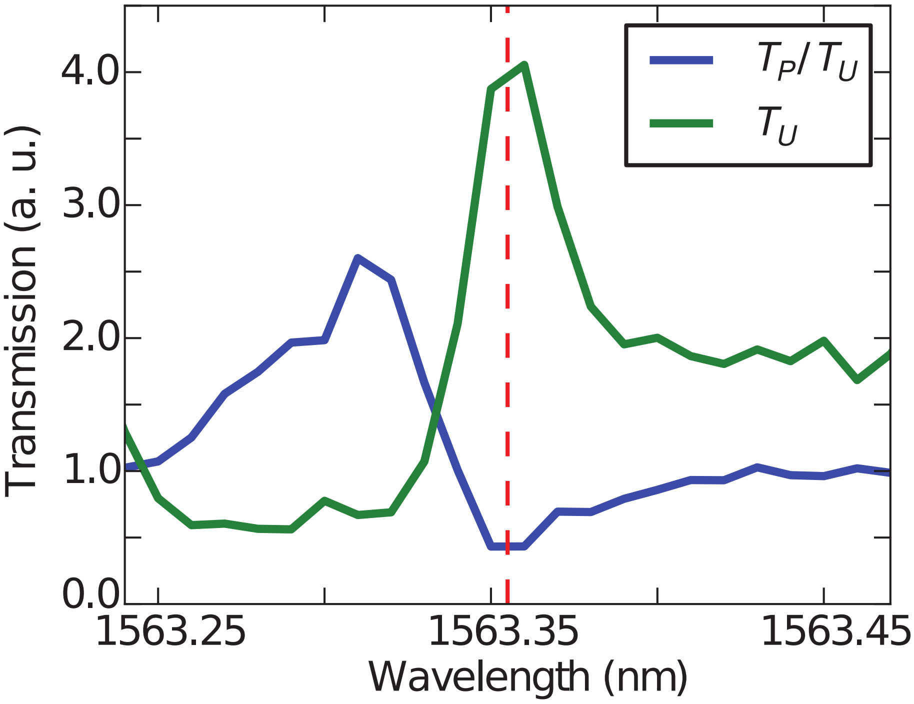

Figure 6.5: Probe-induced blue-shift of a transmission resonance. The green curve is the unperturbed transmission spectrum, T_U*. The center of the unperturbed peak is indicated with a red verical dashed line. The blue curve is the ratio of the unperturbed to the perturbed transmission spectrum,* T_U/T_P*. The blue shift is evident from the transmission enhancement on the short-wavelength side of the original peak, the drop in transmission at the position of the dashed red line, and the unchanged transmission on the long-wavelength side of the original peak.*

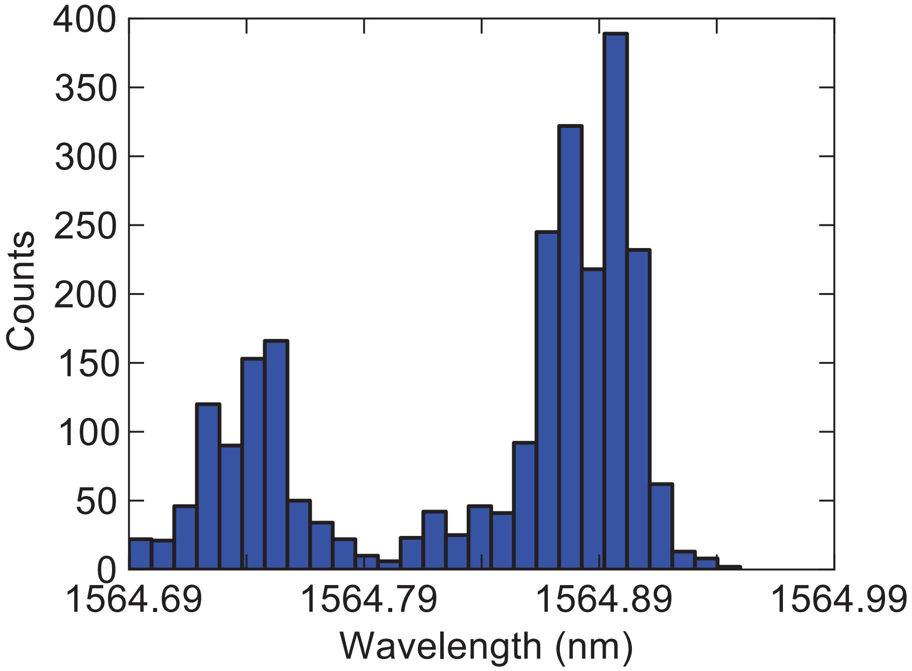

Figure 6.6: A histogram of spectral positions of the near-field maxima for one resonance. The spectral position of the maximum is collected for each spatial position along the waveguide. The positions are binned in a histogram, with the number of bins given by the resolution of the wavelength step and the total wavelength range considered. The total number of counts is equal to the spatial resolution multiplied by the length of the waveguide. Two distinct peaks are present, corresponding to the unperturbed and the perturbed resonance.

$$\frac{\Delta\lambda(r_{\text{pr}})}{\lambda} = -\frac{\alpha^{e}_{\text{eff}}}{2V_{\text{cav}}}\frac{|E(r_{\text{pr}})|^2}{\max[\epsilon(r)|E|^2]}, \tag{6.1}$$

where α^{e}_{eff} is the effective polarizability of the probe; V_{cav} is the cavity volume (area*length); $\epsilon(r)$ is the electric permittivity at the position of the probe; $\max|E|$ is the maximum magnitude of the electric field in the sample; and $|E(r_{\text{pr}})|$ is the magnitude of the electric field at the position of the probe. For a metal-coated probe, such as the one used in this work, Burresi *et al.* [120] showed that the magnetic polarizability, rather than the electric polarizability, has a dominant effect on the shift of the resonance. With this in mind, we use a modified version of equation (6.1):

$$\frac{\Delta\lambda(r_{\text{pr}})}{\lambda} = -\frac{\alpha^{m}_{\text{eff}}}{2V_{\text{cav}}}\frac{|H_z(r_{\text{pr}})|^2}{\max[\mu_0|H_z|^2]}, \tag{6.2}$$

where H_z is the component of the magnetic field which points into the probe; μ_0 is the magnetic constant; and α^{m}_{eff} is the magnetic polarizability of the probe. We are now in a position to estimate L_{loc} as

$$L_{loc} = -\frac{\lambda}{\Delta\lambda}\frac{\alpha^{m}_{eff}}{2A_{cav}}\frac{|H_z|^2}{max|H_z|^2}, \tag{6.3}$$

where we write $V_{cav} = L_{loc}A_{cav}$ and approximate A_{cav} to be the same as that of the waveguide mode. The approximation is valid, because, as we have pointed out in the discussion of figure 6.2, even in the localization regime light populates the waveguide mode. The magnetic polarizability of our probes was estimated by Burresi *et al.* [120], and has a value of $\alpha^{m}_{\text{eff}} = -7 \text{ X } 10^{-21}\text{m}^3/\mu_0$. To estimate the other parameters in equation (6.3), we calculated the eigenmodes of the unperturbed photonic crystal waveguide by using MPB. The eigenmodes at the wavelengths of our study have an effective area of $1.12a^2$, with a the period of the PhC lattice. The ratio $\frac{|H_z(r)|^2}{\max|H_z(r)|^2}$ at the height of the probe is found to be 0.22. Inserting the above estimated values and the measured wavelength shift into equation (6.3) results in figure 6.7.

Figure 6.7 depicts the determined length of individual localized states in our waveguide, normalized to the unit cell of the PhC, as a function of wavelength and group index. The largest source of error stems from the determination of α^m. In the work by Burresi *et al.* [120], the difference between the experimental result and the theoretically predicted value

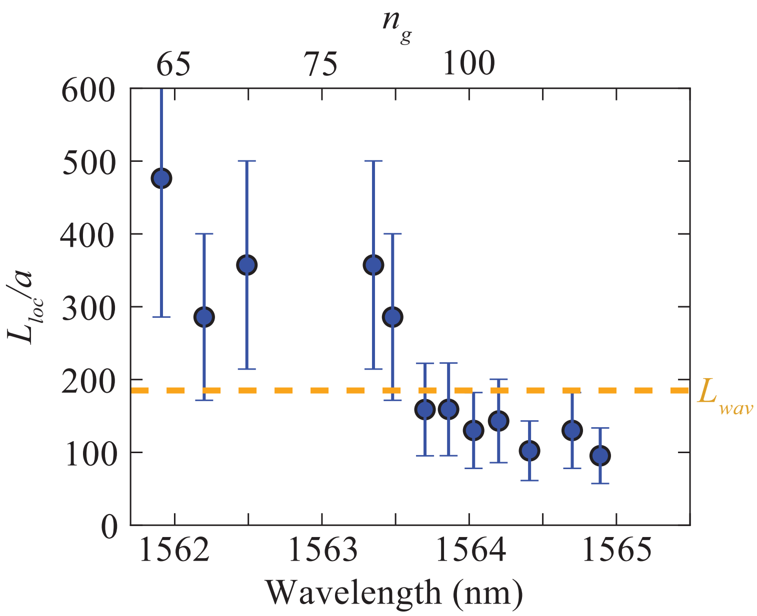

Figure 6.7: **Wavelength dependence of length of localized states.** *The dots are measurement points. The horizontal dashed line indicates L_{wav}, the length of the waveguide. Localization length becomes shorter than the waveguide at $\lambda \approx 1563.5$ nm.*

is 40%. We use this difference as the length of our error bars. On average, the state length decreases for longer wavelengths. The state length is greater than the waveguide length for $n_g \lesssim 70$, but becomes significantly shorter than the waveguide at $n_g > 80$ ($\lambda > 1563.5$ nm). It is at this wavelength that Anderson localization emerges in our sample. The group index of ~ 80 is consistent with our findings of smaller spatial spread of the field at $\lambda > 1563.5$ nm, as measured with the near-field microcope (figure 6.2b). The exact spatial length of a specific localization instance would be difficult to observe directly in the near-field data, due to the random spatial distribution of intensity, as well as the shifting of the peaks. By utilizing the diamagnetic interaction between the light and the probe, we overcome this challenge and measure the spatial extent of each localized state individually.

6.6 Discussion and conclusions

In the Anderson localization regime, waveguide transmission is negligible for the major part of the spectrum, with the exception of narrow and sparse spectral transmission peaks. In all slow-light waveguides, localization inevitably occurs, due to interaction of slow light with structural imperfections [133]. Disorder on the order of 1 nm per lattice period is sufficient to introduce localized states, for frequencies close to the band edge [38]. Even with state-of-the-art fabrication, such as in our work, such precise control is difficult to achieve. The degree of imperfection could vary, depending on the type of waveguide and fabrication method, therefore some waveguides may offer greater slow-light capability than others. To measure exactly at which group index a waveguide enters the localization regime is extremely beneficial for the future of integrated optics, and this is precisely the strongest practical benefit of our method.

On the other hand, our work contributes to the field of wave propagation in disordered media, by showing that the one of the key parameters in such studies can be measured directly on a single instance of disorder. Our measurement approach can be extended to investigate and understand the behavior of any disordered system where electromagnetic waves are present at the surface. We anticipate the method to be of use for fundamental studies of disorder and slow light in novel plasmonic waveguides [56, 73]. The fact that we use the magnetic field of light also reveals the fascinating opportunity to study disorder in systems with a strong magnetic field at optical frequencies, such as metamaterials [134, 135].

7

Applications and outlook

ABSTRACT: Based on nanophotonic phenomena addressed in this thesis, we propose a number of applications and research directions. We discuss designs for efficient coupling to guided plasmons, a plasmonic polarization demultiplexer, addressing single emitters for quantum optics, trapping atoms near nanostructures for fundamental science studies, and efficient coupling to slow light for optical switching and delay lines.

The field of nanophotonics has proven to be of interest both for fundamental science, as well as for technological applications. The understanding and control of light-matter interactions on the nanometer scale enables us to design solutions for real-world problems. In this Chapter we identify some directions in which the research presented in this thesis could be applied. The scope of the ideas ranges from research directions already in progress to proposals for realistic nanophotonic devices, to analyses of the practicality of devices already discussed in the thesis. We start with an analysis of possible uses of plasmonic nanowire and slot waveguides in classical and quantum computing, comparing them to current technology. In section 7.1.2, we propose a scheme for efficient coupling of light to plasmons in slot waveguides. Possible applications of the device used in Chapter 4 for studies of the Talbot effect are explored in sections 7.1.3 and 7.1.4. We propose a device to address single quantum emitters on a chip, and a plasmonic demultiplexer, both for possible use in quantum and classical optical communication. In section 7.2, we discuss trapping of atoms near metallic nanostructures, a research direction already being explored at Utrecht University, partially based on results related to this thesis. Finally, in section 7.3, we discuss the benefits of efficient coupling to slow light in the manner shown in Chapter 5. We show how this coupling mechanism has enabled ultra-compact slow light devices, such as directional couplers and optical buffers.

7.1 Classical and quantum optical circuits

The rapid development of photonics has been largely fueled by the need for faster communication and computing. Photonic waveguides provide a large bandwidth and low power consumption [2], making them ideal candidates for on-chip interconnects and signal carriers. In the drive to the miniaturization of computers and communication devices, it is important to place as many waveguides as possible on small areas of a chip.

Parallel to the development of classical photonics, the field of quantum optics and quantum computing, based on quantum sources of light, has emerged. Quantum sources, such as NV centers in diamond [136] or quantum dots [137], provide one photon at a time. The excited and ground states of a quantum source act as a bit in a classical computer: a quantum dot in its excited state is a bit with value 1, and in its ground state the dot is a bit with value 0. However, a quantum system can also exist in a superposition of the two states. Since the superposition can store additional information, quantum bits based on quantum sources of light provide additional computing power compared to their classical counterparts [138]. Interfacing such sources to nanometer-scaled optical components holds promise for on-chip quantum computing, and has been gaining an increasing amount of attention of researchers in recent years [139, 140, 141]. Techniques already exist for deterministically placing single emitters at desired locations on a chip [141]. In order to use these small and weak sources of light, however, their efficiency and directionality must be enhanced. A common method for overcoming these hurdles is to make use of the Purcell effect [142]. The effect, discovered for radio frequencies in 1946, is one of an enhanced rate of spontaneous emission of atoms placed in environments with a high density of electromagnetic states. Additionally, if the states are those of waveguide mode, the source emits preferentially into that mode. The emission enhancement factor is high when the cross-sectional area of the waveguide mode is low [143]. Here, we show how the structures presented in this thesis could be used as components of classical and quantum computers, making use of their small size and mode cross-section.

7.1.1 Nanowires and slot waveguides for photonic circuits and quantum computing

The nanowires described in Chapter 3 and slot waveguides described in Chapter 2 sustain small mode cross-sections, making them ideal for use as components of possible nano-scale circuits, as well as for use in quantum computers. In general, the cross-sectional area of a plasmonic mode on a gold nanowire is on the order of $\sim 100\,\mathrm{nm}^2$, while the equivalent area in a dielectric is $\sim 1\,\mu\mathrm{m}^2$. The smaller modal cross-section allows for a tenfold increase of on-chip communication channels per unit area when using nanowires, compared to the more common dielectric waveguides. We also expect the small mode area to enhance spontaneous emission of quantum sources of light by an order of magnitude, compared to sources placed in the vicinity of dielectric waveguides, due to a higher density of electromagnetic states [6]. The small area of nanowire plasmons and their enhanced interaction with single emitters are ideal for circuits based on single-photon emitters and detectors, connected by plasmonic nanowires, all packaged to areas as small as several square micrometers.

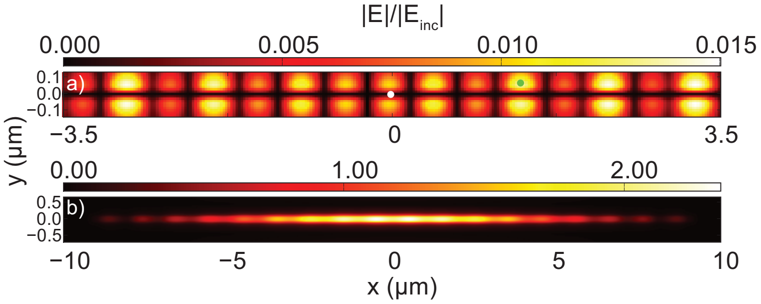

Figure 7.1: Placing single emitters in the plasmon field of a slot waveguide. (a) Electric field component parallel to the waveguide. The electric field has a node in the middle of the slot, therefore the Purcell effect is negligible there. (b) Electric field component perpendicular to the waveguide. This component couples to free-space radiation.

The arguments outlined above hold for plasmonic slot waveguides as well. They too have small mode cross-sections, comparable to those of nanowires. In fact, their open geometry is even more appealing to the introduction of single emitters between the two metal sidewalls. In the case of slot waveguides, our study explores a crucial aspect of the plasmonic mode: symmetry. Dipolar sources of radiation, such as single emitters, emit radiation in directions perpendicular to the dipole axis. Furthermore, the polarization of this radiation is parallel to the axis of the dipole. When slot waveguides are to be used for coupling to such sources, care must be taken that the dipole is oriented and positioned properly. In figure 7.1, we plot the electric field in a slot waveguide, for the electric field component oriented parallel (a) and perpendicular (b) to the waveguide. If the dipole is oriented parallel to the waveguide axis, it should not be positioned in the middle of the waveguide. Such a dipole is illustrated as a white dot in figure 7.1a. The plasmonic mode has a dip in amplitude in the middle of the waveguide for this orientation, so that the benefits of the Purcell factor are removed there. The source should in fact be placed closer to one of the sidewalls of the slot, indicated by the green dot in the same image. If, on the other hand, the dipole is to be oriented perpendicular to the waveguide axis, it is important to take into consideration figure 7.1b. There we observe not only propagating plasmons, but also the incident laser beam, evident as a Gaussian-shaped background. For this dipole orientation, the dipole can couple not only to propagating plasmons, but also to free-space radiation, reducing the benefits of the Purcell effect. On the other hand, in experimental studies, the original orientation of the dipole may be unknown. Our slot waveguide can be used to determine this orientation. As an example, if the dipole is placed in the middle of the slot and it does not emit, this means that the dipole axis is oriented parallel to the waveguide, where the intensity in the mode is zero. Consequently, building on research presented in Chapter 2, we show a possibility to couple quantum emitters to plasmons in slot waveguides, but also to use slot waveguides to determine the orientation of quantum emitters.

7.1.2 Coupling light to the nanoscale

We have proposed in the previous subsection that plasmonic slot waveguides are good candidates for components of future integrated quantum optical computers. In order to bring out the full potential of these structures, it is important to devise means of coupling to their plasmon mode efficiently. In Chapter 2, we launch plasmons by scattering a laser beam off the edges of the slot. A more efficient method of coupling is described in [69], where the authors use a taper to couple a freely propagating beam to plasmons. Here, we propose another method of launching slot plasmons, based on grating diffraction.

Figure 7.2 depicts the design of our coupler. A slot is fabricated in a metal film, for example by focused ion beam milling. Near one end of the slot, a grating is made by milling periodic arrays of square holes on both sides of the slot. Light incident on the grating will be converted to plasmons. The grating coupling mechanism is commonly used to couple to surface plasmons propagating on a gold film [9]. The pitch of the grating should be chosen carefully, to provide the correct magnitude of in-plane momentum, necessary for phase-matching between the incident laser beam and slot plasmons. The momentum of the plasmons (k_{SPP}) should be equal to the sum of the momentum of the incident beam (k_{inc}) and the momentum provided by the grating ($k_{grating}$):

$$k_{inc} + k_{grating} = k_{SPP}, \tag{7.1}$$

from which

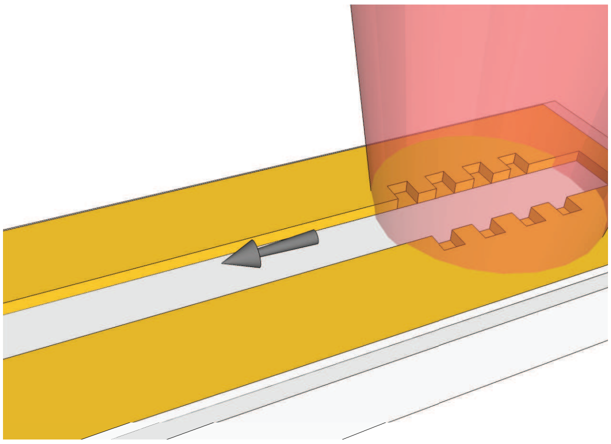

Figure 7.2: A design to couple light to a nanoscale waveguide for photonic integration on a chip, employing grating coupling. The grating adds in-plane momentum to the incident laser beam and launches plasmons in the direction indicated by the grey arrow.

$$\frac{2\pi}{\lambda_0} + \frac{2\pi}{md} = \frac{2\pi}{\lambda_{SPP}}, \tag{7.2}$$

where λ_0 is the free-space wavelength, m is the grating order, d is the pitch of the grating, and λ_{SPP} is the wavelength of the plasmons in the waveguide. For simplicity, equation 7.2 is given for normal incidence. At a given free-space wavelength, the plasmon wavelength and momentum vary depending on the slot width. For example, for slots which are 40 nm wide, such as those discussed in Chapter 2, and $\lambda_0 = 1.5\,\mu$m the plasmon wavelength is $1\,\mu$m. Using equation 7.2, it is easy to calculate that the correct pitch of the grating is $1\,\mu$m.

With this method, plasmons are generated which propagate in both directions in the slot. Plasmons that propagate towards the nearest edge (in the direction opposite from the grey arrow in figure 7.2) are scattered and reflected at the edge. If this edge is placed such that the reflected plasmons interfere constructively with those propagating in the opposite direction, we expect efficient unidirectional plasmon launching in the slot [144], so that we double the efficiency of the launcher.

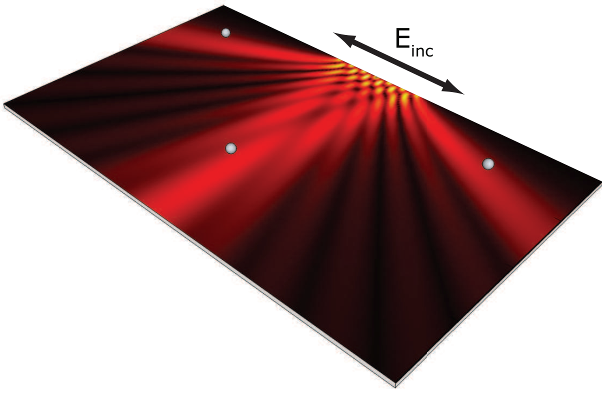

Figure 7.3: A design to selectively address single emitters for on-chip quantum computing. The black arrow indicates the polarization direction of the incident beam; this direction determines which of the single emitters, shown as grey spheres, are addressed by the plasmonic field.

7.1.3 Polarization-controlled excitation of single photon sources

One requirement of quantum computing is the ability to individually address single photon sources. This is not an obviously easy task, due to the small size of the sources. In this section we propose a device consisting of a nanohole array, like the one discussed in Chapter 4, to selectively excite emitters depending on the polarization of the excitation light. The device is sketched in figure 7.3.

The figure represents a chain of seven nanoholes in a gold film on top of a substrate. The electric field intensity pattern depicted in the figure is obtained theoretically, from a summation of non-interacting dipoles. This approach describes the actual experimental patterns well, as we have shown earlier [145]. We have also shown that by rotating the polarization of the incident beam (E_{inc}) in the plane of the film, we can control whether the optical energy is delivered to the middle beam, or the two side beams. We propose to place single emitters, portrayed as grey spheres in the image, in the path of the beams. Depending on the polarization of the incident beam, either the central emitter, or the two side-emitters will be excited. Since polarization of the incident beam is easily controllable with regular polarization optics, our system offers an easy way to control the excitation state of individual emitters. An important aspect of our system is that it can be easily extended to include a bigger number of single emitters. By increasing the pitch of the grating, or decreasing the wavelength, more diffraction orders appear in the form of plasmon beams into which additional emitters can be positioned.

7.1.4 Nanoscale polarization demultiplexer

In this section, we outline a design for a polarization demultiplexer based on phenomena described in Chapters 4 and 3. In telecommunications, multiplexing is a method by which multiple data streams are combined into one signal over a shared medium [146]. One method of multiplexing is polarization multiplexing, where different data streams are encoded into different polarization states of a light beam. At the receiving end of the communication channel, the signal should be *demultiplexed*, i.e. each polarization state needs to be separated prior to processing. In practice, multiplexed signals are processed through so-called “polarization diversity” [147, 148] schemes, in which polarization states are separated, each channel processed individually, after which the channels are recombined. The key is to be able to send the signals to identical channels, such that the same operation on two different channels would result in the same changes in the channels. State-of-the-art devices use photonic waveguides, which result in demultiplexer sizes on the order of $600\,\mu$m [148]. Our designed device demultiplexes polarization multiplexed signals and sends them to separate plasmon nanowire waveguide channels, in which signals originating from different polarization states can be processed individually on the nanometer scale. The demultiplexer takes up an area of only several tens of micrometers squared, which is an order of magnitude smaller than photonic demultiplexers. In addition, the nanowires have small modal cross-sectional areas, as discussed earlier, making our designed device a candidate for addressing individual quantum emitters, for quantum information processing. Our design is sketched in figure 7.4.

A laser beam, carrying the polarization-multiplexed signal, is incident on a chain of nanoholes in a gold film. Similar to the scheme outlined in the previous section, different states of polarization are sent to plasmons propagating in different directions. Tapers in each direction collect the plasmons and adiabatically transform them to modes propagating on gold nanowires. We have already shown that this coupling can have an efficiency greater

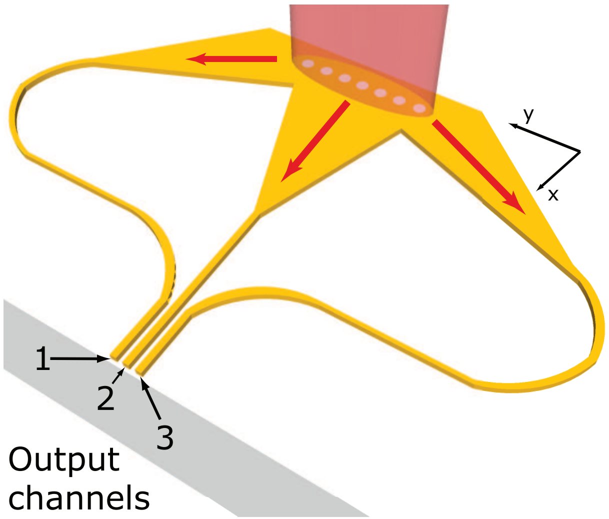

Figure 7.4: A design for a plasmonic polarization demultiplexer. Different polarization components of the incident optical beam are sent to different plasmonic nanowire output channels.

than 50 % [73]. The wires are subsequently brought to be parallel to each other, so that the data streams travel in the same direction. If an emitter is brought to the vicinity of each nanowire in our multiplexer, then we can encode different information in different polarization states of the input light, and this information will be transferred to excitation states of the emitters. The ability to optically detect and control the states of quantum emitters is important for quantum computing and communication. This device can be made to be very small, which is desirable for on-chip integrated components. In Chapter 3, we show that for radii of curvature as small as 4 μm the bending losses in curved nanowires are negligible. Using this radius, the three bends in the design extend a total of 12 μm in the x direction. The tapers which we use have a base opening of 5 μm, although that size is not crucial and could be further reduced through optimization. Using the unoptimized taper size, the distance in the x direction from the holes to the output is only 17 μm. In the y direction, using a realistic taper length of 10 μm, the maximum distance from the holes to the end of the device is 14 μm. Altogether, the device can be fitted to an area $17 \times 38\,\mu$m.

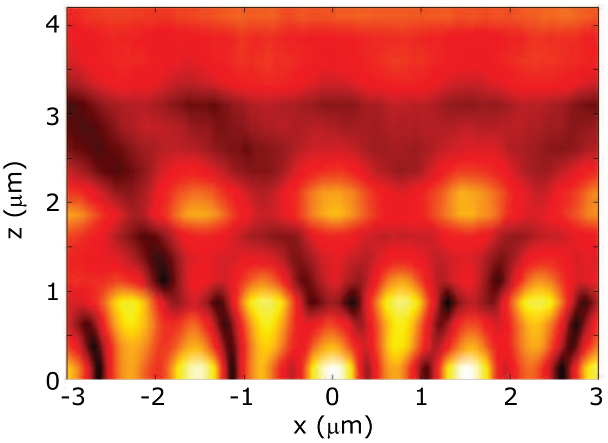

Figure 7.5: Measurements of the electric field amplitude above a grating of nanoholes in a gold film. The grating is positioned at $z = 0$*. Interference of light emanating from individual nanoholes results in the Talbot effect, causing isolated pockets of light above the grating. Research is in progress to trap atoms in these pockets, for studies of fundamental properties of the light-matter interaction.*

7.2 Trapping atoms with nanostructures

In an extension to the topic of Chapter 4, we performed a pilot study to test the feasibility of trapping atoms using nanohole arrays. Results of this pilot study were used as part of a successful application for a Dutch VIDI grant in the 2009 round. The proposal "Atom-light interactions in plasmonic nanostructures" was granted funding, and research is now underway at Utrecht University to trap atoms near an array of nanoholes.

A square array of holes, with a pitch of $1.5\,\mu$m and a 0.5 duty cycle, was fabricated with electron-beam lithography in a gold film on a glass substrate. A collimated laser beam with a free-space wavelength of $1.55\,\mu$m is used to illuminate the array. We probe the electric field as a function of height above the surface of the grating with a near-field microscope. We find isolated regions of high intensity, surrounded by low-intensity regions (see figure 7.5). The pattern results from a manifestation of the Talbot effect, similar to that observed with surface plasmon polaritons in Chapter 4. Atoms can be trapped in the high-intensity regions. The granted proposal investigates the idea that the properties of the atoms can be modified by the presence of the nanostructure, but also conversely: the state of the atom can modify resonance properties of the hole array. These are extremely relevant issues, given the drive in developing active photonic and plasmonic devices.

7.3 Slow light in photonic crystal waveguides

Slow light in photonic crystals has applications ranging from optical delay lines, to buffers, to switches and modulators [7, 25]. Photonic crystals, in particular, lend themselves to slow light applications, as they can be easily integrated on-chip. However, it has long been held that coupling to this slow light in photonic crystals must be inefficient, in part due to the mismatch in mode profiles between fast light and slow light in PhCs [112]. In Chapter 5, we show the first direct experimental observation of evanescent modes at the interface to slow light. Evanescent modes have been theoretically predicted to play a crucial role in efficient coupling to slow light [113, 114]. By confirming the existence of these modes and exploring the nature of the coupling mechanism, we open up the opportunity to engineer new slow-light devices with high coupling efficiencies. We hence expect our findings to be of importance to scientists as well as engineers working in the field of slow light.

Devices which use the efficient coupling through evanescent modes are already being studied. One such device is a photonic directional coupler, described in [29] and shown in figure 7.6. In this coupler, light enters through an input port (indicated with a red arrow and labelled “in” in the figure), after which it can exit through either of two output ports. The port through which the light exits can be switched by optical pumping. This work relies on slow light to make the device only $5.2\,\mu$m long. Efficient excitation of slow light is achieved with the technique described in Chapter 5 of this thesis, with the interface region only $2.4\,\mu$m long.

As described in Chapter 6, structural disorder affects the propagation of light in photonic crystal waveguides. With state-of-the-art fabrication, the residual disorder is on the order of the lattice constant of silicon [149]. Even this small amount of disorder is enough to put limitations on the achievable slow-down of light. In [150], we find design routes to reduce propagation losses in photonic crystal waveguides. For such a careful study of losses, it is imperative that the coupling to slow light is efficient. Again,

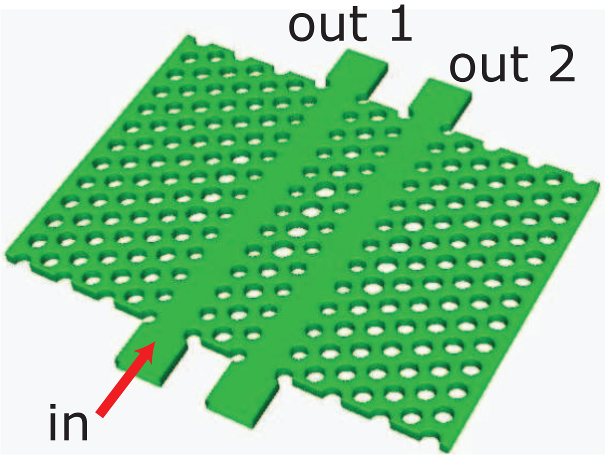

Figure 7.6: A photonic crystal directional coupler. Light enters through the port labelled "in". Light can exit through output port 1 or 2, depending on whether the sample is optically pumped with another laser pulse. The coupler makes use of slow light to keep the device length small. Efficient coupling to slow light is achieved with the use of evanescent modes.

we have used the coupling mechanism described in Chapter 5, to efficiently excite slow light.

We anticipate that an increasing number of photonic crystal slow-light devices will utilize the coupler based on evanescent modes. The coupler is short [29] and efficient [115], ideal for use in miniature devices.

Bibliography

[1] G. P. Agrawal, *Fiber-optic communication systems* (Wiley, New York, 2002).

[2] D. Miller, “Device requirements for optical interconnects to silicon chips,” Proceedings of the IEEE **97**, 1166–1185 (2009).

[3] E. Ozbay, “Plasmonics: Merging photonics and electronics at nanoscale dimensions,” Science **311**, 189–193 (2006).

[4] C. Weisbuch and N. A. J. Rarity, eds., *Microcavities and Photonic Bandgaps: Physics and Applications* (Kluwer, Dordrecht, 1996).

[5] P. Bharadwaj, B. Deutsch, and L. Novotny, “Optical antennas,” Adv. Opt. Photon. **1**, 438–483 (2009).

[6] D. E. Chang, A. S. S, P. R. Hemmer, and M. D. Lukin, “Strong coupling of single emitters to surface plasmons,” Phys. Rev. B **76**, 035420 (2007).

[7] T. F. Krauss, “Why do we need slow light?” Nat. Photonics **2**, 448–450 (2008).

[8] E. Abbe, “Beitrage zur theorie des mikroskops und der mikroskopischen wahrnehmung,” Archiv f. Mikroskop. Anat. **9**, 413 (1873).

[9] H. Raether, *Surface Plasmons* (Springer, Berlin, 1988).

[10] W. L. Barnes, A. Dereux, and T. W. Ebbesen, “Surface plasmon subwavelength optics,” Nature **424**, 824–830 (2003).

[11] S. Lal, S. Link, and N. J. Halas, “Nano-optics from sensing to waveguiding,” Nat. Photonics **1**, 641–648 (2007).

[12] E. Kretschmann and H. Raether, “Radiative decay of nonradiative surface plasmons excited by light,” Z. Naturforsch. A **23**, 2135 (1968).

[13] B. Hecht, H. Bielefeldt, L. Novotny, Y. Inouye, and D. W. Pohl, “Local excitation, scattering, and interference of surface plasmons,” Phys. Rev. Lett. **77**, 1889 (1996).

[14] A.-L. Baudrion, F. de Leon-Perez, O. Mahboub, A. Hohenau, H. Ditlbacher, F. J. Garcia-Vidal, J. Dintinger, T. W. Ebbesen, L. Martin-Moreno, and J. R. Krenn, “Coupling efficiency of light to surface plasmon polariton for single subwavelength holes in a gold film,” Opt. Express **16**, 3420–3429 (2008).

[15] J. J. Burke, G. I. Stegeman, and T. Tamir, “Surface-polariton-like waves guided by thin, lossy metal films,” Phys. Rev. B **33**, 5186 (1986).

[16] E. N. Economou, “Surface plasmons in thin films,” Phys. Rev. **182**, 539 (1969).

[17] D. Sarid, “Long-range surface-plasma waves on very thin metal films,” Phys. Rev. Lett. **47**, 1927 (1981).

[18] E. Verhagen, “Subwavelength light confinement with surface plasmon polaritons,” Ph.D. thesis, FOM Institute AMOLF (2009).

[19] R. Zia, M. D. Selker, P. B. Catrysse, and M. L. Brongersma, “Geometries and materials for subwavelength surface plasmon modes,” J. Opt. Soc. Am. A **21**, 2442–2446 (2004).

[20] J. A. Dionne, L. A. Sweatlock, H. A. Atwater, and A. Polman, “Plasmon slot waveguides: Towards chip-scale propagation with subwavelength-scale localization,” Phys. Rev. B **73**, 035407 (2006).

[21] J. D. Joannopoulos, S. G. Johnson, J. N. Winn, and R. D. Meade, *Photonic Crystals: Molding the Flow of Light (2nd ed.)* (Princeton University Press, 2008).

[22] S. John, “Strong localization of photons in certain disordered dielectric superlattices,” Phys. Rev. Lett. **58**, 2486 (1987).

[23] E. Yablonovitch, “Inhibited spontaneous emission in solid-state physics and electronics,” Phys. Rev. Lett. **58**, 2059 (1987).

[24] C. Kittel, *Introduction to Solid State Physics (7th ed.)* (John Wiley and Sons, Inc., 1996).

[25] T. Baba, “Slow light in photonic crystals,” Nat. Photonics **2**, 465–473 (2008).

[26] Y. A. Vlasov, M. O’Boyle, H. F. Hamann, and S. J. McNab, “Active control of slow light on a chip with photonic crystal waveguides,” Nature **438**, 65–69 (2005).

[27] R. S. Tucker, P.-C. Ku, and C. J. Chang-Hasnain, “Slow-light optical buffers: Capabilities and fundamental limitations,” J. Lightwave Technol. **23**, 4046 (2005).

[28] D. M. Beggs, T. P. White, L. O’Faolain, and T. F. Krauss, “Ultracompact and low-power optical switch based on silicon photonic crystals,” Opt. Lett. **33**, 147–149 (2008).

[29] T. Kampfrath, D. M. Beggs, T. P. White, M. Burresi, D. van Oosten, T. F. Krauss, and L. Kuipers, “Ultrafast rerouting of light via slow modes in a nanophotonic directional coupler,” Appl. Phys. Lett. **94**, 241119 (2009).

[30] B. Corcoran, C. Monat, C. Grillet, D. J. Moss, B. J. Eggleton, T. P. White, L. O’Faolain, and T. F. Krauss, “Green light emission in silicon through slow-light enhanced third-harmonic generation in photonic-crystal waveguides,” Nat. Photonics **3**, 206–210 (2009).

[31] M. Soljaĉić and J. D. Joannopoulos, “Enhancement of nonlinear effects using photonic crystals,” Nat Mater **3**, 211–219 (2004).

[32] R. J. P. Engelen, D. Mori, T. Baba, and L. Kuipers, “Two regimes of slow-light losses revealed by adiabatic reduction of group velocity,” Phys. Rev. Lett. **101**, 103901 (2008).

[33] R. Biswas, Z. Y. Li, and K. M. Ho, “Impedance of photonic crystals and photonic crystal waveguides,” Appl. Phys. Lett. **84**, 1254–1256 (2004).

[34] N. Le Thomas, H. Zhang, J. Jágerská, V. Zabelin, R. Houdré, I. Sagnes, and A. Talneau, “Light transport regimes in slow light photonic crystal waveguides,” Phys. Rev. B **80**, 125332 (2009).

[35] S. Mazoyer, P. Lalanne, J. Rodier, J. Hugonin, M. Spasenović, L. Kuipers, D. Beggs, and T. Krauss, “Statistical fluctuations of transmission in slow light photonic-crystal waveguides,” Opt. Express **18**, 14654–14663 (2010).

[36] S. Mazoyer, J. P. Hugonin, and P. Lalanne, “Disorder-induced multiple scattering in photonic-crystal waveguides,” Phys. Rev. Lett. **103**, 063903 (2009).

[37] P. D. García, S. Smolka, S. Stobbe, and P. Lodahl, “Density of states controls anderson localization in disordered photonic crystal waveguides,” Phys. Rev. B **82**, 165103 (2010).

[38] V. Savona, “Electromagnetic modes of a disordered photonic crystal,” Phys. Rev. B **83**, 085301 (2011).

[39] P. W. Anderson, “Absence of diffusion in certain random lattices,” Phys. Rev. **109**, 1492 (1958).

[40] J. Bertolotti, S. Gottardo, D. S. Wiersma, M. Ghulinyan, and L. Pavesi, “Optical necklace states in anderson localized 1d systems,” Phys. Rev. Lett. **94**, 113903 (2005).

[41] S. Jung, G. M. Rutter, N. N. Klimov, D. B. Newell, I. Calizo, A. R. Hight-Walker, N. B. Zhitenev, and J. A. Stroscio, “Evolution of microscopic localization in graphene in a magnetic field from scattering resonances to quantum dots,” Nat Phys **7**, 245–251 (2011).

[42] H. Hu, A. Strybulevych, J. H. Page, S. E. Skipetrov, and B. A. van Tiggelen, “Localization of ultrasound in a three-dimensional elastic network,” Nat Phys **4**, 945–948 (2008).

[43] J. Billy, V. Josse, Z. Zuo, A. Bernard, B. Hambrecht, P. Lugan, D. Clement, L. Sanchez-Palencia, P. Bouyer, and A. Aspect, “Direct observation of anderson localization of matter waves in a controlled disorder,” Nature **453**, 891–894 (2008).

[44] G. Roati, C. D'Errico, L. Fallani, M. Fattori, C. Fort, M. Zaccanti, G. Modugno, M. Modugno, and M. Inguscio, "Anderson localization of a non-interacting bose-einstein condensate," Nature **453**, 895–898 (2008).

[45] D. S. Wiersma, P. Bartolini, A. Lagendijk, and R. Righini, "Localization of light in a disordered medium," Nature **390**, 671–673 (1997).

[46] L. Novotny and B. Hecht, *Principles of Nano-Optics* (Cambridge University Press, 2008).

[47] D. W. Pohl, W. Denk, and M. Lanz, "Optical stethoscopy: Image recording with resolution lambda/20," Appl. Phys. Lett. **44**, 651–653 (1984).

[48] M. Völcker, W. Krieger, and H. Walther, "Laser-driven scanning tunneling microscope," Phys. Rev. Lett. **66**, 1717 (1991).

[49] E. Betzig, M. Isaacson, and A. Lewis, "Collection mode near-field scanning optical microscopy," Appl. Phys. Lett. **51**, 2088–2090 (1987).

[50] K. Karrai and R. D. Grober, "Piezoelectric tip-sample distance control for near field optical microscopes," Appl. Phys. Lett. **66**, 1842–1844 (1995).

[51] M. Burresi, "Nanoscale investigation of light-matter interactions mediated by magnetic and electric coupling," Ph.D. thesis, FOM Institute AMOLF (2009).

[52] M. L. M. Balistreri, J. P. Korterik, L. Kuipers, and N. F. van Hulst, "Local observations of phase singularities in optical fields in waveguide structures," Phys. Rev. Lett. **85**, 294 (2000).

[53] M. Balistreri, "Coherent imaging of guided optical fields," Ph.D. thesis, University of Twente (2000).

[54] M. Burresi, R. J. P. Engelen, A. Opheij, D. van Oosten, D. Mori, T. Baba, and L. Kuipers, "Observation of polarization singularities at the nanoscale," Phys. Rev. Lett. **102**, 033902 (2009).

[55] A. H. J. Yang, S. D. Moore, B. S. Schmidt, M. Klug, M. Lipson, and D. Erickson, "Optical manipulation of nanoparticles and biomolecules in sub-wavelength slot waveguides," Nature **457**, 71–75 (2009).

[56] S. I. Bozhevolnyi, V. S. Volkov, E. Devaux, J.-Y. Laluet, and T. W. Ebbesen, "Channel plasmon subwavelength waveguide components including interferometers and ring resonators," Nature **440**, 508–511 (2006).

[57] G. Veronis and S. Fan, "Guided subwavelength plasmonic mode supported by a slot in a thin metal film," Opt. Lett. **30**, 3359–3361 (2005).

[58] L. Liu, Z. Han, and S. He, "Novel surface plasmon waveguide for high integration," Opt. Express **13**, 6645–6650 (2005).

[59] D. F. P. Pile, T. Ogawa, D. K. Gramotnev, Y. Matsuzaki, K. C. Vernon, K. Yamaguchi, T. Okamoto, M. Haraguchi, and M. Fukui, "Two-dimensionally localized modes of a nanoscale gap plasmon waveguide," Appl. Phys. Lett. **87**, 261114 (2005).

[60] W. Cai, W. Shin, S. Fan, and M. L. Brongersma, "Elements for plasmonic nanocircuits with three-dimensional slot waveguides," Adv. Mater. **22**, 5120–5124 (2010).

[61] H. Zhan, R. Mendis, and D. M. Mittleman, "Superfocusing terahertz waves below lambda/250 using plasmonic parallel-plate waveguides," Opt. Express **18**, 9643–9650 (2010).

[62] S. Nie and S. R. Emory, "Probing single molecules and single nanoparticles by surface-enhanced raman scattering," Science **275**, 1102–1106 (1997).

[63] A. Bouhelier, M. Beversluis, A. Hartschuh, and L. Novotny, "Near-field second-harmonic generation induced by local field enhancement," Phys. Rev. Lett. **90**, 013903 (2003).

[64] J. A. H. van Nieuwstadt, M. Sandtke, R. H. Harmsen, F. B. Segerink, J. C. Prangsma, S. Enoch, and L. Kuipers, "Strong modification of the nonlinear optical response of metallic subwavelength hole arrays," Phys. Rev. Lett. **97**, 146102 (2006).

[65] S. Kim, J. Jin, Y.-J. Kim, I.-Y. Park, Y. Kim, and S.-W. Kim, "High-harmonic generation by resonant plasmon field enhancement," Nature **453**, 757–760 (2008).

[66] A. R. Davoyan, I. V. Shadrivov, and Y. S. Kivshar, "Nonlinear plasmonic slot waveguides," Opt. Express **16**, 21209–21214 (2008).

[67] Y. C. Jun, R. D. Kekatpure, J. S. White, and M. L. Brongersma, "Nonresonant enhancement of spontaneous emission in metal-dielectric-metal plasmon waveguide structures," Phys. Rev. B **78**, 153111 (2008).

[68] D. F. P. Pile, D. K. Gramotnev, R. F. Oulton, and X. Zhang, "On long-range plasmonic modes in metallic gaps," Opt. Express **15**, 13669–13674 (2007).

[69] L. Chen, J. Shakya, and M. Lipson, "Subwavelength confinement in an integrated metal slot waveguide on silicon," Opt. Lett. **31**, 2133–2135 (2006).

[70] J. A. Dionne, H. J. Lezec, and H. A. Atwater, "Highly confined photon transport in subwavelength metallic slot waveguides," Nano Lett. **6**, 1928–1932 (2006).

[71] H. T. Miyazaki and Y. Kurokawa, "Squeezing visible light waves into a 3-nm-thick and 55-nm-long plasmon cavity," Phys. Rev. Lett. **96**, 097401 (2006).

[72] Y. Satuby and M. Orenstein, "Surface plasmon polariton waveguiding: From multimode stripe to a slot geometry," Appl. Phys. Lett. **90**, 251104 (2007).

[73] E. Verhagen, M. Spasenović, A. Polman, and L. Kuipers, "Nanowire plasmon excitation by adiabatic mode transformation," Phys. Rev. Lett. **102**, 203904 (2009).

[74] R. Yang, R. A. Wahsheh, Z. Lu, and M. A. G. Abushagur, "Efficient light coupling between dielectric slot waveguide and plasmonic slot waveguide," Opt. Lett. **35**, 649–651 (2010).

[75] Y. Vlasov, W. M. J. Green, and F. Xia, “High-throughput silicon nanophotonic wavelength-insensitive switch for on-chip optical networks,” Nat. Photonics **2**, 242–246 (2008).

[76] F. Morichetti, A. Melloni, C. Ferrari, and M. Martinelli, “Error-free continuously-tunable delay at 10 gbit/s in a reconfigurable on-chip delay-line,” Opt. Express **16**, 8395–8405 (2008).

[77] N. Sherwood-Droz, H. Wang, L. Chen, B. G. Lee, A. Biberman, K. Bergman, and M. Lipson, “Optical 4x4 hitless slicon router for optical networks-on-chip (noc),” Opt. Express **16**, 15915–15922 (2008).

[78] M. H. Shih, W. J. Kim, W. Kuang, J. R. Cao, S.-J. Choi, J. D. O’Brien, and P. D. Dapkus, “Experimental characterization of the reflectance of 60[degree] waveguide bends in photonic crystal waveguides,” Appl. Phys. Lett. **86**, 191104–3 (2005).

[79] M. Ayre, T. Karle, L. Wu, T. Davies, and T. Krauss, “Experimental verification of numerically optimized photonic crystal injector, y-splitter, and bend,” IEEE J. Sel. Areas Commun. **23**, 1390–1395 (2005).

[80] I. Ntakis, P. Pottier, and R. M. De La Rue, “Optimization of transmission properties of two-dimensional photonic crystal channel waveguide bends through local lattice deformation,” J. Appl. Phys. **96**, 12–18 (2004).

[81] M. Lipson, “Guiding, modulating, and emitting light on silicon-challenges and opportunities,” J. Lightwave Technol. **23**, 4222–4238 (2005).

[82] Y. Vlasov and S. McNab, “Losses in single-mode silicon-on-insulator strip waveguides and bends,” Opt. Express **12**, 1622–1631 (2004).

[83] T. W. Ebbesen, C. Genet, and S. I. Bozhevolnyi, “Surface-plasmon circuitry,” Phys. Today **61**, 44–50 (2008).

[84] P. Berini, “Plasmon-polariton waves guided by thin lossy metal films of finite width: Bound modes of symmetric structures,” Phys. Rev. B **61**, 10484– (2000).

[85] D. K. Gramotnev and D. F. P. Pile, “Single-mode subwavelength waveguide with channel plasmon-polaritons in triangular grooves on a metal surface,” Appl. Phys. Lett. **85**, 6323–6325 (2004).

[86] B. Steinberger, A. Hohenau, H. Ditlbacher, A. L. Stepanov, A. Drezet, F. R. Aussenegg, A. Leitner, and J. R. Krenn, “Dielectric stripes on gold as surface plasmon waveguides,” Appl. Phys. Lett. **88**, 094104 (2006).

[87] M. Spasenović, D. van Oosten, E. Verhagen, and L. Kuipers, “Measurements of modal symmetry in subwavelength plasmonic slot waveguides,” Appl. Phys. Lett. **95**, 203109 (2009).

[88] J. Takahara, S. Yamagishi, H. Taki, A. Morimoto, and T. Kobayashi, “Guiding of a one-dimensional optical beam with nanometer diameter,” Opt. Lett. **22**, 475–477 (1997).

[89] H.-S. Chu, E.-P. Li, P. Bai, and R. Hegde, “Optical performance of single-mode hybrid dielectric-loaded plasmonic waveguide-based components,” Appl. Phys. Lett. **96**, 221103–3 (2010).

[90] T. Holmgaard, Z. Chen, S. I. Bozhevolnyi, L. Markey, A. Dereux, A. V. Krasavin, and A. V. Zayats, “Bend- and splitting loss of dielectric-loaded surface plasmon-polariton waveguides,” Opt. Express **16**, 13585–13592 (2008).

[91] B. Steinberger, A. Hohenau, H. Ditlbacher, F. R. Aussenegg, A. Leitner, and J. R. Krenn, “Dielectric stripes on gold as surface plasmon waveguides: Bends and directional couplers,” Appl. Phys. Lett. **91**, 081111 (2007).

[92] M. I. Stockman, “Nanofocusing of optical energy in tapered plasmonic waveguides,” Phys. Rev. Lett. **93**, 137404 (2004).

[93] Z. Zhu and T. Brown, “Full-vectorial finite-difference analysis of microstructured optical fibers,” Opt. Express **10**, 853–864 (2002).

[94] E. A. Marcatili, “Bends in optical dielectric guides,” Bell Syst. Tech. J. **48**, 2103 (1969).

[95] R. G. Hunsperger, *Integrated optics: Theory and technology, 4th edition* (Springer-Verlag, Berlin Heidelberg, 1995).

[96] H. F. Talbot, "Facts relating to optical science, no. iv," Phil. Mag. **9**, 401–407 (1836).

[97] L. Rayleigh, "On copying diffraction-grating and on some phenomena connected with therewith," Phil. Mag. **11**, 196–205 (1881).

[98] E. A. Hiedemann and M. A. Breazale, "Secondary interference in the fresnel zone of gratings," J. Opt. Soc. Am. **49**, 372–374 (1959).

[99] J. T. Winthrop and C. R. Worthington, "Theory of fresnel images. i. plane periodic objects in monochromatic light," J. Opt. Soc. Am. **55**, 373–380 (1965).

[100] M. V. Berry and S. Klein, "Integer, fractional and fractal talbot effects," J. Mod. Opt. **43**, 2139–2164 (1996).

[101] M. S. Chapman, C. R. Ekstrom, T. D. Hammond, J. Schmiedmayer, B. E. Tannian, S. Wehinger, and D. E. Pritchard, "Near-field imaging of atom diffraction gratings: The atomic talbot effect," Phys. Rev. A **51**, R14–R17 (1995).

[102] B. Brezger, L. Hackermüller, S. Uttenthaler, M. A. J. Petschinka, and A. Zeilinger, "Matter-wave interferometer for large molecules," Phys. Rev. Lett. **88**, 100404 (2002).

[103] M. R. Dennis, N. I. Zheludev, and F. J. G. de Abajo, "The plasmon talbot effect," Opt. Express **15**, 9692–9700 (2007).

[104] S. Cherukulappurath, D. Heinis, J. Cesario, N. F. van Hulst, S. Enoch, and R. Quidant, "Local observation of plasmon focusing in talbot carpets," Opt. Express **17**, 23772–23784 (2009).

[105] P. B. Johnson and R. W. Christy, "Optical constants of the noble metals," Phys. Rev. B **6**, 4370–4379 (1972).

[106] C. Sönnichsen, A. C. Duch, G. Steiniger, M. Koch, G. von Plessen, and J. Feldmann, "Launching surface plasmons into nano-holes in metal films," Appl. Phys. Lett. **76**, 140–142 (2000).

[107] L. Yin, V. K. Vlasko-Vlasov, A. Rydh, J. Pearson, U. Welp, S.-H. Chang, S. K. Gray, G. C. Schatz, D. B. Brown, and C. W. Kimball,

"Surface plasmons at single nanoholes in au films," Appl. Phys. Lett. **85**, 467–469 (2004).

[108] P. Lalanne and J. P. Hugonin, "Interaction between optical nano-objects at metallo-dielectric interfaces," Nat. Phys. **2**, 551–556 (2006).

[109] A. Sommerfeld, "Über die ausbreitlung der wellen in der drahtlosen telegraphie," Ann. der Physik **28**, 665–736 (1909).

[110] J. Li, T. P. White, L. O'Faolain, A. Gomez-Iglesias, and T. F. Krauss, "Systematic design of flat band slow light in photonic crystal waveguides," Opt. Express **16**, 6227–6232 (2008).

[111] T. Baba, T. Kawaaski, H. Sasaki, J. Adachi, and D. Mori, "Large delay-bandwidth product and tuning of slow light pulse in photonic crystal coupled waveguide," Opt. Express **16**, 9245–9253 (2008).

[112] Y. A. Vlasov and S. J. McNab, "Coupling into the slow light mode in slab-type photonic crystal waveguides," Opt. Lett. **31**, 50–52 (2006).

[113] J. P. Hugonin, P. Lalanne, T. P. White, and T. F. Krauss, "Coupling into slow-mode photonic crystal waveguides," Opt. Lett. **32**, 2638–2640 (2007).

[114] A. Hosseini, X. Xu, D. N. Kwong, H. Subbaraman, W. Jiang, and R. T. Chen, "On the role of evanescent modes and group index tapering in slow light photonic crystal waveguide coupling efficiency," Appl. Phys. Lett. **98**, 031107 (2011).

[115] T. P. White, L. C. Botten, C. Martijn de Sterke, K. B. Dossou, and R. C. McPhedran, "Efficient slow-light coupling in a photonic crystal waveguide without transition region," Opt. Lett. **33**, 2644–2646 (2008).

[116] J. Ballato, A. Ballato, A. Figotin, and I. Vitebskiy, "Frozen light in periodic stacks of anisotropic layers," Phys. Rev. E **71**, 036612 (2005).

[117] S. Ha, A. A. Sukhorukov, K. B. Dossou, L. C. Botten, C. M. de Sterke, and Y. S. Kivshar, "Bloch-mode extraction from near-field data in periodic waveguides," Opt. Lett. **34**, 3776–3778 (2009).

[118] A. Gomez-Iglesias, D. O'Brien, L. O'Faolain, A. Miller, and T. F. Krauss, "Direct measurement of the group index of photonic crystal waveguides via fourier transform spectral interferometry," Appl. Phys. Lett. **90**, 261107 (2007).

[119] S. Hughes, L. Ramunno, J. F. Young, and J. E. Sipe, "Extrinsic optical scattering loss in photonic crystal waveguides: Role of fabrication disorder and photon group velocity," Phys. Rev. Lett. **94**, 033903 (2005).

[120] M. Burresi, T. Kampfrath, D. van Oosten, J. C. Prangsma, B. S. Song, S. Noda, and L. Kuipers, "Magnetic light-matter interactions in a photonic crystal nanocavity," Phys. Rev. Lett. **105**, 123901 (2010).

[121] C. M. Soukoulis, ed., *Photonic Crystals and Light Localization in the 21st Century* (Kluwer, Dordrecht, 2001).

[122] D. J. Thouless, "Maximum metallic resistance in thin wires," Phys. Rev. Lett. **39**, 1167 (1977).

[123] P. D. García, R. Sapienza, L. S. Froufe-Pérez, and C. López, "Strong dispersive effects in the light-scattering mean free path in photonic gaps," Phys. Rev. B **79**, 241109 (2009).

[124] Y. Akahane, T. Asano, B.-S. Song, and S. Noda, "High-q photonic nanocavity in a two-dimensional photonic crystal," Nature **425**, 944–947 (2003).

[125] J. Topolancik, B. Ilic, and F. Vollmer, "Experimental observation of strong photon localization in disordered photonic crystal waveguides," Phys. Rev. Lett. **99**, 253901 (2007).

[126] J. Topolancik, F. Vollmer, and B. Ilic, "Random high-q cavities in disordered photonic crystal waveguides," Appl. Phys. Lett. **91**, 201102 (2007).

[127] L. Sapienza, H. Thyrrestrup, S. Stobbe, P. D. Garcia, S. Smolka, and P. Lodahl, "Cavity quantum electrodynamics with anderson-localized modes," Science **327**, 1352–1355 (2010).

[128] L. D. Landau and E. M. Lifshitz, *Electrodynamics of Continuous Media* (Wiley, New York, 1984).

[129] S. Vignolini, F. Intonti, F. Riboli, L. Balet, L. H. Li, M. Francardi, A. Gerardino, A. Fiore, D. S. Wiersma, and M. Gurioli, “Magnetic imaging in photonic crystal microcavities,” Phys. Rev. Lett. **105**, 123902 (2010).

[130] P. Sebbah, B. Hu, J. M. Klosner, and A. Z. Genack, “Extended quasimodes within nominally localized random waveguides,” Phys. Rev. Lett. **96**, 183902 (2006).

[131] R. J. P. Engelen, Y. Sugimoto, H. Gersen, N. Ikeda, K. Asakawa, and L. K. Kuipers, “Ultrafast evolution of photonic eigenstates in k-space,” Nat Phys **3**, 401–405 (2007).

[132] A. F. Koenderink, M. Kafesaki, B. C. Buchler, and V. Sandoghdar, “Controlling the resonance of a photonic crystal microcavity by a near-field probe,” Phys. Rev. Lett. **95**, 153904 (2005).

[133] F. Morichetti, A. Canciamilla, M. Martinelli, A. Samarelli, R. M. De La Rue, M. Sorel, and A. Melloni, “Coherent backscattering in optical microring resonators,” Appl. Phys. Lett. **96**, 081112 (2010).

[134] S. Linden, C. Enkrich, M. Wegener, J. Zhou, T. Koschny, and C. M. Soukoulis, “Magnetic response of metamaterials at 100 terahertz,” Science **306**, 1351–1353 (2004).

[135] M. Burresi, D. van Oosten, T. Kampfrath, H. Schoenmaker, R. Heideman, A. Leinse, and L. Kuipers, “Probing the magnetic field of light at optical frequencies,” Science **326**, 550–553 (2009).

[136] G. Davies and M. F. Hamer, “Optical studies of the 1.945 ev vibronic band in diamond,” Proceedings of the Royal Society of London. A. Mathematical and Physical Sciences **348**, 285–298 (1976).

[137] A. I. Ekimov and A. A. Onushchenko, “Quantum size effect in three-dimensional microscopic semiconductor crystals,” JETP Lett. **34**, 345 (1982).

[138] D. P. DiVincenzo, “Quantum computation,” Science **270**, 255–261 (1995).

[139] J. N. Farahani, D. W. Pohl, H.-J. Eisler, and B. Hecht, “Single quantum dot coupled to a scanning optical antenna: A tunable superemitter,” Phys. Rev. Lett. **95**, 017402 (2005).

[140] O. L. Muskens, V. Giannini, J. A. Sánchez-Gil, and J. Gómez Rivas, “Strong enhancement of the radiative decay rate of emitters by single plasmonic nanoantennas,” Nano Letters **7**, 2871–2875 (2007).

[141] A. G. Curto, G. Volpe, T. H. Taminiau, M. P. Kreuzer, R. Quidant, and N. F. van Hulst, “Unidirectional emission of a quantum dot coupled to a nanoantenna,” Science **329**, 930–933 (2010).

[142] E. M. Purcell, “Spontaneous emission probabilities at radio frequencies,” Phys. Rev. **69**, 681 (1946).

[143] D. E. Chang, A. S. S, E. A. Demler, and M. D. Lukin, “A single-photon transistor using nanoscale surface plasmons,” Nat Phys **3**, 807–812 (2007).

[144] F. Lopez-Tejeira, S. G. Rodrigo, L. Martin-Moreno, F. J. Garcia-Vidal, E. Devaux, T. W. Ebbesen, J. R. Krenn, I. P. Radko, S. I. Bozhevolnyi, M. U. Gonzalez, J. C. Weeber, and A. Dereux, “Efficient unidirectional nanoslit couplers for surface plasmons,” Nat Phys **3**, 324–328 (2007).

[145] D. van Oosten, M. Spasenović, and L. Kuipers, “Nanohole chains for directional and localized surface plasmon excitation,” Nano Letters **10**, 286–290 (2010).

[146] L. W. Couch, *Digital and Analog Communication Systems (6th Edition)* (Prentice Hall, 2001).

[147] D. M. Beggs, M. Midrio, and T. F. Krauss, “Compact polarization rotators for integrated polarization diversity in inp-based waveguides,” Opt. Lett. **32**, 2176–2178 (2007).

[148] T. Barwicz, M. R. Watts, P. A., P. T. Rakich, L. Socci, F. X. Kartner, E. P. Ippen, and H. I. Smith, “Polarization-transparent microphotonic devices in the strong confinement limit,” Nat Photon **1**, 57–60 (2007).

[149] T. P. White, L. O'Faolain, J. Li, L. C. Andreani, and T. F. Krauss, "Silica-embedded silicon photonic crystal waveguides," Opt. Express **16**, 17076–17081 (2008).

[150] L. O'Faolain, S. A. Schulz, D. M. Beggs, T. P. White, M. Spasenović, L. Kuipers, F. Morichetti, A. Melloni, S. Mazoyer, J. P. Hugonin, P. Lalanne, and T. F. Krauss, "Loss engineered slow light waveguides," Opt. Express **18**, 27627–27638 (2010).

List of publications

This thesis is based on the following publications:

- *Measurements of modal symmetry in plasmonic slot waveguides,* M. Spasenović, D. van Oosten, E. Verhagen, and L. Kuipers, Appl. Phys. Lett. **95,** 203109 (2009). **(Chapter 2)**
- *Characterization of bending losses for curved plasmonic nanowire waveguides,* D. J. Dikken, M. Spasenović, E. Verhagen, D. van Oosten, and L. Kuipers, Opt. Express **18,** 16112 (2010). **(Chapter 3)**
- *Nanohole chains for directional and localized surface plasmon excitation,* D. van Oosten, M. Spasenović, and L. Kuipers, Nano Lett. **10,** 286 (2010). **(Chapter 4)**
- *Experimental observation of evanescent modes at the interface to slow-light photonic crystal waveguides,* M. Spasenović, T. P. White, S. Ha, A. A. Sukhorukov, T. Kampfrath, Y. S. Kivshar, C. M. de Sterke, T. F. Krauss, and L. Kuipers, Opt. Lett. **36,** 1170 (2011). **(Chapter 5)**
- *Measuring localisation length of electromagnetic waves via magnetic interaction with a metalised probe,* M. Spasenović, D. M. Beggs, T. F. Krauss, P. Lalanne, and L. Kuipers, in preparation. **(Chapter 6)**

Other publications by the author:

- *Slow-light and evanescent modes at interfaces in photonic-crystal waveguides: optimal extraction from experimental near-field measurements,* S. Ha, M. Spasenović, A. A. Sukhorukov, T. P. White, C. M. de Sterke, L. Kuipers, T. F. Krauss, and Y. S. Kivshar, J. Opt. Soc. Am. B **28**, 955 (2011).

- *Loss engineered slow light waveguides,* L. O Faolain, S. A. Schulz, D. M. Beggs, T. P. White, M. Spasenović, L. Kuipers, F. Morichetti, A. Melloni, S. Mazoyer, J. P. Hugonin, P. Lalanne, and T. F. Krauss, Opt. Express **18,** 27627 (2010).
- *Statistical fluctuations of transmission in slow light photonic-crystal waveguides,* S. Mazoyer, P. Lalanne, J. C. Rodier, J. P. Hugonin, M. Spasenović, L. Kuipers, D. M. Beggs, and T. F. Krauss, Opt. Express **18,** 14654 (2010).
- *Nanowire plasmon excitation by adiabatic mode transformation,* E. Verhagen, M. Spasenović, A. Polman, and L. Kuipers, Phys. Rev. Lett. **102,** 203904 (2009).
- *All-optical coherent control of electrical currents in centrosymmetric semiconductors,* M. Spasenović, M. Betz, L. Costa, and H. M. van Driel, Phys. Rev. B **77,** 085201 (2008).
- *All-optical injection of ballistic electrical currents in unbiased silicon,* M. Betz, L. Costa, M. Spasenović, A. D. Bristow, and H. M. van Driel, phys. stat. sol. (c) **5,** 340 (2008).
- *All-optical injection of ballistic electrical currents in unbiased silicon,* L. Costa, M. Betz, M. Spasenović, A. D. Bristow, and H. M. van Driel, Nat. Phys. **3,** 632 (2007).

Summary

Light is an essential part of the human environment. Since the dawn of mankind, we have been using light to see and communicate. In the last century, there has been an increase in the rate of communication with light, mainly due to the invention of the laser and fiber optics. Lasers are powerful and precise sources of light, which optical fibers can guide over long distances. Lately, there has been a strong drive to use light for computing. Compared to traditional computers, optical computers would have the advantage of speed and easier integration with the communications network. On-chip optical information processing components, such as switches, routers, and memory have all been demonstrated and the first practical devices have already been made. The exploration goes on to make ever smaller and faster integrated components. This thesis explores two concepts which are important for integrated optical sugnal processing: surface plasmon polaritons and slow light in photonic crystal waveguides.

Surface plasmon polaritons (SPPs) are light waves confined to the surface of a metal. These waves can propagate along the surface without leaking out into the metal or the surroundings. We can make metal structures which confine SPPs to small volumes. For example, wires made of gold on a glass substrate, or trenches in a gold film, can both guide SPP waves. Both these types of structures can be made to have widths as small as 40 nanometers (a human hair is about 60000 nanometers in diameter). Such small guides for light are ideal for integrated optics. In this thesis, we investigate both nanowires and nano-trenches.

In Chapter 2, we study SPPs in a nano-trench, also called a slot waveguide. We measure the symmetry of the electric field of the SPP and conclude that the field is anti-symmetric, i.e. opposite electronic charges face each other across the trench. This study is important for understanding the symmetry properties of the trench as an SPP guide, but also for the research field of quantum optics, which puts small sources of light into tightly confined optical fields. The small sources of light are based on electronic charges, which makes their orientation with respect to the symmetry of the optical field a crucial parameter.

In Chapter 3, we study how much gold nanowires can be bent before light leaks out of the wire. We find that the bending losses rise as the bend becomes sharper. In fact, losses due to bending become the primary loss mechanism when the radius of the bend is only 2 micrometers (a human hair is about 60 micrometers in diameter). This study shows that SPP nanowires are a possible candidate for certain optical processing functions.

In Chapter 4, we look at how SPPs are made from light which strikes a chain of holes in a gold film. Each hole launches SPPs along the film. These SPPs mix and create a "plasmonic carpet", a complex structure of maxima and minima in the optical field. At a certain distance from the chain, the mixing of the SPPs is such that an exact image of the chain is formed. This self-imaging effect was observed in 1836 in ordinary dielectric gratings by Henry Fox Talbot, after whom it is named the Talbot effect. Talbot predicted exactly at which distance from the grating the self-imaging will occur. Our results show that this prediction needs to be corrected in the case of gratings and chains in which the spacing between single components of the chain is close to the wavelength of the light. The maxima in the carpet are spatially localized, hence we predict that this research will be useful for delivering optical energy to precise positions on a chip.

Photonic crystal waveguides are guides for light in which certain frequencies (colors) of light are slowed down. From a technological point of view, slow light can be applied to optical memory, switches and routers. From a more fundamental physical point of view, light interacts with the crystal in a different manner when it is slowed down than when it moves fast. In the thesis, we investigate both the technological aspect and the more fundamental physical process which occurs in the slow light regime.

In Chapter 5, we deal with the challenge of making slow light. In general, since the behavior of slow light is different than that of fast light, it is thought that going from fast to slow light requires a carefully optimized transition region. We show experimentally, based on previous theoretical predictions, that efficient transfer from fast to slow light can be achieved without a transition region. We show that at an interface between fast-light and slow-light sections of a photonic crystal waveguide a special kind of optical mode is created, which decays away from the interface. This special, “evanescent” mode assists in matching the profiles of fast and slow light, hence increasing the efficiency of coupling to slow light. The results of the chapter open up possibilities to engineer many devices based on slow-light.

In Chapter 6 we study light-matter interactions in the slow-light regime. When light is slowed down, it interacts more strongly with the waveguide. When the interaction is strong enough, light will scatter many times from any engineered or undesired defect. When light scatters many times, it is said to exist in the “multiple scattering” regime, in which it behaves very different than it does in normal propagation. Multiple scattering disrupts transmission, so that the waveguide becomes unusable for many applications. Even with state-of-the-art fabrication, multiple scattering inevitably sets in if the velocity of light is reduced sufficiently. In Chapter 6, we show a new method for measuring at which frequency multiple scattering occurs in a particular waveguide, effectively opening a new direction for exploration of multiple scattering in photonic crystal waveguides. Deeper understanding of this phenomenon may help in finding ways to prevent it from happening or shift the frequencies at which it happens away from those which one would like to use for applications.

Acknowledgements

"I choose my generals based on how lucky they are."

- Napoleon Bonaparte

Kobus, once upon a time, when I was starting my PhD and doing my first measurements, you mentioned the above quote. It referred to my statement that "I am usually lucky with measurements". You thus compared yourself to Napoleon, and myself to a general. Ever since, I have felt just the same: a general, in the army of Kobus. We fought, we conquered, we lost, retreated, stood up and fought again. Kobus, you lead without commanding; you teach without lecturing; you guide without pointing; and I thank you for it all.

If this research group is a body, with Kobus the head, then, for the largest part of my PhD, Dries was the right arm, and Hinco the left. The rest of us were legs. Sometimes striding or even leaping, sometimes weak and trembling, most often pushing through mud and dirt, leaving a trail in the vast desert that is nanophotonics, pushing with a relentless stubborness which is all the more shocking if one realizes that we actually didn't know where we're headed and what waits for us.

Dries, I have never before or since seen a scientist who works with so much passion, so much ferocity, or such appalling skills as you. Working next to you was as terrifying as it was amazing. You left behind a frightening void, but you also left me with the skills needed to fill this gap, and I thank you for that. And remember, "you're a group leader now, and you have to suffer it". At least we will always have Baltimore.

Hinco, you were as instrumental to my success as you have been for students past, and I'm sure you will keep being for students to come.

Matteo, watching you struggle with three years of incomprehensible data, uncertainty and failure, followed by almost a year of painful labour, and the birth of your thesis and all that's in it, has been truly remarkable. The "rennaisance", or "golden age" of this group of which you were the core brought with it moments and feelings which I've never come across. I hope to work with you in the future. It's been a pleasure sleeping with you in Cairo.

Many others contributed to this fantastic period: Tobias, Jord and Aron were constant ingredients. Aron, you were a true soldier, ready to jump in whenever things needed to be done as a collective. It's been very pleasant travelling to conferences with you, and I won't forget that you always trusted and accompanied me, at AMOLF and outside. Thank you for the brilliant presentation at my defense celebration. You are really the only one who could piece that together. Thank you also for the poker lesson which I received from you in Munich.

Nir, you brought a breath of fresh air to our group. I hope that your relaxedness and willingness to accept scientific criticism will be contagious. I'm glad to have had a second chance to publish with you. Next time though, I promise we will be on the same level of the scientific hierarchy.

I'd like to thank Marijn Sandtke and Rob Engelen for their help at the beginning of my PhD. I've also enjoyed working with Lydwin, Benny, Milan, Daryl, Hakkı, Sanli, Alberto, MarCo Seynen, Sjoerd, Duncan, Idsart, Hans Z, and Chris. Ewold Verhagen has taught me important lessons on determination and goal setting. Apart from that, thank you for expressing interest in absolutely every project of mine. Writing papers with you has been a true lesson on clarity. I would also like to thank Albert Polman for his contributions to the work which we did together. Additionally, the meetings and knowledge-sharing with the group of Resonant Nanophotonics has been a very pleasant experience. Thanks to Wouter Harmsen, Enid Bouman, Anouk Nelissen, and Wenda Hetem.

Dirk Jan and Thijs, I hope I have been as good a master as you have been slaves. The work which you contributed to my thesis will stay forever with me. I wish you success in whatever you indulge in.

Finally, I'd like to thank everyone from Nanophotonics at AMOLF, for all the interactions. Thanks to Prof. Bela Mulder for advice on the design of the cover of this thesis. I thank my committee for careful reading of the thesis manuscript. In particular, I thank Jennifer Herek and Kobus Kuipers for being so kind and helping with the reception. Thank you Jennifer for being instrumental in bringing me here in the first place.

I thank The Great Kossus for inspiration and guidance.

Outside of AMOLF, I'm proud to have collaborated with the SPLASH group - the experience has dramatically changed the course of my PhD, for the better. I thank Philippe Lalanne, Thomas Krauss, Andrea Melloni, Marc Sorel, Richard de la Rue, and everyone else from SPLASH, for the experience of sharing science with so many experts as much as for the social events in Milan and Amsterdam. I would also like to thank Martijn de Sterke, Tom White, and the CUDOS collaboration for the knowledge gained while writing papers together.

The student chapter of the OSA was a venture into work beyond the boundaries of science. Its success has confirmed again that extraordinary things can be done by ordinary people, especially when ordinary people team up. I am deeply indebted to Andrej Kwadrin, Matthias Wulf, and Aron Opheij, and I am certain that with them I am leaving the chapter in good hands. I look forward to joint events with the Barcelona chapter. Also thanks to Boris and Felipe, for continuing with the chapter, as well as for everything else.

Personally, during this period I have fully come to grips with myself. The number of people who contributed to this experience is infinite, but out of infinity stand out a few. Bergin, we move on, always after a few years, but we leave behind trenches so deep as to never be forgotten. You have an amazing mind, let it out. Gijs, stay sane. Thank you for taking care of me when I was sick. You are very kind. Jean... you just came in and out... and in again. Rony boy, thanks for all the nights out, for Rajoy and Alberto, for Istanbul. Jochen, thank you as well.

Ivana, ti si divna. Daljina je samo privid, ali ipak znam da nigde na drugom mestu neću imati takvu drugaricu.

Udaljenost... Ta reč zaokružuje ono što mi se dešava već petnaestak godina. Udaljenost od slobode, zatim udaljenost od Žarkova i Beograda, pa udaljenost od porodice, udaljenost od društva, čak udaljenost od sebe. Djuro, Božo, Nebojša, Nešo, Kobayo, svi ste vi zaslužni za jedan deo onoga što jesam. Marija, guten freude, Gertrude.

Zahvalan sam ujaku Goranu za svu pomoć i ohrabrivanje na putu do Amsterdama. Zahvaljujem se i ujkinom tati Joci, za jedinstven primer i inspiraciju.

Zahvaljujem se sestri Jeleni koja me je naučila da čitam i pišem i koja je uvek ohrabrivala moju kreativnu stranu. Neke periode svog života bez nje jednostavno ne bih preživeo. Hvala zetu Marku za sve, a posebno za ručkove.

Svako krči svoj put i za njega je odgovoran, ali ne polazimo svi sa istim orudjem. Dragi roditelji, svestan sam i ljubavi i mnogostruke žrtve i bezgranične dobrote i ljubavi prema drugima koju ste u mene usadili. Vi ste svakako, zajedno sa mnom, najzaslužniji za ovaj uspeh. Zahvaljujem se i ostatku “ukućana”: Slavici, Muti, Vladi, Branki, Obrenu, Milanu i malom Predragu, mojim hodajućim radostima.

Snežana, ono što prema tebi osećam može se iskazati samo nevidljivim mastilom: